Dynamics, Pathways, and Regulation of Exocytotic Release

Rui Su

Submitted in partial fulfillment of the
requirements for the degree of
Doctor of Philosophy
under the Executive Committee
of the Graduate School of Arts and Sciences

COLUMBIA UNIVERSITY

2023

© 2023

Rui Su

All Rights Reserved

Abstract

Dynamics, Pathways, and Regulation of Exocytotic Release

Rui Su

Exocytosis involves fusion between a membrane-bound vesicle containing signaling molecules and the plasma membrane of the cell. Cells use exocytosis to release membrane-impermeant bioactive molecules to the extracellular space, and to deliver lipids and proteins to the plasma membrane. Exocytosis is essential to many fundamental processes including neurotransmission and hormone secretion. Exocytosis is triggered and regulated by a range of cellular components including calcium, SNARE proteins, and the actin cortex. Despite of the accumulative discovery of molecules involved in exocytosis, a unified physical landscape that these molecules act on is missing. The biophysical forces driving exocytosis haven't been identified, and the mechanisms by which these biophysical forces regulate exocytosis are not established.

To address these unsolved questions, we built mathematical model to study exocytosis on the single-vesicle level and the cell level. In the first chapter of the thesis we modeled the shape evolution of dense-core vesicles in chromaffin cells during exocytosis. Emerged from the model, we discovered a novel mechanism that drives vesicles to merge into the plasma membrane. Following fusion, the osmotic pressure of the cell squeezes the vesicle and abolishes the vesicle membrane tension, and the high plasma membrane tension reels the vesicle onto the adjacent cytoskeleton. With no fitting parameters, the model predicted remarkable vesicle shapes consistent with real-time visualizations by super-resolution microscopy from the Wu lab. Interestingly, we predicted vesicles to adopt elongated tubular shapes under mildly high osmotic

pressure, which was confirmed by visualizations from the Wu lab, providing a vivid illustration of osmotic squeezing.

In the second chapter of the thesis we investigated fusion pores, the membrane connection between a fused vesicle and the plasma membrane. As commonly observed in amperometric traces, the initially small pore may subsequently dilate for full contents release. Here using formalisms of differential geometry, we obtained exact solutions for fusion pores between two membranes. We found three families: a narrow pore, a wide pore and an intermediate tether-like pore. We suggest membrane fusion initially generates a stable narrow pore, and the dilation pathway is a transition to the stable wide pore family. The unstable intermediate pore is the transition state that sets the energy barrier for this dilation pathway. Pore dilation is mechanosensitive, as the energy barrier is lowered by increased membrane tension. Finally, we showed fusion pores are locked into the narrow pore family in nanodisc-based experiments, powerful systems for the study of individual pores.

In the third chapter of the thesis we investigated the mechanism of spatiotemporal regulation of exocytosis on the cell level. By analyzing the spatiotemporal profile of exocytosis events in chromaffin cells observed by confocal microcopy from the Wu lab, we discovered a novel mechanism of exocytosis regulation via release site availability. We found vesicle fusion can happen repeatedly at hotspots, which generated a membrane reservoir consisting of unmerged and slowly merged vesicles that are spatially close to hotspots. In turn, unmerged vesicles occupy release sites and locally suppress exocytosis frequency. We developed a mathematical model to demonstrate that such membrane reservoir requires sufficiently low local membrane tension that abolishes the driving force of vesicle merger.

Finally, in the fourth chapter of the thesis we studied virus entry, a process similar to exocytosis but involves membrane fusion between the virus and the host cell. SARS-CoV-2 entry in to host cells is accomplished by the S2 subunit of the spike S protein by capture of the host cell membrane and fusion with the viral envelope. Membrane capture requires the native S2 to transit to its potent, fusogenic form, the fusion intermediate, whose structure is unknown. Here, we computationally constructed a full-length model of the CoV-2 fusion intermediate by extrapolating from known CoV-2 pre- and postfusion structures. In atomistic and coarse-grained molecular dynamics simulations the fusion intermediate was remarkably flexible and executed large bending and extensional fluctuations due to three hinges in the C-terminal base. The large configurational fluctuations of the fusion intermediate generated a substantial exploration volume that aided capture of the target membrane. Simulations suggested a host cell membrane capture time of ~ 2 ms. Our simulated structures of the fusion intermediate showed good agreement with cryo-electron tomography data from the Moscona’s lab.

Table of Contents

List of Charts, Graphs, Illustrations iii

Acknowledgments v

Introduction 1

Chapter 1: Vesicle shrinking and enlargement play opposing roles in the release of exocytotic contents 4

- 1.1 Introduction 4
- 1.2 Results 6
- 1.3 Discussion 24
- 1.4 Appendix: Justification and details of the mathematical model 28

Chapter 2: Three membrane fusion pore families determine the pathway to pore dilation 37

- 2.1 Introduction 37
- 2.2 Results 40
- 2.3 Discussion 56
- 2.4 Appendix: Derivation of the model and numerical methods to solve the model 59

Chapter 3: Spatiotemporal regulation of exocytosis by a membrane reservoir via release site availability 75

- 3.1 Introduction 75
- 3.2 Results 78

Chapter 4: Host cell membrane capture by the SARS-CoV-2 spike protein fusion intermediate 93

- 4.1 Introduction 93

4.2 Results 96

4.3 Discussion 116

4.4 Appendix: Details of the simulations and the analysis 120

Conclusion 139

References 143

List of Charts, Graphs, Illustrations

Figure 1.1. Direct visualization of Ω-shape membrane profile shrinking and enlargement. 9

Figure 1.2. Observation of Ω-shape membrane profile shrinking and enlargement while releasing FFN511. 11

Figure 1.3. Fusion pore dynamics during shrink-, partial-shrink-, same-size- and enlarge-fusion. 14

Figure 1.4. Imaging NPY-EGFP release and structural changes of A647-labelled fusing vesicles. 18

Figure 1.5.Mathematical model of vesicle evolution during exocytosis. Model parameters as in Table 1.1. 23

Figure 2.1. Three families of fusion pores between two planar membranes. 43

Figure 2.2. Two microscopic catenoidal fusion pores are observable between freely hinged membranes. 49

Figure 2.3. A narrow and a wide fusion pore family are stable for realistic membrane bending constraints. 52

Figure 2.4. Nanodiscs lock fusion pores into thin quasi-catenoids 54

Figure 2.5. Model of the pore dilation transition during exocytosis. 56

Figure 3.1. Confocal imaging of cultured chromaffin cells following whole-cell calcium dialysis. 80

Figure 3.2. Four fundamental classes of vesicle evolution during exocytosis. 83

Figure 3.3. Vesicles release at hotspots. 85

Figure 3.4. Repeated exocytosis generates a membrane reservoir spatially close to hotspots 89

Figure 3.5. Schematic of the mathematical model of the reservoir. 92

Figure 4.1. Model of the SARS-CoV-2 spike protein fusion intermediate. 98

Figure 4.2. All-atom simulation of the SARS-CoV-2 fusion intermediate 100

Figure 4.3. The fusion intermediate is highly flexible and visits a large capture volume. 102

Figure 4.4. Multiscale simulations of the membrane-bound fusion peptide. 106

Figure 4.5. Membrane binding kinetics of an isolated fusion peptide. 107

Figure 4.6. Interaction of the fusion intermediate with a target membrane. 111

Figure 4.7. Comparison of the fusion intermediate simulations with cryo-ET density maps. ... 113

Figure 4.8. Model of the SARS-CoV-2 fusion intermediate and the pathway to fusion. 116

Acknowledgments

I would like to express my deepest appreciation my advisor, Ben O’Shaughnessy, for constantly motivating me to explore the truth of the world, for continuously providing insightful guidance on my projects, and for patiently teaching me how to think as an independent scientific researcher.

I’m very grateful for having the opportunities to develop research projects together with Zachary McDargh, Sathish Thiyagarajan, Shuyuan Wang, Dong An and Jin Zeng. I benefit a lot from your valuable inputs. I would also express my gratitude to Roberto Alonso-Matilla, Nadiv Dharan, Anirban Polley, Hongkang Zhu, Tianyi Zhu, and Ioana-Cristina Butu, for helpful and interesting discussions.

I’m also very thankful to our collaborators Ling-gang Wu, Wonchul Shin, Gianvito Arpino, Lihao Ge, Anne Moscona, Matteo Porotto, and Tara Marcink. My work was highly motivated from their breakthrough experiments. Thanks should also go to the National Institute of General Medical Sciences of the National Institute of Health, for funding my research.

Finally I would extend my sincere thanks to my parents Caichi Liu and Tao Su. I would not finish my PhD without your unconditional support.

To my parents.

Introduction

i. Overview of exocytosis

Cells use exocytosis to secrete bioactive molecules to the extracellular environment, or to deliver proteins and lipids to the plasma membrane (PM). During exocytosis, membrane-bound vesicles fuse with the PM and then content molecules inside the vesicle diffuse to the extracellular space. Exocytosis is central to many vital processes, including neurotransmitter release at the synapse for neurotransmission and insulin secretion by pancreatic β-cells for blood glucose level regulation. The vesicle size varies greatly in different cells, from synaptic vesicles of ~50 nm diameter in neurons (1) to dense-core vesicles of ~400 nm diameter in chromaffin cells (2).

Three stages are involved in exocytosis. First, vesicles are transported to the release sites on the PM mediated by various motor molecules including kinesin, dynein and myosin associated with the cytoskeleton (3, 4). Then the vesicle gets docked and primed by forming partially assembled SNARE complexes, ready to release its contents upon stimulus (5, 6). Second, specialized fusion machineries respond to a signal (usually Ca^{2+}), fuse the vesicle membrane with PM, and create a fusion pore through which vesicle contents are released. SNARE proteins are the core of the fusion machinery, which zipper into SNAREpins complexes to catalyze fusion by pulling membranes together (7-9). Finally, the molecules stored in the vesicles secret into the extracellular space through the fusion pore, whose size and dynamics are critical to regulate release rates (10, 11). The fused vesicle can merge into the PM, remain static or grow dramatically (12, 13). This thesis focuses on the post-fusion stage of exocytosis.

ii. Post-fusion vesicle evolution

From a vast body of research using microscopies and electrophysiological measurements, a consensus view has emerged that, immediately following membrane fusion the Ω-shaped vesicle-PM composite evolves along one of two pathways (14-16). (1) Full-fusion. The pore dilates and the Ω-profile flattens into the PM, with full contents release. (2) Kiss-and-run. The pore transiently opens and then closes, giving partial contents release. A new picture was suggested by recent super-resolution microscopy studies visualizing exocytosis in chromaffin cells (12, 13, 17). Vesicles can merge into the PM, remain static, or grow. Particularly vesicle flattening in full-fusion was not observed. Instead, the vesicles shrink into the PM in a self-similar fashion, remaining their Ω-profiles. However, the driving forces and the mechanisms of post-fusion vesicle evolution have not been understood.

iii. Fusion pores are dynamical structures controlling content release rates

Once fusion between the vesicle and the plasma membrane is completed, content molecules will release through the fusion pore, the connection between the fused membranes (18). Conductance measurements at the Calyx of Held revealed minimum synaptic vesicle pore diameters of ~ 1 nm that can flicker repeatedly (19). A historic development was the use of microelectrodes to detect the far slower release from non-synaptic secretory cells which showed that the initial fusion pore is very small but often dilates dramatically after a delay (20). The narrow initial pore may serve as a molecular sieve to modulate size and rate of vesicle cargo release (10, 21), while full release requires the pore to dilate. For example, fusion events at synaptic terminals may result in partial or total neurotransmitter release, depending on whether the nascent pore dilates fully or reseals, with important consequences for synaptic activity (11, 14). Impaired pore expansion is associated with disease such as type 2 diabetes where insulin release is misregulated (22). Although a range of molecules including SNAREs, synaptotagmin and dynamin were found to regulate fusion pore size (13, 23, 24), the energetic landscape of pore dilation on which these molecules act on is not clear.

iv. Spatiotemporal regulation of exocytosis

Exocytosis is spatially regulated by cells. In neurons synaptic vesicles are released at the active zone that is precisely aligned with the receptors on the postsynaptic density (25). In endocrine cells, the existence of such active zone is not obvious (26). Instead, vesicle fusion can happen repeatedly at hotspots (27-29). Lacking such hotspots might be the cause of impaired insulin secretion in type 2 diabetes (28). Exocytosis is also temporally regulated, reflected as highly modulated exocytosis rates upon different stimulus protocols in different cells (30). In neurons the availability of readily releasable vesicles is thought to be cause of short-term depression (31-34). In secretory cells such as chromaffin cells, the actin cortex can be a barrier of exocytosis by separating vesicles from the PM (35), but meanwhile can serve as a carrier by navigating the vesicle to the docking sites (36). Temporal regulation of exocytosis may also be executed via the availability of release sites. A fixed number of release sites was suggested by early statistics of the postsynaptic currents (37). After a release event, the site experiences a refractory period during which the next vesicle is not able to dock (38). It is proposed that to make the site reusable again the vesicle components of the previous exocytosis event has to be cleared away either by passive diffusion or by active removal of the local membrane (39). However, the mechanism of regulating site availability and how hotspots participate in temporospectral regulation of exocytosis is unknown.

Chapter 1: Vesicle shrinking and enlargement play opposing roles in the release of exocytotic contents

In this chapter, I describe collaborative work combining experimental visualizations of vesicle release during exocytosis in chromaffin cells and mathematical modeling of vesicle evolution under biophysical forces. The modeling part is my original work with equal contribution from Dr. Sathish Thiyagarajan, a former postdoctoral researcher in the O'Shaughnessy group. The experiments are performed by the Ling-Gang Wu group at National Institute of Health.

1.1 Introduction

Hormone and transmitter release by endocrine cells and neurons mediate many important functions, such as stress responses, immune response, control of blood glucose with relevance to diabetes, and synaptic transmission which is essential for cognition and coordinated motor activity (5, 14, 16, 40-42). Regulation of the amount and the rate of release is physiologically crucial, and much research has addressed the mechanisms involved (5, 14, 16, 40-42). From decades of research, a widely held view emerged that content release by neurons and endocrine cells is controlled by two modes of fusion: 1) full-collapse, in which the fusion pore dilates while the vesicle flattens into the membrane, resulting in rapid and complete release, and 2) kiss-and-run, when a narrow fusion pore opens and then closes, giving a slow and/or partial release of contents (5, 14, 16, 40-42).

Recently, this view has been questioned in two respects. First, kiss-and-run often involves a large pore (13, 43), inconsistent with the assumed narrow pore. Second, while full-collapse was proposed on the basis of electron microscopy data (44), it has not been observed in live cells. Imaging in endocrine cells shows shrinking fusion spots, rather than growing fusion spots that subsequently disappear, as would be expected from full-collapse (12, 17). It was proposed that the shrinking spots indicated a fusion mode termed shrink-fusion, in which the vesicle shrinks while retaining its shape without pore dilation, and shrink-fusion was suggested to be mediated by F-actin-dependent plasma membrane tension (17).

While these observations imply the possibility of replacing full-collapse with shrink-fusion, direct evidence of shrink-fusion is lacking. To demonstrate shrink-fusion would require visualization of vesicle membrane profiles to measure the evolution of vesicle shape and to demonstrate that the pore does not dilate. Such visualization is also required to eliminate other possibilities, including rapid budding of clathrin-coated vesicles at the fusion-generated Ω-profile as recently suggested (45, 46). Direct visualization is indeed feasible, as shown in recent studies that visualized Ω-shaped membrane profiles and their pores (13, 47). However, these studies did not investigate Ω-profile shrinking or pore dynamics during shrinking (13, 47).

The proposal of shrink-fusion in replacement of full-collapse raises the question as to why shrinking is preferred to the intuitively appealing full-collapse pathway, whether shrink-fusion promotes release and by what mechanism. The observation that kiss-and-run does not limit content release (13, 43) raises the question whether there is a fusion mode specifically for the limiting of content release. Here we addressed these fundamental questions by super-resolution STED imaging of vesicular membrane profiles and fusion pore dynamics, confocal imaging of content release, electron microscopy and realistic mathematical modelling in neuroendocrine chromaffin cells. We found that facilitation of content release is not mediated by full-collapse, but by shrink-fusion with a large fusion pore, and that inhibition of release is not mediated by kiss-and-run, but by enlarge-fusion mode, in which Ω-profiles increase in size, but maintain a narrow pore. We discovered that cells' physiological osmotic pressure squeezes, but not dilates the Ω-profile, explaining why shrink-fusion, rather than full-collapse, is the default fusion more for merging vesicles with the plasma membrane and for promoting content release. We concluded that shrink- and enlarge-fusion control the yin and yang of exocytotic content release.

1.2 Results

Direct observation of fused vesicle shrinking and enlargement in live cells

To determine how vesicles merge with the plasma membrane (PM) during exocytosis, we transfected bovine adrenal chromaffin cells in primary cultures with EGFP or mNeonGreen attached to phospholipase C delta PH domain (PH_G: either PH-EGFP or PH-mNeonGreen). PH_G binds to PtdIns(4,5)P2 (PIP_2) at PM cytosolic-facing leaflet and thus labels PM (Fig. 1.1A) (13, 47). We added Atto 532 (A532) in the bath (Fig. 1.1A), which enters the fusing Ω-profile to confirm the structural changes revealed by PH_G imaging (12, 13). We induced vesicle fusion using 1-s depolarization from -80 to +10 mV through a pipette in the whole-cell configuration, which induced calcium currents and capacitance changes reflecting robust exo- and endocytosis (Fig. 1.1A). STED imaging of A532 and PH_G was performed in the microscope XZ plane at a fixed Y-location near the cell bottom every 26-300 ms per frame (XZ/Y_{fix} imaging) before and after $depol_{1s}$ for ~20-30 s. Each cell was subjected to only one $depol_{1s}$, which induced fusion mostly during and ~3 s after $depol_{1s}$ (12, 13).

$Depol_{1s}$ induced PH_G-labelled Ω-shape profiles (PH-Ω) filled with A532 (Figs. 1.1B-H), reflecting diffusion of PH_G and A532 from PM and bath into the fusion-generated Ω-profile. PH-Ω without A532, which reflected hemi-fusiowrn (47), was not analysed here. In ~20% of cells, we observed a $depol_{1s}$-induced, fusion-generated A532-filled PH-Ω with a clear membrane outline. Following PH-Ω appearance (236 events, 202 cells), the Ω-profile either 1) shrank while maintaining an Ω-shape until it became undetectable (shrink-fusion, 45 events, Figs. 1.1B-D), 2) shrank partially, then maintaining a reduced-size Ω-profile (partial-shrink-fusion, 24 events, Figs. 1.1E-F), 3) maintained its Ω-profile and A532 spot size (same-size-fusion, 136 events, Fig. 1.1G), or 4) increased in size while maintaining its Ω-shape (enlarge-fusion, 31 events, Fig. 1.1H; summarized in Fig. 1.1I). The PH-Ω width at the fusion onset was similar for these four fusion modes.

Shrink-fusion was rapid, with a 20-80% shrinking time mostly <2 s (Figs. 1.1B-D). During shrinking episodes (both shrink-fusion and partial-shrink-fusion), in most cases the Ω shape of the vesicle was preserved as the width and height decreased proportionally (Figs 1.1B, 1.1C and 1.1E). However, in some instances of shrink-fusion the vesicle had an extended tubular shape with a height considerably greater than the width (Figs. 1.1D, 1.1F). We did not observe vesicle budding off the PH-Ω during shrink-fusion (n = 45), excluding this as the mechanism that shrinks the PH-Ω.

Enlarge-fusion was slower than shrink-fusion, with a 20-80% time of ~2-20 s (Fig. 1.1H). Enlarge-fusion was detected when the width of the PH-Ω measured at 20-30 s after fusion onset (516 ± 18 nm) increased by >15% as compared to that at the fusion onset (~26 ms – 300 ms, 352 ± 13 nm, n = 31; t test, $p < 0.001$). The width of PH-Ω measured at 20-30 s after the onset of enlarge-fusion (516 ± 18 nm, n = 31) was significantly larger than that of same-size-fusion (374 ± 7 nm, n = 136; t test, $p < 0.001$).

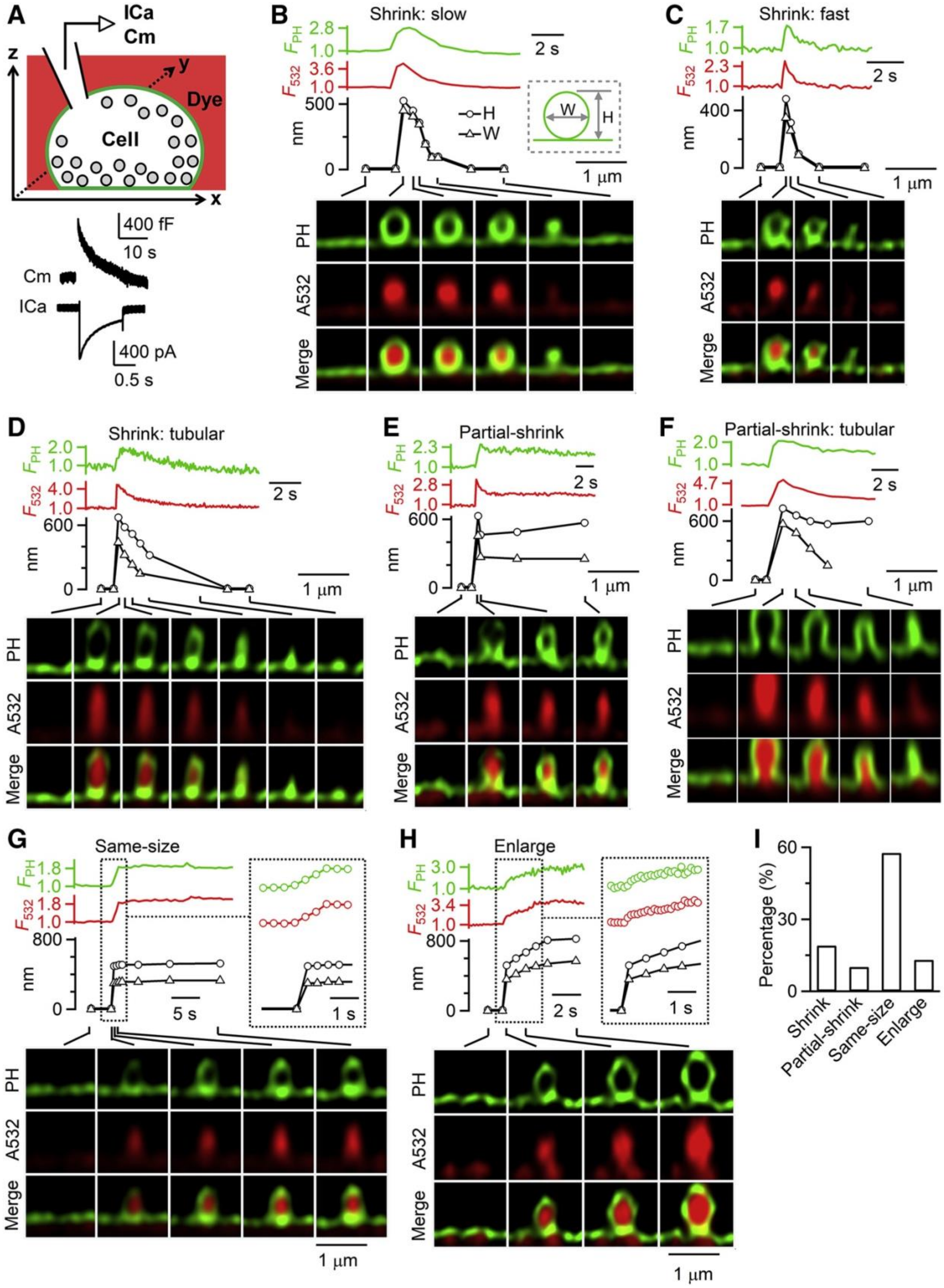
A
ICa
Cm
z
y
x
Dye
Cell
400 fF
10 s
Cm
ICa
400 pA
0.5 s
B
Shrink: slow
F_{PH}
2.8
1.0
2 s
F_{532}
3.6
1.0
500
nm
0
H
W
1 μm
PH
A532
Merge
C
Shrink: fast
F_{PH}
1.7
1.0
2 s
F_{532}
2.3
1.0
400
nm
0
1 μm
PH
A532
Merge
D
Shrink: tubular
F_{PH}
2.0
1.0
2 s
F_{532}
4.0
1.0
600
nm
0
1 μm
PH
A532
Merge
E
Partial-shrink
F_{PH}
2.3
1.0
2 s
F_{532}
2.8
1.0
600
nm
0
1 μm
PH
A532
Merge
F
Partial-shrink: tubular
F_{PH}
2.0
1.0
2 s
F_{532}
4.7
1.0
600
nm
0
1 μm
PH
A532
Merge
G
Same-size
F_{PH}
1.8
1.0
F_{532}
1.8
1.0
800
nm
0
5 s
1 s
PH
A532
Merge
1 μm
H
Enlarge
F_{PH}
3.0
1.0
F_{532}
3.4
1.0
800
nm
0
2 s
1 s
PH
A532
Merge
1 μm
I
Percentage (%)
60
30
0
Shrink
Partial-shrink
Same-size
Enlarge

Figure 1.1. Direct visualization of Ω-shape membrane profile shrinking and enlargement. (A) Upper: setup drawing. Cell's membrane and bath are labelled with PH_G (green) and A532 (red, pseudo-colour), respectively. ICa and Cm (capacitance) are recorded via a whole-cell pipette. Lower: Sampled ICa and the Cm change induced by $depol_{1s}$ at the whole-cell voltage-clamp configuration. (B-H) PH-Ω fluorescence (F_{PH}, normalized to baseline), A532 spot fluorescence (F_{532}, normalized to baseline), PH-Ω height (H, circles), PH-Ω width (W, triangles), and sampled images at times indicated with lines showing fusion with various patterns of Ω-profile structural changes: B-D, shrink-fusion (B, slow; C, fast; D, generation of tubular intermediates); E-F, partial-shrink-fusion (E, generation of reduced-size Ω-profile; F, generation of reduced-size tubular structure); G, same-size-fusion; H, enlarge-fusion. The inset in G-H is shown at the same time scale (right) for side-by-side comparison. When PH-Ω was too dim or smaller than our resolution, PH-Ω height and width were not measured. Images were acquired at the STED XZ/Y_{fix} configuration. (I) The percentage of shrink-fusion, partial-shrink-fusion ($shrink_{partial}$), same-size-fusion and enlarge-fusion (total PH-Ω number: 236; from 202 cells).

The width and height of the PH-Ω increased approximately proportionally to one another during enlarge-fusion (Fig. 1.1H). Additional vesicle fusion at the PH-Ω was not observed during enlarge-fusion (n = 31), excluding compound fusion as the origin of enlarge-fusion.

Three sets of evidence showed that shrinking or enlargement was not due to Ω-profile movement in the XY-plane. First, random Ω-profile movement would in general involve displacements in both the X- and Y- directions – whereas during shrinking or enlargement captured by STED XZ/Y_{fix} imaging the Ω-profile did not shift in the X direction (n = 69, Fig. 1.1B-H). Second, STED XY-plane imaging at a fixed Z-focal plane (XY/Z_{fix} imaging) showed that $depol_{1s}$ induced the appearance of PH-labelled rings containing A532 spots, which reflected fusion-generated Ω-profiles induced by $depol_{1s}$ (12, 13). These PH-labelled rings shrank, remain unchanged or enlarged, but did not move in the XY-plane (102 events, 7 cells). Third, in cells treated with high potassium (70 mM) solution for 45 s and fixed with 4% paraformaldehyde, we observed PH-Ω most likely induced by high potassium stimulation. All these PH-Ω (59 PH-Ω in

39 cells) did not change in width over 20-30 s STED XZ/Y_{fix} imaging, indicating that PH-Ω size changes observed in live cells are not due to microscopic Y-axis drift.

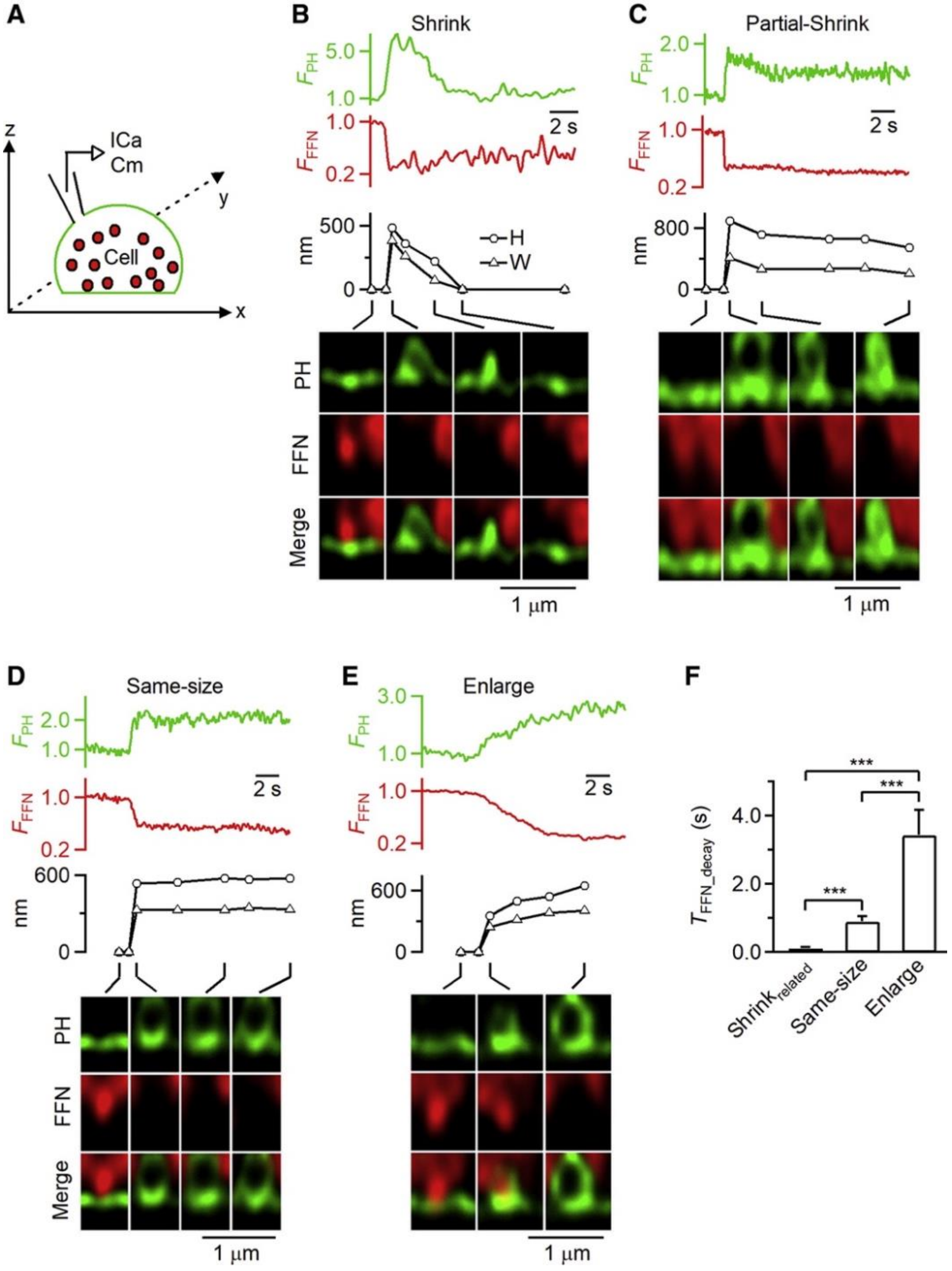

Figure 1.2. Observation of Ω-shape membrane profile shrinking and enlargement while releasing FFN511.
(A) Schematic diagram of the experimental setup: vesicles are loaded with FFN511 (red, pseudo-color), plasma membrane is labelled with PH_G (green), and ICa and capacitance (Cm) are recorded via a pipette at the whole-cell configuration. (B-E) PH-Ω fluorescence (F_{PH}, normalized to baseline), FFN511 fluorescence (F_{511}, normalized to baseline), PH-Ω width (W, triangles), and sampled images at times indicated with lines showing release of FFN511 for shrink-fusion (B), partial-shrink-fusion (C), same-size-fusion (D) and enlarge-fusion (E). (F) 20-80% decay time of FFN511 (T_{FFN_decay}) for shrink-fusion (8 events), partial-shrink-fusion (13), same-size-fusion (53 events) and enlarge-fusion (18 events). Data taken from 71 cells where STED XZ/Y_{fix} imaging of PH_G/FFN511 was performed. **: $p<0.01$; ***: $p<0.001$; ANOVA test.

To verify that the observed PH-Ω structural changes reflect post-fusion structural changes, we loaded vesicles with fluorescent false neurotransmitter FFN511 via bath application (Fig. 1.2A) (48). $Depol_{1s}$ induced PH-Ω that released FFN511, as observed with STED XZ/Y_{fix} imaging of PH_G and FFN511 (Figs. 1.2A-E, n = 92 events, 71 cells) (13). Similar to STED PH_G/A532 imaging, we observed shrink-fusion (n = 8), partial-shrink-fusion (n = 13), same-size-fusion (n = 53), and enlarge-fusion (n = 18, Figs. 1.2B-E). The 20-80% FFN511 release time depended on the fusion mode (Fig. 1.2F), which would be further discussed later. These results confirmed that the observed PH-Ω size changes reflect post-fusion vesicle size changes.

Consistent with Ω-profile shrinking and enlargement (Fig. 1.1), electron microscopy revealed Ω-profiles of various sizes, some of which approached a tubular shape (Figs. 1.3A-B); widths ranged from 56-784 nm, and larger width was correlated with larger height (Fig. 1.3C-upper). The height/width ratio was mostly > 1 (85% of cases, Fig. 1.3C-lower), indicating that Ω-profiles were mostly somewhat elongated with some approaching a tubular-shape, consistent with STED observation of mostly elongated Ω-profiles (e.g., Figs. 1.1B-H, 1.3D-H). The pore size range measured with electron microscopy was similar to the STED-measured $Pore_v$ range (13).

As the PH-Ω shrank, remained unchanged in size or enlarged, in some cases the pore closed. This was reflected as decay of the spot A532 fluorescence (F_{532}, strong excitation) to the baseline while PH-Ω size remained unchanged, due to closure of the pore that prevented exchange of the bleached A532 (caused by strong excitation) with fluorescent A532 in the bath (12, 47). Since the present work focuses on PH-Ω size changes, unless otherwise stated we do not further analyze pore closure.

Resolving fusion pore during vesicle shrinking or enlargement

At fusion onset, sampled every 26-300 ms, ~21% of PH-Ω (50 of 236 PH-Ω) showed a visible pore ($Pore_v$), i.e. a pore size exceeding our STED resolution of ~60 nm (Figs. 1.3D-H). The pore in the remaining PH-Ω could not be resolved, mostly because it was below our STED resolution (13). The percentage of $Pore_v$ ($Pore_v$%) for shrink-related fusion ($shrink_{related}$-fusion), which denotes both shrink-fusion (e.g., Figs. 1.3D-E) and partial-shrink-fusion (e.g., Fig. 1.3F), was significantly larger than that for enlarge-fusion (e.g., Fig. 1.3H), but not significantly larger than that for same-size-fusion (e.g., Fig. 1.3G) (summarized in Fig. 1.3I). Results similar to those in Fig. 1.3I were obtained when pore closure events were excluded. Thus, fusion pores are larger during $shrink_{related}$-fusion than during enlarge-fusion. This finding suggests that $shrink_{related}$-fusion releases contents faster than enlarge-fusion, a conjecture which was experimentally verified, as described in the next section.

We noticed that in 3 of 14 shrink-fusion events with a $Pore_v$, following substantial shrinking of the Ω-profile so that the width had become smaller than the pore size, the Ω-shape changed into a Λ-shape during the final stages (e.g., Fig. 1.3E). Such Λ-profiles were not observed during shrink-fusion with no $Pore_v$ (31 out of 31 events, e.g., Figs. 1.1B-D). Thus, only ~7% of shrink-fusion events showed a late stage Λ-profile. These results suggest that as the shrinking Ω-profile approaches the size of its own pore, a conversion to a Λ-profile occurs before finally merging with the flat PM.

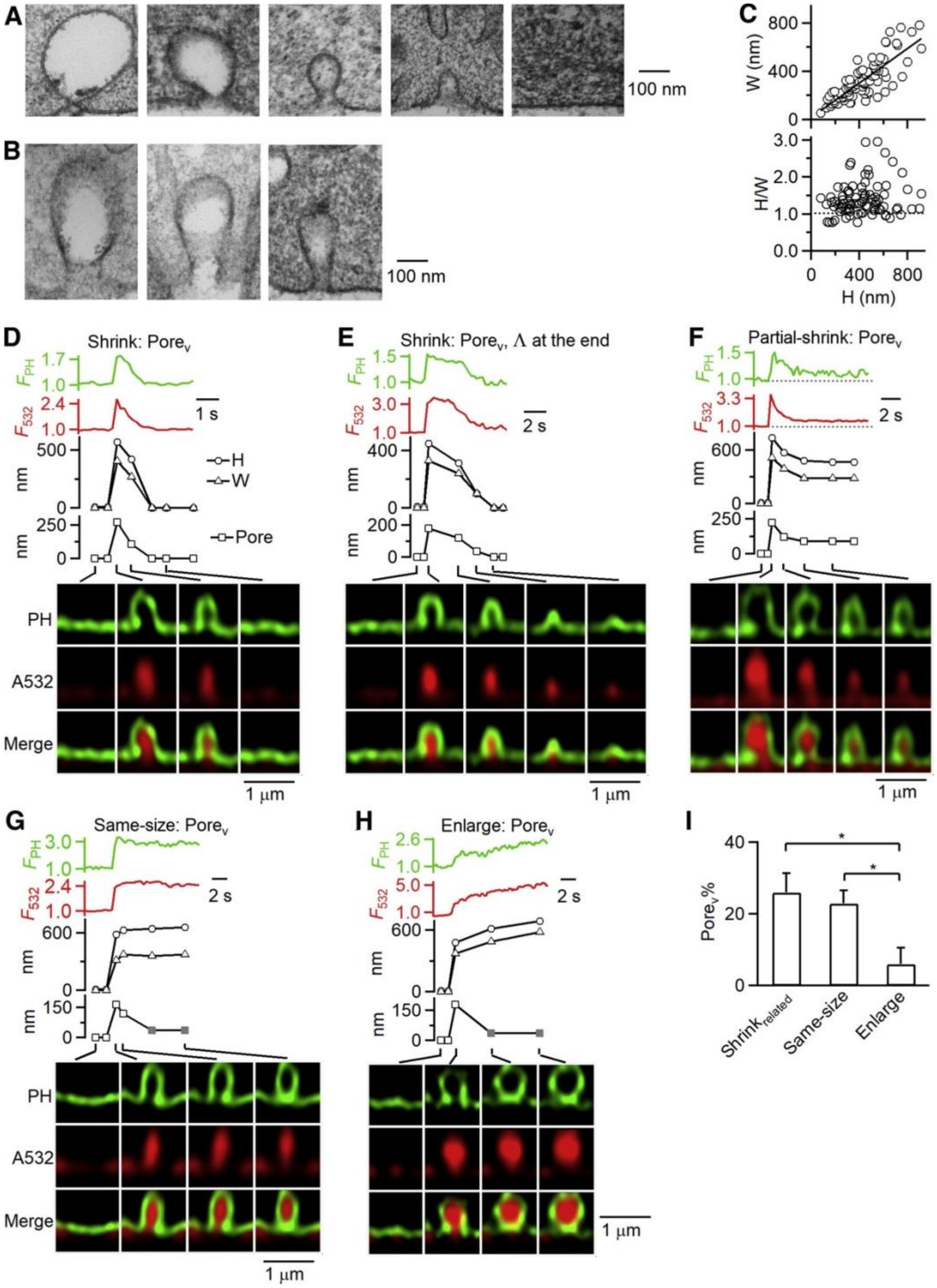

Figure 1.3. Fusion pore dynamics during shrink-, partial-shrink-, same-size- and enlarge-fusion.

(A) Electron microscopic images of Ω-profiles with different sizes. Cells were in 70 mM KCl for 90 s (applies to panels A-C). (B) Electron microscopic images of elongated Ω-profiles resembling cylinders with different sizes. (C) The width (W, upper) and the ratio between the height (H) and width (H/W, lower) of Ω-profiles observed with electron microscopy (each circle represents one Ω-profile, 84 Ω-profiles from 800 cell cross sections). The line in the upper panel is a linear regression fit (correlation coefficient: 0.81). Dotted line in the lower panel indicates H/W = 1. Most data are above the dotted line, indicating that most Ω-profiles are somewhat elongated. (D-H) F_{PH} (PH-Ω fluorescence), F_{532} (A532 fluorescence), H (PH-Ω height, circles), W (PH-Ω width, triangles), Pore (PH-Ω pore size, squares) and sampled images at times indicated with lines showing pore dynamics during shrink-fusion (D-E), partial-shrink-fusion (F), same-size-fusion (G), and enlarge-fusion (H). Gray squares (G-H): below STED resolution of ~60 nm. (I) The percentage of observing a $Pore_v$ ($Pore_v$%) during $Shrink_{related}$-fusion fusion (including shrink-fusion and partial-shrink-fusion), same-size fusion and enlarge-fusion (total fusion event number: 236; from 202 cells). *: $p < 0.05$, ANOVA.

Shrink-fusion releases contents much faster than enlarge-fusion

To determine whether shrink-fusion and enlarge-fusion are associated with different release kinetics, we overexpressed a vesicular lumen protein neuropeptide Y-EGFP (NPY-EGFP) and performed confocal imaging of NPY-EGFP with Alexa 647 (A647, in the bath) in the XY/Z_{fix} configuration ~200 nm above the cell bottom (Fig. 1.4A). $Depol_{1s}$ induced NPY-EGFP spot release (218 spots, 28 cells, Figs. 1.4B-G), accompanied by sudden A647 spot appearance and increase in A647 fluorescence (F_{647}) due to A647 diffusion from the bath to the fusion-generated Ω-profile (12).

Under strong excitation we observed four distinct patterns of evolution of A647 spots (218 spots, 28 cells) (12). First, shrink-fusion was reflected as A647 spot width shrinking until it was undetectable while F_{647} decayed to the baseline (Fig. 1.4B, 41 events). Second, the A647 spot width could shrink partially with partial F_{647} decrease, then maintaining a spot of reduced size, which reflected partial-shrink-fusion (Figs. 1.4C-D, 28 events). The reduced-size spot was sometimes followed by spot F_{647} decay to baseline while the spot size did not change further, reflecting pore closure that prevented exchange of bleached A647 in the spot with fluorescent A647 in the bath (partial-shrink-fusion with pore closure, Fig. 1.4D) (12). Third, A647 spot size and F_{647} could remain unchanged (same-size-fusion, Fig. 1.4E, 111 events), sometimes followed by F_{647} decay to baseline without spot size change (same-size-fusion with pore closure, Fig. 1.4F). Fourth, spot width and F_{647} could increase (enlarge-fusion, Fig. 1.4G, 38 events), occasionally followed by spot F_{647} decay to baseline without further change in spot size (enlarge-fusion with pore closure, not shown). Consistent with STED XY/Z_{fix} imaging, we used these A647 spot behaviours to identify shrink-fusion, partial-shrink-fusion, same-size-fusion and enlarge-fusion (12).

The percentage of shrink-fusion (19 ± 4%, n = 28 cells) and enlarge-fusion (17 ± 4.6%, n = 28 cells) were not significantly different compared to those without NPY-EGFP overexpression (shrink-fusion: 18 ± 3.4%; enlarge-fusion: 10 ± 2.3%, n = 60 cells) (12). Thus, NPY-EGFP overexpression is not crucial in determining whether vesicle undergoes shrink- or enlarge-fusion.

NPY-EGFP release was detected as decay of NPY-EGFP fluorescence (F_{NPY}, Figs. 1.4B-G) (49, 50). The F_{NPY} 20-80% decay time (T_{NPY_decay}) ranged from 12 ms – 12 s, in most cases < ~2 s. Of 218 spots, 6 did not release or else partially released NPY-EGFP, due either to rapid pore closure (5 out of 95 pore closure events) or a narrow pore (1 out of 82 same-size-fusion or enlarge-fusion without pore closure) (13). These 6 events were excluded from further analysis.

T_{NPY_decay} for $shrink_{related}$-fusion was much shorter than that for same-size-fusion, whereas enlarge-fusion showed a much longer T_{NPY_decay} than that of either same-size-fusion or $shrink_{related}$-fusion (Fig. 1.4H-I, upper; 212 events, 28 cells). Similar results were obtained when pore closure events were excluded (122 events, 28 cells), or partial-shrink-fusion was excluded from $\text{shrink}_{\text{related}}$-fusion. Thus, $\text{shrink}_{\text{related}}$-fusion and enlarge-fusion are associated with faster and slower contents release, respectively.

STED XZ/Y_{fix} imaging of FFN511 release further confirmed that $\text{shrink}_{\text{related}}$-fusion and enlarge-fusion are associated with faster and slower contents release, respectively. The 20-80% decay time of FFN511 ($T_{\text{FFN\_decay}}$) during shrink-fusion and partial-shrink-fusion, as observed with STED XZ/Y_{fix} imaging, was much shorter than that for same-size-fusion, whereas enlarge-fusion observed with STED XZ/Y_{fix} imaging showed the longest $T_{\text{FFN\_decay}}$ (e.g., Figs. 1.2B-E, summarized in Fig. 1.2F; 92 events, 71 cells). These results were analogous to different $T_{\text{NPY\_decay}}$ observed during $\text{shrink}_{\text{related}}$-, same-size- and enlarge-fusion (Fig. 1.4I).

Three sets of evidence suggest that, to facilitate content release, $\text{shrink}_{\text{related}}$-fusion employs a larger fusion pore than enlarge-fusion. First, as mentioned above, Pore_{v}% of $\text{shrink}_{\text{related}}$-fusion was significantly larger than that of enlarge-fusion (Fig. 1.3I). Second, release of either NPY-EGPF or FFN511 was fastest for $\text{shrink}_{\text{related}}$-fusion, slower for same-size-fusion, and the slowest for enlarge-fusion (Figs. 1.2F and 1.4I-upper), supporting that these different release time courses are controlled by the fusion pore size differences. Third, the F_{647} 20-80% rise time ($T_{\text{647\_rise}}$) was shortest for $\text{shrink}_{\text{related}}$-fusion, significantly longer for same-size-fusion, and longest for enlarge-fusion (Figs 1.4H and 1.4I, lower), mirroring the order of the respective $T_{\text{NPY\_decay}}$ values for the three classes of events (Figs. 1.4H and 1.4I, upper). The same order for the time course of content release and A647 entry into the fusing vesicle further suggests that this order reflects the fusion pore size differences.

Both $T_{\text{NPY\_decay}}$ and $T_{\text{647\_rise}}$ were shorter for $\text{shrink}_{\text{related}}$-fusion than for same-size fusion, (Figs 1.4H-I), suggesting that $\text{shrink}_{\text{related}}$-fusion employs a larger fusion pore than does same-size-fusion. We could not detect a difference in $\text{Pore}_\text{V}\%$ values for $\text{shrink}_\text{related}$-fusion and same-size-fusion (Fig. 1.3I), likely due to our limited STED resolution (~60 nm). Although shrink-fusion was associated with fast NPY release, shrinking was apparently not the cause of this fast release, because NPY release time, $T_\text{NPY\_decay}$ (0.14 ± 0.03 s, n = 41), was much faster than the time for the vesicle to shrink, the 20-80% decay time of F_{647} during shrink-fusion (0.80 ± 0.25 s, n = 41, t test, $p < 0.01$; e.g., Fig. 1.4B, summarized in Fig. 1.4J).

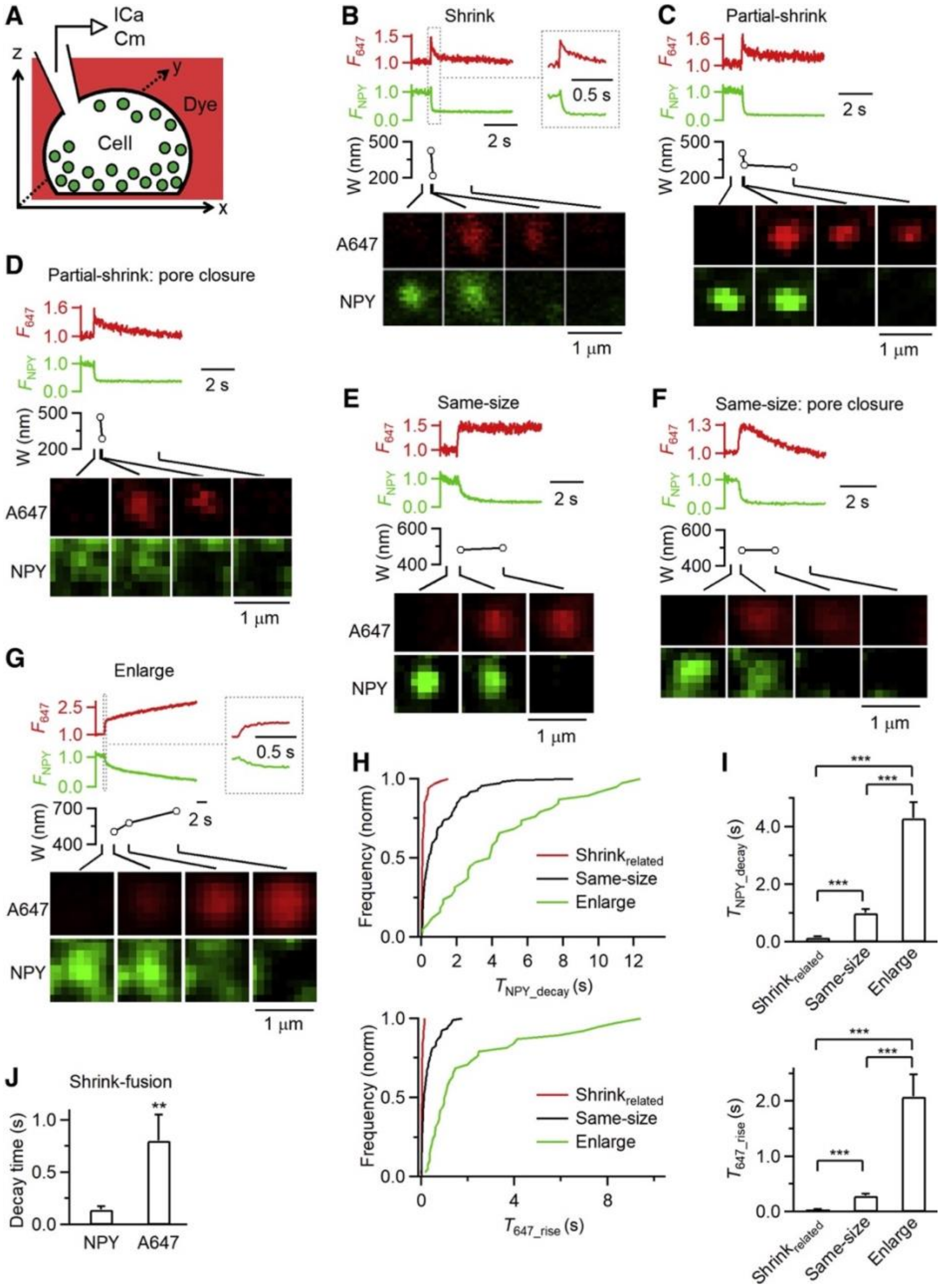

Figure 1.4. Imaging NPY-EGFP release and structural changes of A647-labelled fusing vesicles.

(A) Schematic drawing of a cell with vesicles containing NPY-EGFP (green) on the coverslip bathed with a solution containing A647 (red). (B-G) F_{647} (A647 spot fluorescence), F_{NPY} (NPY-EGFP spot fluorescence), A647 spot width (W, full-width-half-maximum), and A647/NPY-EGFP confocal XY-images at times indicated with lines for various rates of NPY-EGFP release at various fusion modes: B, shrink-fusion (inset shows traces in larger time scale); C, partial-shrink-fusion; D, partial-shrink-fusion followed by pore closure; E, same-size-fusion; F, same-size-fusion followed by pore closure; G, enlarge-fusion (inset shows traces in larger time scale). (H-I) Cumulative frequency (H, normalized) or the

mean (I, mean + s.e.m.) of T_{NPY_decay} (20-80% F_{NPY} decay time, upper) and T_{647_rise} (20-80% F_{647} rise time, lower) for $shrink_{related}$-fusion (69 events, 28 cells), same-size-fusion (111 events, 28 cells) and enlarge-fusion (38 events, 28 cells). ***: $p < 0.001$, ANOVA. (J) 20-80% decay time of NPY-EGFP (T_{NPY_decay}) and A647 fluorescence during shrink-fusion (mean + s.e.m., 41 events). A647 fluorescence decay was measured after the peak was reached. **: $p < 0.01$, t test.

Mechanisms underlying shrink-fusion

What mechanism leads to shrink-fusion, and why is this pathway preferred to the full collapse pathway envisaged in the classical picture? To address this, we mathematically modelled the merging of a fused vesicle with the chromaffin cell PM (Fig. 1.5A and Appendix) and verified the model's predictions with experimental data.

The vesicle membrane is treated as a continuous surface, with bending and osmotic pressure energy contributions following the well-established Helfrich theory (51). The membrane connects to the PM in a small area assumed free of actin cortex (Table 1.1, and Fig. 1.5A), and elsewhere the PM is assumed adhered to the actin cortex, likely via actin-binding transmembrane and membrane-associated proteins (17, 52-55). Using a method similar to a previous study (56) we obtained differential equations whose solution yielded the minimum energy shape and volume (see Appendix). All model parameters were fixed by experiment, either from the present study or published data (Table 1).

A key model assumption is that during shrink-fusion the vesicle and extracellular pressures are equal because fusion pores are large enough to allow rapid pressure equilibration, unhindered by vesicular lumen contents (Fig. 1.5A). Several observations support this assumption. First, ~26% of shrink-fusion events involved pores > 60 nm (Fig. 1.3I). Second, shrink-fusion events permitted rapid ~0.14 s release of the ~4 nm NPY-EGFP (57) (Fig. 1.4J), much faster than the Ω-profile shrinking time (~0.80 s, Fig. 1.4J, $p < 0.01$). Thus, content release precedes Ω-profile shrinking.

Consist with this, chromogranin A, a major vesicular matrix component, was released in ~0.1 s during high potassium application (58), which might induce mostly shrink-fusion (17). Once the contents are gone, pressure equilibration is almost instantaneous: even for a small 4 nm diameter pore, we estimate unhindered pressure equilibration requires only milliseconds (see Appendix).

Pressure equalization has significant consequences: since cells maintain a swelling osmotic pressure (ΔP = intracellular osmotic pressure – extracellular osmotic pressure) (59), it follows that the fused vesicle experiences a squeezing osmotic pressure ΔP, equal to the cell swelling pressure but acting in reverse (Fig. 1.5A). Computed shapes are shown in Fig. 1.5B for a typical squeezing pressure $\Delta P = 100$ Pa and vesicle sizes up to effective diameter $D = 400$ nm, typical for shrink-fusion onset. The sequence follows a shrink-fusion trajectory of mildly prolate Ω-shapes, with height-width ratios ~1.2-1.5 close to our EM measurements (Fig. 1.3C).

We calculated the free energies of the vesicle states in Fig. 1.5B and found the free energy monotonically decreased with decreasing vesicle size, demonstrating that the shrink-fusion trajectory is indeed selected (Figs 1.5B, 1.5C and Appendix). The decrease originated in the osmotic squeezing force, which deflated the vesicle and abolished its tension to negative values (Figs. 1.5D and S1.1A). Thus, a powerful membrane tension gradient reels in membrane, from the tensionless vesicle into the PM, driven by the PM tension and the PM-actin cortex adhesion forces (Fig. 1.5G). For a membrane area ΔA reeled onto the PM, we find a free energy decrease $\Delta F = -(\epsilon_{\text{adhesion}} + \gamma_{\text{PM}} - \gamma_{\text{ves}})\,\Delta A$, where $\epsilon_{\text{adhesion}}, \gamma_{\text{PM}}, \gamma_{\text{ves}}$ are the membrane-cytoskeleton adhesion energy, the PM tension and vesicle membrane tension, respectively (see Appendix).

In the late stages of the shrink-fusion sequence (Fig. 1.5B), the model generated Λ shapes similar to those in STED images (Fig. 1.3E). The Ω→Λ shape transition depended on the diameter w of the actin cortex-free zone where the vesicle joins the PM (Fig. 1.5A). For example, if

w = 80 nm, Ω→Λ transition occurred as vesicle diameter D shrank to ~56 nm (Fig. 1.5B); the transition was delayed to $D = 14$ nm if $w = 20$ nm (Figs. S1.1B-F). The merging of a Λ-shaped membrane with the PM is a full-collapse subsequence; thus, full-collapse shapes are realized only in the latest stages of the trajectory.

From the computed shapes shown in Fig. 1.5B we measured fusion pore diameters, defined as the minimum width near the PM for Ω shapes, or the vesicle width at a fixed height for Λ shapes. The latter is similar to the definition used for experimental pore size measurements (Fig. S1.1F). Down to a height of ~ 200 nm in the shrink-fusion sequence of Fig. 1.5B the pore size increases gradually from 16 to 23 nm (Fig. S1.1F), then increasing more sharply to 42 nm before decreasing to zero during the Λ shape sequence as the vesicle flattens into the PM. The qualitative behaviour is similar for larger diameters of the actin cortex-free zone w, but with somewhat larger pores (Figs. S1.1B-F). In the experiments we measured a monotonic decrease in pore size (Figs. 1.3D-E). We speculate that the more monotonic behavior observed experimentally may be associated with changes in w during the shrink episode, or with the effects of dynamin or synaptotagmin, beyond the scope of the present model (13, 60).

For even larger vesicles (e.g. $D > 400$ nm at $\Delta P = 100$ Pa) the model reproduced the remarkable tubular shapes that we observed in cells, a vivid consequence of squeezing forces (Fig. 1.5E). Tubular vesicles had large height-to-width ratios and widths that decreased with height, asymptoting a pressure-dependent width for large heights (Fig. 1.5F).

Agreeing with experiment, the model identified three vesicle classes: Ω-shaped, tubular-shaped and Λ-shaped. In Fig. 1.5F, model-predicted isobars (constant ΔP) are plotted in the vesicle height-width plane, together with the EM data of Fig. 1.3C. Each experimental point belongs to one of the three vesicle shape sectors and to a certain isobar, illustrating how measurement of vesicle shape enables the model to predict the squeezing pressure on that vesicle. The data in Fig. 1.5F suggest vesicles in cells were subject to squeezing pressures from ~40 to ~400 pa.

Four specific model predictions are confirmed by experimental observations, considerably strengthening our model's conclusions. (1) During shrink-fusion, predicted vesicle shapes have mild prolateness (height greater than width), and a late transition to Λ-shape before flattening into the PM (Fig. 1.5B). This is experimentally confirmed (Figs 1.1 and 1.3). (2) Tubular shapes are predicted for large squeezing pressures or vesicle size, a vivid manifestation of osmotic squeezing closely related to the spherical-to-prolate first order transition previously predicted for closed vesicles under high squeezing pressure (56). Tubular-shaped vesicles were predicted to be shrinking (Fig. 1.5E), consistent with our observations of large shrinking tubular vesicles (Figs. 1.1 and 1.3). (3) Lowering the osmotic squeezing driving force by increasing extracellular osmolarity, or (4) lowering the reeling-in force by compromising adhesion between the PM and the actin cortex is predicted to reduce the shrink-fusion frequency (Fig. 1.5A). Both predictions were confirmed by a recent study, where increased extracellular osmolarity or inhibition of F-actin by latrunculin A, cytochalasin D or actin knockout significantly reduced the percentage of shrink-fusion detected by confocal imaging of fusion spots (17).

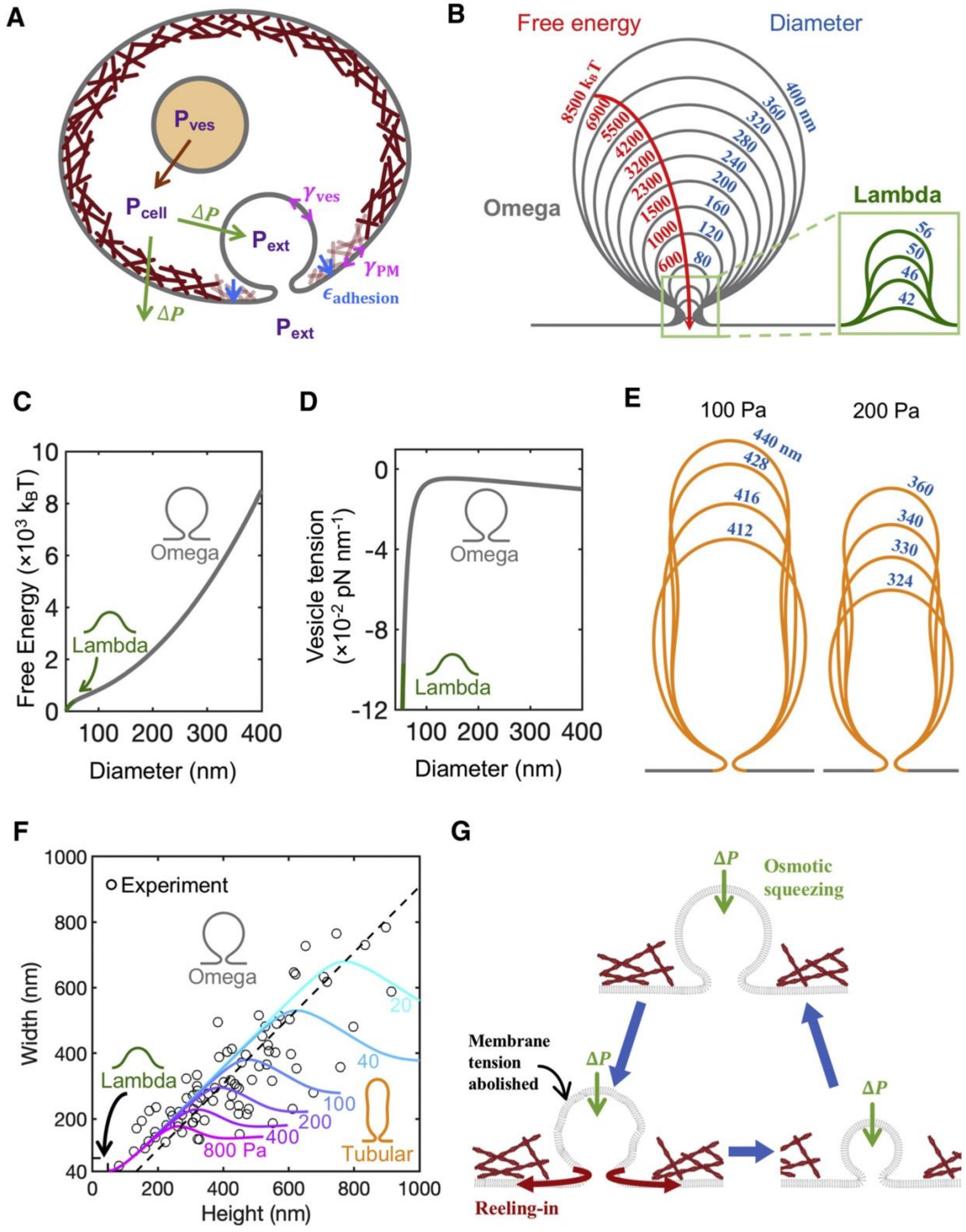

Figure 1.5.Mathematical model of vesicle evolution during exocytosis. Model parameters as in Table 1.1.

(A) Schematic of the model (not to scale). Cells maintain an outward (swelling) osmotic pressure $\Delta P = P_{\text{cell}} - P_{\text{ext}}$ (green arrow, left), with cell pressure P_{cell} exceeding

extracellular pressure P_{ext}. Intact vesicles maintain swelling pressure (red arrow), with vesicle pressure $P_{\text{ves}} > P_{\text{cell}}$. Following fusion with the plasma membrane (PM), rapid equilibration between the vesicle lumen and extracellular medium is assumed, so $P_{\text{ves}} = P_{\text{ext}}$. The vesicle osmotic pressure then equals ΔP, but is now an inwards squeezing pressure (green arrow, right). The model calculates the vesicle tension, γ_{ves}, while the PM tension, γ_{PM}, and the adhesion energy $\epsilon_{\text{adhesion}}$ to the actin cortex (maroon layer adjacent to PM) are taken from experiment (see Table 1.1). (B) Predicted Ω-shrink sequence. Computed vesicle shapes and free energies for squeezing pressure $\Delta P = 100$ Pa and the indicated effective diameters D (such that vesicle area equals πD^2). A transition occurs at $D = 56$ nm from Ω to Λ shape (defined as a profile lacking overhang). (C) Free energy versus diameter for the vesicles in panel B. (D) Vesicle membrane tensions for the vesicles in panel B. (E) Osmotic squeezing generates tubular vesicles. Predicted tubular shapes for two squeezing pressures. Tubular vesicles are predicted for large squeezing pressure or large vesicle area. (F) Three classes of vesicle shape are predicted, Ω, tubular and Λ, each corresponding to one sector in the vesicle width-height plane. Predicted isobars are shown for the indicated osmotic squeezing pressures. The electron microscopy data of Figure 1.3C are also plotted. Each experimental point belongs to one isobar, representing the predicted squeezing pressure for the observed vesicle. (G) Ω-shrink mechanism predicted by the model. Osmotic squeezing deflates the vesicle and abolishes its membrane tension, so membrane is reeled into the PM by the PM tension and PM adhesion to the actin cortex.

Table 1.1 Model parameters

Symbol	Meaning	Value	Reference
κ	Membrane bending modulus	20 k_BT	(A)
w	Diameter of actin cortex-free zone	80 nm	(B)
γ_{PM}	Plasma membrane tension	0.04 pN nm^{-1}	(C)
$\epsilon_{\text{adhesion}}$	Membrane-cortex adhesion energy density	0.02 pN nm^{-1}	(D)

(A) Ref. (61).
(B) Model solutions with w=80 nm had ~30 nm diameter fusion pores, consistent with the experimental Ω shapes of Figure 3A. The solutions exhibited a Ω-to-Λ transition at vesicle diameter 56 nm, slightly less than the STED resolution limit, consistent with the finding that 93% of shrink-fusion events lacked a visible Λ sequence in STED measurements (see main text).
(C) Ref. (62).
(D) Ref. (53).

1.3 Discussion

Recent imaging of dense-core vesicle fusion in chromaffin cells shows that fusion spots may shrink or enlarge in size, and that F-actin-dependent plasma membrane tension is needed for shrinking

(12, 17). The present work advanced over these studies in three aspects. First, with STED imaging of PH_G-labelled fused vesicular membrane dynamics and the dynamics of FFN511 release from vesicular lumen in chromaffin cells, we directly visualized, and thus verified two fusion modes associated with size changes, the shrink-fusion (or $shrink_{related}$-fusion) and enlarge-fusion (Figs. 1.1-1.3). Second, we found that $shrink_{related}$-fusion is associated with a large pore that promotes rapid content release, whereas enlarge-fusion is associated with a narrow pore that slows down content release (Figs 1.2-1.4). These two fusion modes may contribute to explain diverse release rates reported in decades of studies that had interpreted release under the framework of full-collapse and kiss-and-run fusion mode (14, 16, 40). Third, we discovered the underlying mechanism of shrink-fusion: the swelling osmotic pressure maintained by cells squeezes the Ω-profile and abolishes the Ω-profile membrane tension, producing a tension gradient (from PM to Ω-profile) that reels Ω-profile membrane into the PM (Fig. 1.5). The requirement of the PM-to-Ω-profile tension gradient explains why F-actin-dependent PM tension is needed to mediate shrink-fusion, as suggested recently (17). The squeezing pressure is equal in magnitude to the swelling osmotic pressure of the cell (17, 59, 63-65), once the fused vesicle equilibrates with the extracellular medium (Fig. 1.5A). With squeezing force and membrane-reeling-in force, Ω-profile shrinking is free energetically favoured over full-collapse (Figs. 1.5, S1.1G-H), challenging the traditional view that full-collapse is the default fusion mode (14, 16).

Our findings as summarized above, together with a recent finding that most fusion pore closure events (kiss-and-run) on average do not slow down content release (13), lead us to suggest that shrink- and enlarge-fusion are the yin and yang of fusion modes that control the rate of content release. This suggestion challenges the classical view that full-collapse and kiss-and-run serve as the yin and yang fusion modes accounting for rapid and slow release observed in endocrine cells and neurons (14, 16, 40). Decades of studies on the release rates (14, 16, 40) that interpret exocytosis with the classical view may need to be re-examined with new fusion modes reported here.

Our finding that cells use shrink-fusion instead of full-collapse to promote content release has broad implications, for two reasons. First, swelling osmotic pressure and membrane-actin cortex adhesion, both required for shrink fusion (Fig. 1.5), are general properties of cells (17, 53, 59, 63-65). Consequently, shrink-fusion may serve as the fusion mode that facilitates exocytotic content release in many cell types. Second, shrink-fusion may describe exocytosis of various sizes of vesicles, because Ω-profile shrinking was observed down to our STED resolution limit of ~60 nm (Fig. 1.1). A recent study had speculated that as the width of the Ω-profile shrinks to an extent that is smaller than its pore, Ω-profile may appear as a collapse-like ∩-shape profile before flattening at the PM (17). Modeling and imaging in the present work showed that, during the final stage of shrinking, the Ω-profile undergoes a transition to a Λ-profile (Figs 1.3 and 1.5). Indeed, such Λ-profiles, observed with electron microscopy, are the basis for the full-collapse fusion hypothesis (14, 16, 44). Thus, we propose a shrink-collapse fusion mode, in which Ω-profile shrinking is followed by a transition to a Λ-profile and then flattening, to unify the apparently contradictory observations of shrink-fusion and full-collapse.

Although vesicles smaller than 60 nm, such as synaptic vesicles (~20-60 nm), are beyond our detection limit, it is likely that these vesicles display shrink-collapse, with shrinking as the main component for larger vesicles (near 60 nm), and collapse as the main component for smaller vesicles (near 20 nm). It would be of great interest to verify this possibility in the future. The forces involved in mediating shrink-fusion, as described here (Fig. 1.5), could not account for same-size-

and enlarge-fusion. Additional unknown mechanisms must be involved in mediating same-size and enlarge-fusion.

Here we mathematically modelled shrink-fusion events, for which we assumed that the vesicle contents are released before the onset of the shrinking dynamics, based on the observed fast release of NPY-EGFP (Fig. 1.4I). However, for other event types (same-size-fusion and enlarge-fusion) NPY-EGFP release was significantly slower, so that contents may influence vesicle shape evolution. Previous studies have shown a relationship between the amount of cargo in a vesicle and its pore size. For example, overexpression of NPY-EGFP, chromogranin A-EGFP or tissue plasminogen activator-EGFP affected pore lifetimes and sizes (58, 66), and in chromogranin-knockout mice the amount of catecholamine released is lowered (67). However, in the present work with overexpression of NPY-EGFP the percentage of shrink- and enlarge-fusion was not significantly different to that in an earlier study without overexpression (12), suggesting that the initial amount of NPY-EGFP is not a crucial factor in deciding whether vesicle undergoes shrink- or enlarge-fusion. It would be of great interest to investigate this point in the future.

The mathematical model we presented elucidated the basic effects due to the biophysics of the vesicle and plasma membranes and the actin cortex. Other components such as dynamin or synaptotagmin may be relevant (13, 60), but their roles are beyond the scope of this study. Dynamin was proposed to assist constriction of fusion pores (13) . Different synaptotagmin isoforms sort to different chromaffin granule populations, and granules with Syt-1 have larger fusion pores with shorter lifetimes than granules with Syt-7 (68, 69).

Various sizes of Ω-, tubular- and Λ-profiles have been reported in electron microscopy studies (44, 70). The present work revealed that these structures can originate from the dynamic processes of shrink-, partial-shrink-, and enlarge-fusion. For example, large Ω-profiles were previously presumed to result from bulk endocytosis, phagocytosis, or compound exocytosis of large vesicles formed by vesicle-vesicle fusion (16, 40, 71). We showed that they may alternatively originate from enlarge-fusion. Enlarge-fusion may not be limited to chromaffin cells; capacitance recordings in mast cells show that the capacitance up-step is sometimes followed by a larger down-step, suggesting that retrieved vesicles can be larger than fused vesicles (72). Fusion pore closure after enlarge-fusion may thus be a mechanism to generate large endosome-like structures previously attributed to bulk endocytosis. What controls vesicle size is largely unclear; our work suggests that fusion pore closure after partial-shrink-fusion and enlarge-fusion may produce different sizes of vesicles. The origin of tubular membrane structures is unclear and often attributed to bulk endocytosis (16, 40, 71). The present work reveals that partial-shrink-fusion, mediated by the osmotic squeezing forces, may generate tubular membrane shapes. Closure of these tubular structures may thus constitute a novel mechanism to generate tubular vesicles widely observed.

1.4 Appendix: Justification and details of the mathematical model

Estimating vesicle pressure equilibration time

We estimate here an upper bound of the time required, during shrink fusion, for the pressure inside the fused vesicle to decrease and become equal to the extracellular pressure. The equilibration is assumed unhindered by vesicular contents, which are assumed released before shrink fusion commences (see main text). During this equilibration, a small volume of fluid flows out of the vesicle and the membrane tension of the fused vesicle decreases simultaneously. This tension change is due to an increase in lipid density at a constant number of lipids, as lipid flow from the vesicle to the plasma membrane is much slower than the flow of the content fluid (54). We calculate the timescale of tension relaxation below, which is the same as the timescale for pressure relaxation as the two are related according to Laplace's law.

We first estimate the volume change ΔV_{ves} needed to let the vesicle membrane tension relax to zero. We assume a linear stress-strain relation for the membrane tension (73):

$$\Delta\gamma = -\frac{E_{\text{m}}\Delta\rho}{\rho_0}, \quad [\mathbf{1.1}]$$

where E_{m} is the area expansion modulus of the vesicle membrane and ρ_0 is the lipid density under zero tension.

We assume the total number of lipids does not change as stated earlier, so the area of the membrane is inversely proportional to lipid density. Then the area change is given by $\Delta A_{\text{ves}} = -A_{\text{i}}\Delta\gamma/E_{\text{m}}$, where A_{i} is the initial membrane area. For simplicity we assume the vesicle remains a sphere, so the corresponding change in volume ΔV_{ves} to completely abolish the tension is given by

$$\Delta V_{\text{ves}} = \frac{\pi D_{\text{i}}^3 \gamma_{\text{i}}}{2E_{\text{m}}}, \quad [\mathbf{1.2}]$$

where D_{i} is the initial vesicle diameter and γ_{i} the pre-fusion vesicle tension. This volume change is relatively small compared to the initial vesicle volume V_{i} as $\Delta V_{\text{ves}}/V_{\text{i}} \approx \gamma_{\text{i}}/E_{\text{m}} \ll 1$.

The flux Q of the content fluid through a fusion pore with a diameter D_{pore} is given by $Q \sim D_{\text{pore}}^2 \bar{v}$, where $\bar{v}$ is the mean vertical velocity across the cross-section of the fusion pore. This flux is caused by the high initial vesicle pressure ΔP_{i}, set by initial tension γ_{i} following Laplace's law $\Delta P_{\text{i}} = 4\gamma_{\text{i}}/D_{\text{i}}$. The mean velocity $\bar{v}$ is estimated by the Stokes equation (ignoring inertial terms) $\eta\bar{v}/D_{\text{pore}} \sim \Delta P_{\text{i}}$, where η is the viscosity of the content fluid. Thus, the flux is given by

$$Q \sim \frac{\Delta P_{\text{i}} D_{\text{pore}}^3}{\eta}, \quad [\mathbf{1.3}]$$

The pressure relaxation time τ_{relax} is given by

$$\tau_{\mathrm{relax}} \sim \frac{\Delta V_{\mathrm{ves}}}{Q} \sim \frac{D_{\mathrm{i}}^{4}\eta}{E_{\mathrm{m}} D_{\mathrm{pore}}^{3}}. \quad [\mathbf{1.4}]$$

We use the following parameter values from experiment: D_{i} = 350 nm, the mean diameter of large dense-core vesicles in chromaffin cells (74); η = 1.1 cP, the measured cytoplasmic viscosity in fibroblast cells (75); and E_{m} = 250 pN nm^{-1}, measured expansion modulus of phosphatidylcholine bilayers (61). For a relaxation time of ~1 ms, D_{pore}~ 4 nm. This is an upper bound for the relaxation time as larger pores have been observed (Fig. 1.3D). These have much smaller relaxation times as $\tau_{\mathrm{relax}} \sim D_{\mathrm{pore}}^{-3}$.

Calculation of fused vesicle shapes

Our procedure yields the shape of a fused vesicle corresponding to an area A_{ves}, an actin cortex-free zone of diameter w, and a squeezing pressure ΔP (Table 1). Such a shape has a local balance of forces and moments, which are produced by osmotic pressure ΔP, membrane tension γ_{ves}, and force q that arises from membrane bending. The membrane bending energy is given by $F_{\mathrm{bend}} = \kappa/2 \int (2H)^2 dS$ (the integral is over the entire surface of the vesicle) (51), where κ is the bending modulus and H is the mean curvature. These force and moment balance equations stated below were derived by Jenkins (56).

We assume the vesicle shape is axisymmetric with the vertical axis being the symmetry axis. We numerically solve a system of six first order equations for the height coordinate z, the cross-sectional radius r, the angle between the tangent plane and the z-axis ϕ, mean curvature H, force that arises from bending q, and membrane tension γ_{ves}. All the six variables (except ϕ) as well as the parameter ΔP are nondimensionalized as

$$\tilde{r} = rR_{\mathrm{ves}}^{-1}, \qquad \tilde{z} = zR_{\mathrm{ves}}^{-1}, \qquad \widetilde{H} = HR_{\mathrm{ves}}, \qquad \tilde{q} = q(2\kappa)^{-1}R_{\mathrm{ves}},$$

$$\tilde{\gamma} = \gamma_{\mathrm{ves}}(2\kappa)^{-1}R_{\mathrm{ves}}^{2}, \qquad \tilde{p} = \Delta P(2\kappa)^{-1}R_{\mathrm{ves}}^{3}, \quad [\mathbf{1.5}]$$

where $R_{\mathrm{ves}} = \sqrt{A_{\mathrm{ves}}/4\pi}$. These quantities are obtained as a function of an angle S as defined by Jenkins (56), which ranges from 0 to π, where S = 0 and π denote the top and the bottom of the fused vesicle respectively (the vesicle membrane joins the cytoskeleton-attached plasma membrane at the bottom). The six first order equations are

$$\frac{d\tilde{r}}{dS} = \frac{\sin S}{\tilde{r}} \sin\phi$$

$$\frac{d\tilde{z}}{dS} = -\frac{\sin S}{\tilde{r}} \cos\phi$$

$$\frac{d\phi}{dS} = \frac{2\sin S}{\tilde{r}} \widetilde{H} + \frac{\sin S}{\tilde{r}^2} \cos\phi$$

$$\frac{d\widetilde{H}}{dS} = \frac{\sin S}{\tilde{r}^2} \tilde{q}$$

$$\frac{d\tilde{q}}{dS} = -\tilde{p}\sin S - 2\widetilde{H}\sin S\left(\tilde{\gamma} + \widetilde{H}^2 + \frac{\cos\phi}{\tilde{r}}\left(2\widetilde{H} + \frac{\cos\phi}{\tilde{r}}\right)\right)$$

$$\frac{d\tilde{\gamma}}{dS} = 0, \quad [\mathbf{1.6}]$$

for $0 \le S \le \pi$. Of the following six boundary conditions, the first is vanishing force at $\tilde{r}$ = 0 and the others are geometric constraints.

$$\tilde{q}(0) = 0, \qquad \phi(0) = \phi(\pi) = \frac{\pi}{2}, \qquad \tilde{r}(0) = 0, \qquad \tilde{r}(\pi) = \frac{\widetilde{w}}{2}, \qquad \tilde{z}(\pi) = 0, \quad [\mathbf{1.7}]$$

Here, $\widetilde{w} = w/R_{\mathrm{ves}}$ is the normalized diameter of the cortex-free zone.

These differential equations are solved using the solver ‘bvp4c’ in MATLAB® using an absolute error tolerance of 10^{-4} and a relative error tolerance of 10^{-2} (MathWorks, Natick, MA). We get the sequence of shapes and tensions along one isobar by solving these equations for different R_{ves} values, and by repeating this procedure for different ΔP values, several isobars were achieved (Fig. 1.5F). For one isobar, the vesicle adopts Ω shapes for small sizes and tubular ones for large sizes. The Ω-tubular boundary is defined as points where the vesicle width is a maximum for a given pressure value (Fig. 1.5F, dashed line).

Evaluation of free energy changes

We estimate the free energy change during shrink-fusion using the shapes and tensions of a fused vesicle at a constant squeezing pressure calculated as described above. For each shape which has area A_{ves} and volume V_{ves}, the squeezing pressure $\Delta P = P_{\mathrm{cell}} - P_{\mathrm{ves}}$ and the vesicle membrane tension γ_{ves} are related to partial derivatives of the membrane bending energy F_{bend} (76),

$$\Delta P = -\left.\frac{\partial F_{\mathrm{bend}}}{\partial V_{\mathrm{ves}}}\right|_{A_{\mathrm{ves}}}$$

$$\gamma_{\mathrm{ves}} = -\left.\frac{\partial F_{\mathrm{bend}}}{\partial A_{\mathrm{ves}}}\right|_{V_{\mathrm{ves}}}. \quad [\mathbf{1.8}]$$

The evaluation of the free energy change during shrink-fusion involves not only the membrane bending energy F_{bend}, but also the contribution from the vesicle interior (whose free energy is denoted as $F_{\mathrm{ves}}^{\mathrm{i}}$), the cell interior ($F_{\mathrm{cell}}^{\mathrm{i}}$), and the cell membrane ($F_{\mathrm{cell}}^{\mathrm{m}}$). The total free energy F is the sum of the above four free energies, given by

$$F = F_{\mathrm{ves}}^{\mathrm{i}}(V_{\mathrm{ves}}) + F_{\mathrm{bend}}(A_{\mathrm{ves}}, V_{\mathrm{ves}}) + F_{\mathrm{cell}}^{\mathrm{i}}(V_{\mathrm{cell}}) + F_{\mathrm{cell}}^{\mathrm{m}}(A_{\mathrm{cell}}), \quad [\mathbf{1.9}]$$

where V_{cell} is the cell volume and A_{cell} is the cell membrane area. We assume the chemical potential of the content molecules is the same between the vesicle and the extracellular solution, hence their free energy does not appear in F. The differential of F is given by

$$dF = \frac{\partial F_{\mathrm{ves}}^{\mathrm{i}}}{\partial V_{\mathrm{ves}}} dV_{\mathrm{ves}} + \frac{\partial F_{\mathrm{bend}}}{\partial V_{\mathrm{ves}}} dV_{\mathrm{ves}} + \frac{\partial F_{\mathrm{bend}}}{\partial A_{\mathrm{ves}}} dA_{\mathrm{ves}} + \frac{\partial F_{\mathrm{cell}}^{\mathrm{i}}}{\partial V_{\mathrm{cell}}} dV_{\mathrm{cell}} + \frac{dF_{\mathrm{cell}}^{\mathrm{m}}}{dA_{\mathrm{cell}}} dA_{\mathrm{cell}}$$

$$= -P_{\mathrm{ves}} dV_{\mathrm{ves}} - \Delta P dV_{\mathrm{ves}} - \gamma_{\mathrm{ves}} dA_{\mathrm{ves}} - P_{\mathrm{cell}} dV_{\mathrm{cell}} - \gamma dA_{\mathrm{cell}}, \quad [\mathbf{1.10}]$$

where γ is the sum of plasma membrane tension γ_{PM} and membrane-cortex adhesion energy density $\epsilon_{\mathrm{adhesion}}$ (Table 1).

As total fluid volume and membrane area are conserved, $dV_{\mathrm{ves}} + dV_{\mathrm{cell}} = 0$ and $dA_{\mathrm{ves}} + dA_{\mathrm{cell}} = 0$. Thus, the above equation can be simplified as

$$dF = (\gamma_{\mathrm{PM}} + \epsilon_{\mathrm{adhesion}} - \gamma_{\mathrm{ves}})\, dA_{\mathrm{ves}}. \quad [\mathbf{1.11}]$$

Integrating, we get the free energy of a fused vesicle with area A

$$F(A) = \int_{A_0}^{A} (\gamma_{\mathrm{PM}} + \epsilon_{\mathrm{adhesion}} - \gamma_{\mathrm{ves}})\, dA_{\mathrm{ves}}. \quad [\mathbf{1.12}]$$

The reference area A_0 is $\pi {D_0}^2$ where D_0 = 42 nm. We numerically calculated the free energy change as shown in Fig. 1.5C using the above equation with the equilibrated vesicle shapes and tensions γ_{ves} calculated as described before at a constant squeezing pressure ΔP = 100 Pa.

Free energy landscape of fusion pore dilation

We developed a Monte Carlo (MC) method to calculate the minimum energy shapes of vesicles with a fixed pore diameter, which allows determination of free energy landscape of fusion pore expansion by measuring the forces to expand or constrain the fusion pore. The contour of the axially symmetric vesicle is described by a function $r(z)$ (r and z are defined same as in the previous section) and discretized into N points ($(z_{\mathrm{i}}, r_{\mathrm{i}})$, i=1, 2, …N) which are uniformly distributed along the z axis. The MC method seeks the shape that minimizes the vesicle free energy

$$F_{\mathrm{ves}} = F_{\mathrm{bend}} + V_{\mathrm{ves}}\Delta P + \frac{k_{\mathrm{membrane}}}{2}(A_{\mathrm{ves}} - A_{\mathrm{ves}}^{0})^2 + \frac{k_{\mathrm{pore}}}{2}\left(d_{\mathrm{pore}} - d_{\mathrm{pore}}^{0}\right)^2, \quad [\mathbf{1.13}]$$

where two quadratic terms serve to constrain the vesicle membrane area A_{ves} and fusion pore diameter d_{pore} to their set values A_{ves}^{0} and d_{pore}^{0} (F_{bend}, V_{ves} and ΔP are defined same as in the previous section). The vesicle membrane tension is given by $\gamma_{\mathrm{ves}} = k_{\mathrm{membrane}}(A_{\mathrm{ves}} - A_{\mathrm{ves}}^{0})$ and the force to constrain the fusion pore $f_{\mathrm{pore}} = k_{\mathrm{pore}}(d_{\mathrm{pore}} - d^{0}_{\mathrm{pore}})$, which are obtained from partial derivatives of F_{bend}. As one expands the fusion pore, the variation of the free energy of the vesicle with respect to fusion pore diameter d is given by

$$F_{\mathrm{expansion}}(d) = \int_{d_0}^{d} -f_{\mathrm{pore}}\, d(d_{\mathrm{pore}}), \quad [\mathbf{1.14}]$$

where d_0 is the fusion pore diameter of the reference state.

The simulation investigates the free energy landscape of fusion pore expansion of a fused vesicle with effective diameter D = 200 nm ($A_{\mathrm{ves}} = \pi D^2$) with subject to a squeezing pressure ΔP = 100 Pa, and the reference state is d_{pore} = 6 nm. The vesicle contour is discretised into N = 401 points. To ensure the calculated vesicle area and fusion pore diameter fall within $\pm$1% of the set value, k_{membrane} = 4×10^{-6} pN nm^{-3} and k_{pore} = 10^{3} pN nm^{-1} were chosen. The simulation runs at zero temperature and a move that generates a new shape will be accepted only if it leads to a lower free energy F_{ves}. Each move is either a local radial change (neighbouring r_{i}) with a maximum displacement of 10^{-4} nm or a change in vesicle height of 10^{-4} nm (all z_{i} scale with the same factor). All the simulations are equilibrated after 2×10^{8} MC steps as in the final 2×10^{7} steps F_{ves} only decreases by ~ 0.05 k_BT.

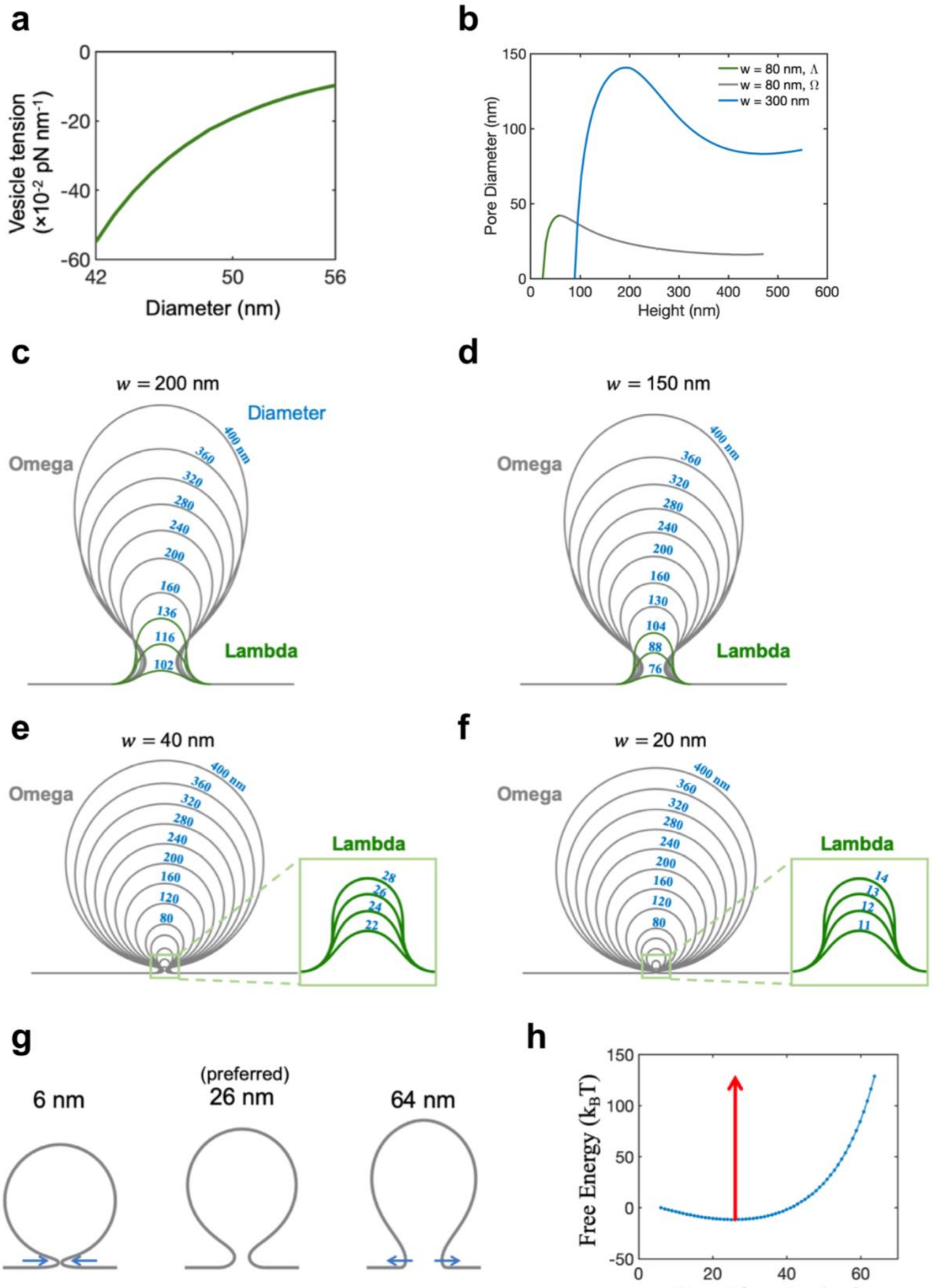

a
Vesicle tension (×10^{-2} pN nm^{-1})
0
-20
-40
-60
42
50
56
Diameter (nm)
b
Pore Diameter (nm)
150
100
50
0
0
100
200
300
400
500
600
Height (nm)
w = 80 nm, Λ
w = 80 nm, Ω
w = 300 nm
c
$w = 200$ nm
Diameter
Omega
400 nm
360
320
280
240
200
160
136
116
102
Lambda
d
$w = 150$ nm
Omega
400 nm
360
320
280
240
200
160
130
104
88
76
Lambda
e
$w = 40$ nm
Omega
400 nm
360
320
280
240
200
160
120
80
Lambda
28
26
24
22
f
$w = 20$ nm
Omega
400 nm
360
320
280
240
200
160
120
80
Lambda
14
13
12
11
g
6 nm
(preferred)
26 nm
64 nm
h
Free Energy (k$_B$T)
150
100
50
0
-50
0
20
40
60
Pore Diameter (nm)

Figure S1.1. Modelling of Ω-profile shrinking, Related to Figure 1.5.

(A) Vesicle membrane tension versus effective diameter D (vesicle area equals πD^2) for Λ-shape of Fig. 1.5B. (B-E) The predicted sequences of shapes are calculated for diameter of actin cortex-free zone w equal to (B) 300 nm, (C) 150 nm, (D) 40 nm and (E) 20 nm, respectively. The four sequences show that the Ω-to-Λ transitions in the shrink trajectory occur at effective diameter D of (B) 202 nm, (C) 104 nm, (D) 28 nm and (E) 14 nm, respectively. Conclusion: a large w leads to earlier Ω-to-Λ transition while for small w values, Λ shapes are adopted at smaller sizes. (F) Vesicle pore diameter versus vesicle height with diameter of actin cortex-free zone w equal to 80 nm (solid line) or 300 nm (dashed line). The largest vesicle in each sequence has an effective diameter of 400 nm. For Λ shapes, the pore diameter is defined to be the vesicle width at fixed height. This height is chosen to be the height of the fusion pore of the last Ω-shaped vesicle before the transition to the Λ regime. (G) Three examples of minimum energy shapes of fused vesicles calculated with Monte Carlo method. The constrained pore diameter for each shape is shown in the label above. The vesicle diameter is 200 nm. The energetically preferred pore diameter is ~26 nm as at that diameter no external force is needed to constrain the pore size. (H) Free energy landscape of fusion pore expansion. An energy barrier of ~140 k_BT (red arrow) is needed to expand the fusion pore from the preferred size to 80% of the diameter of the actin cortex-free zone.

Chapter 2: Three membrane fusion pore families determine the pathway to pore dilation

In this chapter, I describe theoretical work on solving exact fusion pore shapes and determining the pathway to pore dilation. This work has been made available on bioRxiv. Shuyuan Wang and Zachary McDargh, two former members in the O'Shaughnessy group, also contributed to this work.

2.1 Introduction

Phospholipid membranes are essential to life as enforcers of compartmentalization, providing impermeable yet flexible surfaces whose highly adaptable shapes readily adjust to enclose compartments and maintain specialized conditions and contents within (77-79). Consisting of ~5nm thick phospholipid bilayers dressed with transmembrane proteins, channels, receptors and other machineries (80, 81), cell membranes are used to enclose diverse compartments, from ~ 50 nm synaptic vesicles for neurotransmitter release to ~100-400 nm dense core vesicles for secretion of hormones such as insulin (2, 82, 83), to large organelles (84) and the cell itself.

The most extreme demands on membrane shape occur during processes such as secretion and trafficking, when membranes of different compartments undergo topological change by membrane fusion, resulting in a membrane fusion pore connecting the compartments (16). Here we consider purely lipidic fusion pores (85), but the initial fusion pore in cells has also been proposed to be proteinaceous, lined by a complex of transmembrane domains of the SNARE proteins syntaxin and synaptobrevin (86-89). The simplest membrane shape is the sphere, a surface of minimal area that also minimizes the membrane bending energy, adopted by closed secretory vesicles. Much less is established about the shapes and dynamics of fusion pores.

At neuronal synapses, the cellular fusion machinery creates a fusion pore within less than a millisec of presynaptic calcium influx, inferred from delay times in electrophysiological measurements of excitatory postsynaptic currents (90). Conductance measurements at the Calyx of Held revealed minimum synaptic vesicle pore diameters of ~ 1 nm that can flicker repeatedly. A historic development was the use of microelectrodes to detect the far slower release from non-synaptic secretory cells which showed that the initial fusion pore is very small but often dilates dramatically after a delay (20). In amperometry recordings this is indicated by a flickering low amplitude 1-50 ms "foot" signal that abruptly transits to a spike (18, 91, 92). In neuroendocrine chromaffin cells, pores can dilate to ~ 100 nm and remain open for >30 sec (13, 93). Fusion pores are mechanosensitive, as higher membrane tension correlates with larger pores and favors full fusion and contents release over partial release ("kiss-and-run") (17, 94).

The sizes, shapes and evolution of fusion pores are critical to exocytosis, when secretory vesicles fuse with target membranes and release contents through pores. The narrow initial pore may serve as a molecular sieve to modulate size and rate of vesicle cargo release (10, 21), while full release requires the pore to dilate. For example, fusion events at synaptic terminals may result in partial or total neurotransmitter release, depending on whether the nascent pore dilates fully or reseals, with important consequences for synaptic activity (11, 14). Pore dilation is assisted by SNARE proteins and Synaptotogamin (Syt) (23, 24, 95), components of the cellular fusion machinery (9, 96, 97), but the membrane energy barriers they must overcome to dilate pores are not known. Impaired pore expansion is associated with disease such as type 2 diabetes where insulin release is misregulated (22). Membrane fusion pores are also used for host cell entry by membrane-enveloped viruses such as influenza, HIV and SARS coronaviruses, whose genomes enter via a fusion pore following fusion of the viral and host membranes by specialized glycoproteins (98-100).

Theoretical works have sought to establish fusion pore shapes between two planar membranes, accounting for free energy contributions from membrane tension (tending to minimize area) and from surface bending energy (51). Fusion pores were predicted, but the shapes were assumed to belong to a particular class, either toroidal, ellipsoidal, or a combination of catenoidal and cylindrical (101-103), or were approximated by polynomials (102, 104). Continuum models and MARTINI simulations showed pores that bowed outwards beyond the planar membranes (104, 105). These studies identified a single family of narrow fusion pores, with minimum diameter < 10 nm. By contrast, an important recent study found exact solutions minimizing the Helfrich free energy corresponding to three fusion pore families, using freely hinged boundary conditions at the membrane edges (106). Membrane tethers are structures closely related to fusion pores, typically pulled from cells or artificial liposomes by optical tweezers that use the measured pulling force to infer membrane tension (53, 54). Rigorous analysis showed that long tethers approach a cylindrical shape, with a more complex transition region where the tether attaches to the planar membrane (107, 108).

Classical soap films are a natural reference point for the study of microscopic membrane surfaces. These macroscopic surfactant-stabilized water films have surface tension and thus if equilibrated adopt surfaces minimizing the area, including the spherical soap bubble. Another classical shape is the catenoid. Given two planar soap films enclosed by hoops, if the films become fused the preferred shape is the catenoid, the minimal area open surface given the constraints (109). In fact two catenoidal solutions exist, but only the wider catenoid family is stable. Bending energy is unimportant for macroscopic soap films, but for the microscopic scales of cell membranes this component becomes significant so the selected surface shape minimizes the sum of the tension and bending energies, the Helfrich free energy (51). A natural question is whether microscopic membrane fusion pores adopt catenoid or catenoid-like solutions similar to soap films. The study of ref. (106) showed that when bending energy features, the second thinner catenoid family can also be realized if the far field boundary conditions are freely hinged (106).

Here we obtain exact shapes and energetics of fusion pores between planar membranes by minimizing the Helfrich free energy (51). With simplified freely hinged boundary conditions, appropriate to soap films, there are three families as reported by Powers et al. (106): the wide and thin catenoids and the tether-like family. We show the thin catenoid is unobservable in soap films, being locally stable for membrane tensions within a band whose width decreases with increasing membrane size. Accounting properly for bending constraints from the planar membranes, we find three fusion pore families with shapes and energetics close to those of the freely hinged families. We propose that the nascent fusion pore generated by the cellular fusion machinery during exocytosis is the quasi-thin catenoid, whose dilation is a transition to the quasi-wide catenoid as observed in amperometric foot-to-spike transitions (18, 91, 92). The transition energy barrier is set by the unstable tether intermediate and is lowered by membrane tension, consistent with experiments showing facilitated dilation at higher tensions (17, 94). Finally, we study nanodiscs, model systems allowing long time measurements of stabilized pores (23, 24). We show that nanodiscs stabilize fusion pores by locking them into the thin catenoidal fusion pore family.

2.2 Results

Mathematical model of the fusion pore

During exocytosis, content molecules are released through the fusion pore, the initial connection between the fused vesicle and cell membrane. We consider a somewhat simpler geometry, a fusion pore between two planar membranes of diameters D_{mb}^{1} and D_{mb}^{2}, separated by distance h maintained by a force f (Fig. 2.1A). The classic Helfrich free energy (51) F includes contributions from bending F_{bend} and tension F_{tension},

$$F = F_{\mathrm{bend}} + F_{\mathrm{tension}} = \frac{\kappa}{2}\int (2H)^2 \, dS \; + \gamma \int \, dS \, , \qquad [\mathbf{2.1}]$$

where κ is the bending modulus, $H = (c_1 + c_2)/2$ is the mean curvature, the average of the two principal curvatures c_1 and c_2, γ is the membrane tension, and the integral is over the membrane surface S. We take $\kappa = 20$ kT (61).

An equilibrium fusion pore shape $\underline{\boldsymbol{X}}$ satisfies $\delta F(\underline{\boldsymbol{X}})/\delta \underline{\boldsymbol{X}} = 0$, which leads to the shape equation (see refs. (108, 110)),

$$2\kappa(\nabla^2 H + 2H^3 - 2HK) - 2\gamma H = 0, \qquad [\mathbf{2.2}]$$

where ∇^2 is the Laplace–Beltrami operator on the surface and K is the Gaussian curvature defined as the product of the two principle curvatures.

Assuming an axisymmetric fusion pore shape for simplicity, with the vertical axis z being the symmetric axis (Fig. 2.1B), the fusion pore is a surface generated by revolution of a curve in the meridian plane. Parameterizing this contour curve by its arclength s, the shape equation Eq. **2.2** is then expressed as an ordinary differential equation involving the vertical coordinate $z(s)$, the cross-sectional radius $r(s)$, and the tangent angle $\phi(s)$ (107) (Fig. 2.1B, and see Appendix for a derivation),

$$\phi''' = -\frac{1}{2}(\phi')^3 - \frac{2\cos\phi}{r}\phi'' + \frac{3\sin\phi}{2r}(\phi')^2 + \frac{3\cos^2\phi - 1}{2r^2}\phi' + \frac{\gamma}{\kappa}\phi' - \frac{\cos^2\phi + 1}{2r^3}\sin\phi$$
$$+ \frac{\gamma}{\kappa}\frac{\sin\phi}{r} \, , \qquad [\mathbf{2.3}]$$

where prime denotes derivative with respect to s. This is the same shape equation as for the tether analysis of ref. (107), but our boundary conditions (BCs) are different: the membrane tangent points inwards at the outer edge of both upper and lower membranes, $dr/ds > 0$ at $z = h/2$ and $dr/ds < 0$ at $z = -h/2$ (Fig. 2.1B). In ref. (107) the upper membrane tangent points outwards at the edge.

Three fusion pore families: wide catenoid, thin catenoid, tether

A proper treatment must account for the bending constraints from the upper and lower planar membranes. However, it is helpful to first study solutions to the shape equation, Eq. **2.3**, for the simplified case of freely hinged BCs (Fig. 2.1A, zero torque, or equivalently $H = 0$) at the boundary of the planar membranes, appropriate to macroscopic soap films which have tension but cannot support bending stress (111, 112). We consider first equal membranes, $D_{\mathrm{mb}}^{1} = D_{\mathrm{mb}}^{2} \equiv D_{\mathrm{mb}}$. As shown previously (106, 113), there are three fusion pore solutions: two catenoids and one tether-like solution (Fig. 2.1C). The stability of the three solutions will be discussed in later sections.

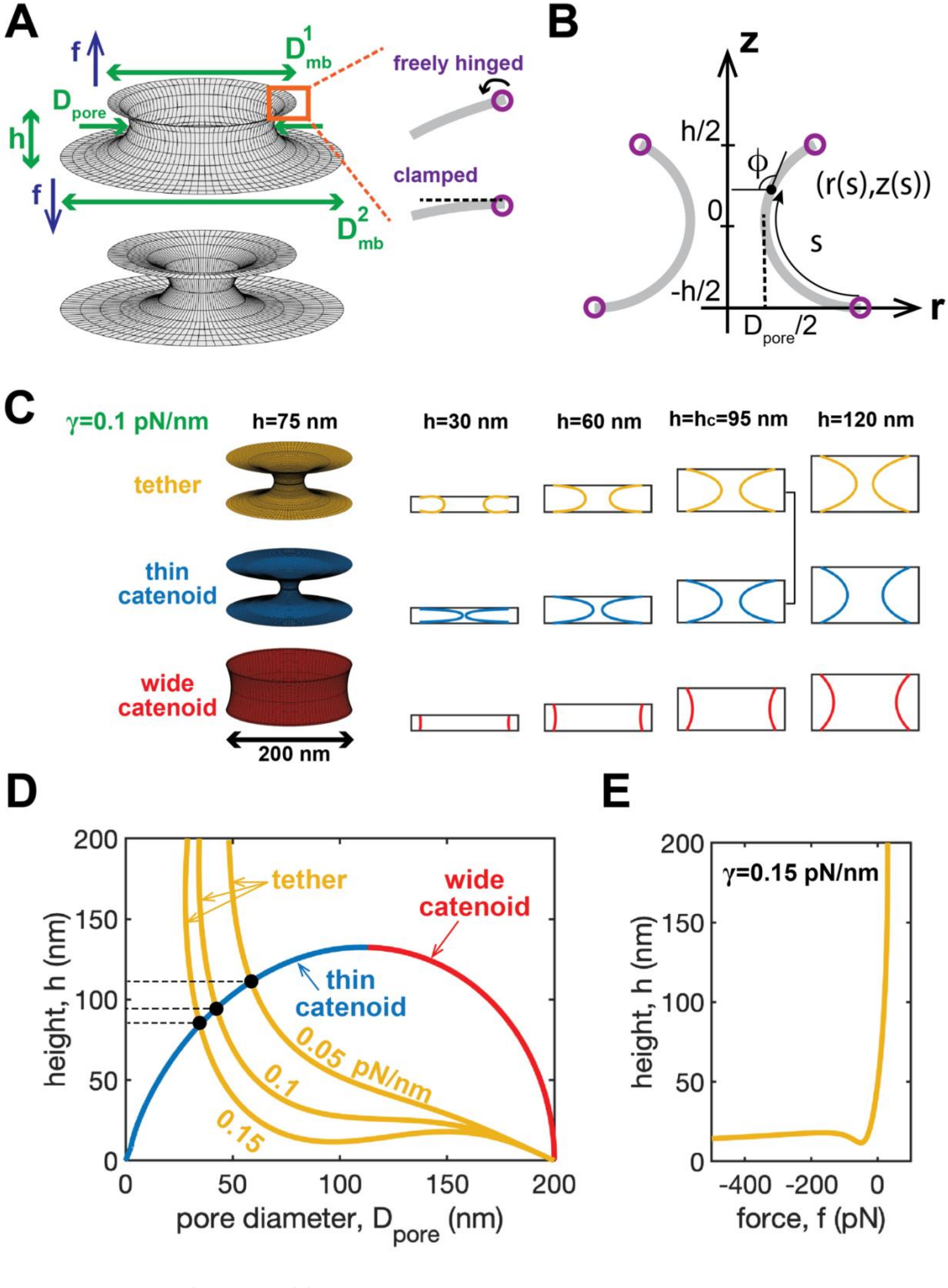

Figure 2.1. Three families of fusion pores between two planar membranes.

(A) We study fusion pores between two planar membranes of diameters D_{mb}^{1} and D_{mb}^{2} with a separation h maintained by a force f. Two boundary conditions (BCs) are considered, with and without bending constraints from planar membranes (clamped and freely hinged, respectively). Freely hinged BCs describe soap films, but proper treatment of microscopic membranes requires clamped BCs. The fusion pore diameter D_{pore} is the minimal cross-sectional diameter. (B) Coordinate system of an axisymmetric fusion pore. (C) The three fusion pore families for freely hinged BCs. Examples of the wide catenoid, thin catenoid and tether family are shown for $D_{\mathrm{mb}} = 200$ nm and membrane tension $\gamma = 0.1$ pN/nm. At the critical separation $h_{\mathrm{c}} \sim 95$ nm, the tether and thin catenoid are identical. (D) Pore diameter vs membrane separation for the three families (freely hinged BCs). The two catenoids do not depend on membrane tension, while the tether becomes thinner at higher tension. For high tensions the tether diameter depends non-monotonically on membrane separation. (E) For high tensions the tether requires a non-monotonic compressive force to maintain the pore height.

Wide and thin catenoids. The freely hinged BCs allow for two catenoidal solutions (106, 108). Consider first a fusion pore that is a minimal surface (114), locally minimizing the membrane area A and the tension contribution to the free energy of Eq. **2.1**, $\delta^{(1)} F_{\mathrm{tension}} = \gamma \delta^{(1)} A = 0$.Parameterizing the surface $\underline{\boldsymbol{X}}(u, v)$ with coordinates (u, v), the surface area element $dS = g^{1/2} du dv$. Thus, a minimal surface satisfies (115) (see SI Text for a derivation)

$$\delta(dS) = -2 g^{\frac{1}{2}} H \psi \, du dv = 0, \qquad [\mathbf{2.4}]$$

for arbitrary variation $\delta\underline{\boldsymbol{X}}$. Here g is the determinant of the metric tensor and ψ is the normal component of $\delta\underline{\boldsymbol{X}}$ (the tangential component reparametrizes the surface without affecting A). Thus, a minimal surface has zero mean curvature, H (114). Expressing H in terms of our coordinate system $r(z)$ for an axisymmetric surface and solving $H = 0$ leads to the general catenoidal solution (108),

$$r(z) = \frac{D_{\mathrm{pore}}}{2} \cosh(\frac{2z}{D_{\mathrm{pore}}}), r\left(\pm\frac{h}{2}\right) = \frac{D_{\mathrm{mb}}}{2}, \qquad [\mathbf{2.5}]$$

where D_{pore} is the pore diameter, the minimal cross-sectional diameter (Fig. 2.1A). For a given pore height h, two values of D_{pore} satisfy the BCs of Eq. **2.5**: $D_{\text{pore}} = D_{\text{pore}}^{\text{wide}}$ (wide catenoid) and $D_{\text{pore}} = D_{\text{pore}}^{\text{thin}}$ (thin catenoid), see Fig. 2.1.

Since the mean curvature $H = 0$, the catenoid simultaneously minimizes the positive definite bending free energy, $\kappa/2 \int (2H)^2 \, dS$, and satisfies the freely hinged BCs. Thus, both catenoids satisfy $\delta^{(1)}F = 0$ (Eq. **2.1**). Since the catenoids minimize the area regardless of membrane tension γ, the catenoidal solutions are unaffected by the value of γ. Note the freely hinged BC ($H = 0$) guarantees an exact catenoid solution as the BC cost no additional bending energy.

Tether. Numerical solution of Eq. **2.3** yields a third "tether" solution family (106) in addition to the two catenoids. For illustration Fig. 2.1C shows tethers for $D_{\text{mb}} = 200$ nm (similar to the size of a dense-core vesicle (74, 116)) and membrane tension $\gamma = 0.1$ pN/nm (117). For large separations, the third tether solution adopts almost cylindrical shapes whose radius equals the capillary length $\lambda \equiv (\kappa/2\gamma)^{1/2}$, similar to a tether pulled from a membrane (107, 108). For small separations, tethers require a compressing force ($f < 0$) between the two planar membranes, unlike catenoids (Fig. S2.1). In contrast to the two catenoids, the shape of the tether solution is tension-dependent (Fig. 2.1D). For small tensions, the tether has monotonically decreasing pore diameter with increasing membrane separation. However, above a certain tension, neither the pore diameter nor the compressing force f are monotonic (Figs. 2.1D, 2.1E, S2.2). Notably in studies of tether pulling (107, 108), an oscillation in the force-height plane was also found for larger h values where a cylindrical tether starts to form, but unlike our study those tethers are under a positive pulling force. Regardless of membrane tension, the tether branch always intersects the thin catenoid branch at a critical separation h_c where the two branches share the same shape (Figs. 2.1C, D). The critical separation decreases with membrane tension.

The thin catenoid is stable on nanoscales

Thus far we have used the shape equation, Eq. **2.3**, to determine equilibrium fusion pore shapes. However, whether an equilibrium shape can be observed depends on its stability. Only the fusion pore shapes that locally minimize the free energy F can be realized. Thus, we next considered the second variation of the Helfrich energy $\delta^{(2)}F$ of each catenoidal surface to determine whether it is positive definite.

Soap films: wide catenoids. For macroscopic soap films, the bending energy is a negligible contribution, so $F \approx \gamma \int dS$ in Eq. **2.1** (118). Thus, stability of a soap film depends only on the second variation of the film area A, $\delta^{(2)}A$. Under an arbitrary deformation $\delta\underline{\boldsymbol{X}}$ whose normal component is ψ, the second variation can be expressed as (119)

$$\delta^{(2)}A = \frac{1}{2}\int \psi L\psi \, dS, \quad [\mathbf{2.6}]$$

where the operator $L \equiv -\nabla^2 + 2K$ and the integral is over the reference surface (in our case the exact catenoidal surface, Eq. **2.5**). We consider the eigenvalue problem $L\psi = 4\lambda\psi/D_{\text{pore}}^2$, which becomes a Sturm-Liouville problem when we parameterize the axisymmetric deformation $\psi(v)$ by the normalized vertical coordinate $v \equiv 2z/D_{\text{pore}}$ (Fig. 2.1B, see Appendix for a derivation) (109),

$$\psi'' + \frac{2}{\cosh^2 v}\psi + \lambda \cosh^2 v \, \psi = 0, \quad [\mathbf{2.7}]$$

where prime denotes derivative with respect to v and the boundary conditions are $\psi(\pm h/D_{\text{pore}}) = 0$. Note that the thin and wide catenoids have distinct sets of eigenvalues and eigenfunctions determined by the ratio D_{pore}/h. Numerically solving the eigenvalues and the eigenfunctions of Eq. **2.7**, it can be shown that for wide catenoids all the eigenvalues are positive, while for thin catenoids one of the eigenvalues is negative, $\lambda_1 < 0$ (109) (Fig. S2.3).

An arbitrary deformation ψ can be expressed in terms of the eigenfunctions ψ_{i} $(i = 1,2, \dots)$ of Eq. **2.7**, $\psi = \sum_i c_{\mathrm{i}}\psi_{\mathrm{i}}$ (c_{i} are constants), and the second variation in the area is $\delta^{(2)}A = \pi \sum_i \lambda_{\mathrm{i}} c_{\mathrm{i}}^2$ where $\lambda_1 < \lambda_2 < \cdots$ are the eigenvalues of Eq. **2.7**. Thus, whether a deformation mode ψ_{i} contributes negatively or positively to $\delta^{(2)}A$ depends on the sign of the corresponding eigenvalue λ_i. With all $\lambda_i > 0$, $\delta^{(2)}A$ is always positive for wide catenoids and they can stably exist, as observed in soap film experiments (120). In contrast, thin catenoids are unstable as the first deformation mode ψ_1 makes $\delta^{(2)}A$ negative ($\lambda_1 < 0$).

Cellular membranes: wide and thin catenoids. On cellular scales (nm to μm) bending energy is important, so the second variation $\delta^{(2)}F$ of the full Helfrich energy Eq. **2.1** must be considered. For a catenoid whose mean curvature H is zero, $\delta^{(2)}F$ given a normal deformation ψ can be greatly simplified to (119) (see SI text)

$$\delta^{(2)}F = \frac{\kappa}{2}\int \psi[-\nabla^2 + 2K]^2\psi\, dS + \frac{\gamma}{2}\int \psi(-\nabla^2 + 2K)\psi\, dS$$

$$= \int \frac{\kappa}{2}\psi L^2\psi + \frac{\gamma}{2}\psi L\psi\, dS, \qquad [\mathbf{2.8}]$$

where the integral is over the catenoidal surface. Thus, using the same eigenvalues λ_i and eigenfunctions ψ_i of Eq. **2.7**, we obtain (see SI Text for derivation)

$$\delta^{(2)}F = \sum_{i=1}^{\infty} \lambda_i \left(\frac{D_{\mathrm{pore}}^2\gamma}{4\kappa} + \lambda_i\right)\frac{4\pi\kappa}{D_{\mathrm{pore}}^2} c_i^2. \qquad [\mathbf{2.9}]$$

A stable catenoid requires positive definite$\delta^{(2)}F$ such that $\lambda_i(D_{\mathrm{pore}}^2\gamma/4\kappa + \lambda_i) > 0$ for any deformation mode ψ_{i}. Consider positive membrane tension γ. Then wide catenoids are always stable, as all eigenvalues are positive, but since a thin catenoid has one negative eigenvalue, $\lambda_1 < 0$, it is stable only if its spatial dimensions are sufficiently small, $D_{\mathrm{pore}}^2 < 4\,|\lambda_1|\,\kappa/\gamma$, or equivalently $h < h_c$ where h_c is the critical membrane separation corresponding to this upper limit for pore size. These stable and unstable regions are shown in Fig. 2.2D. Note that the limit of stability $h = h_c$ on the small catenoid solution is precisely the point where the curve intersects the tether solution, Figs. 2.1D, 2.2A. Thus, increasing membrane separation beyond the critical point, $h > h_c$ (at fixed tension), the small catenoid becomes unstable and is replaced by the tether. This is an example of a bifurcation occurring when a solution becomes unstable, qualitatively similar to the behavior of a spherical vesicle under pressure (56): above a critical pressure, the spherical solution becomes unstable and two new solution branches appear, prolate and oblate. The stable prolate shape replaces the sphere.

Stability can also be phrased in terms of tension, γ. For wide catenoids, the lowest eigenvalue γ_1 sets a negative lower bound on the tensions for which stability holds. For thin catenoids the negative lowest eigenvalue and lowest positive eigenvalue, λ_1 and λ_2, set an upper and lower bound on tension, respectively. Thus

$$\gamma > -\lambda_1 \gamma_0, \quad \text{stable wide catenoid}$$

$$-\lambda_2 \gamma_0 < \gamma < |\lambda_1| \gamma_0, \quad \text{stable thin catenoid}$$

$$\gamma_0 \equiv 4\kappa / D_{\mathrm{pore}}^2 \qquad [\mathbf{2.10}].$$

Since the characteristic tension γ_0 decreases with increasing spatial dimension (measured by D_{pore}), it follows that thin catenoids are observed only at small scales: as the scale increases the band of tensions where thin catenoids are stable shrinks and tends to zero, Fig. 2.2D. Thus, at macroscopic scales (soap films) only wide catenoids are seen. Thin catenoids are specific to scales found in cells. For example $\gamma_0 \sim 10^{-1}$ pN/nm for $D_{\mathrm{pore}} \sim 50$ nm and κ =20 kT (61), comparable to cellular membrane tensions (121). These results are consistent with ref. (106) where the buckling transitions of fixed-area catenoidal membranes were studied.

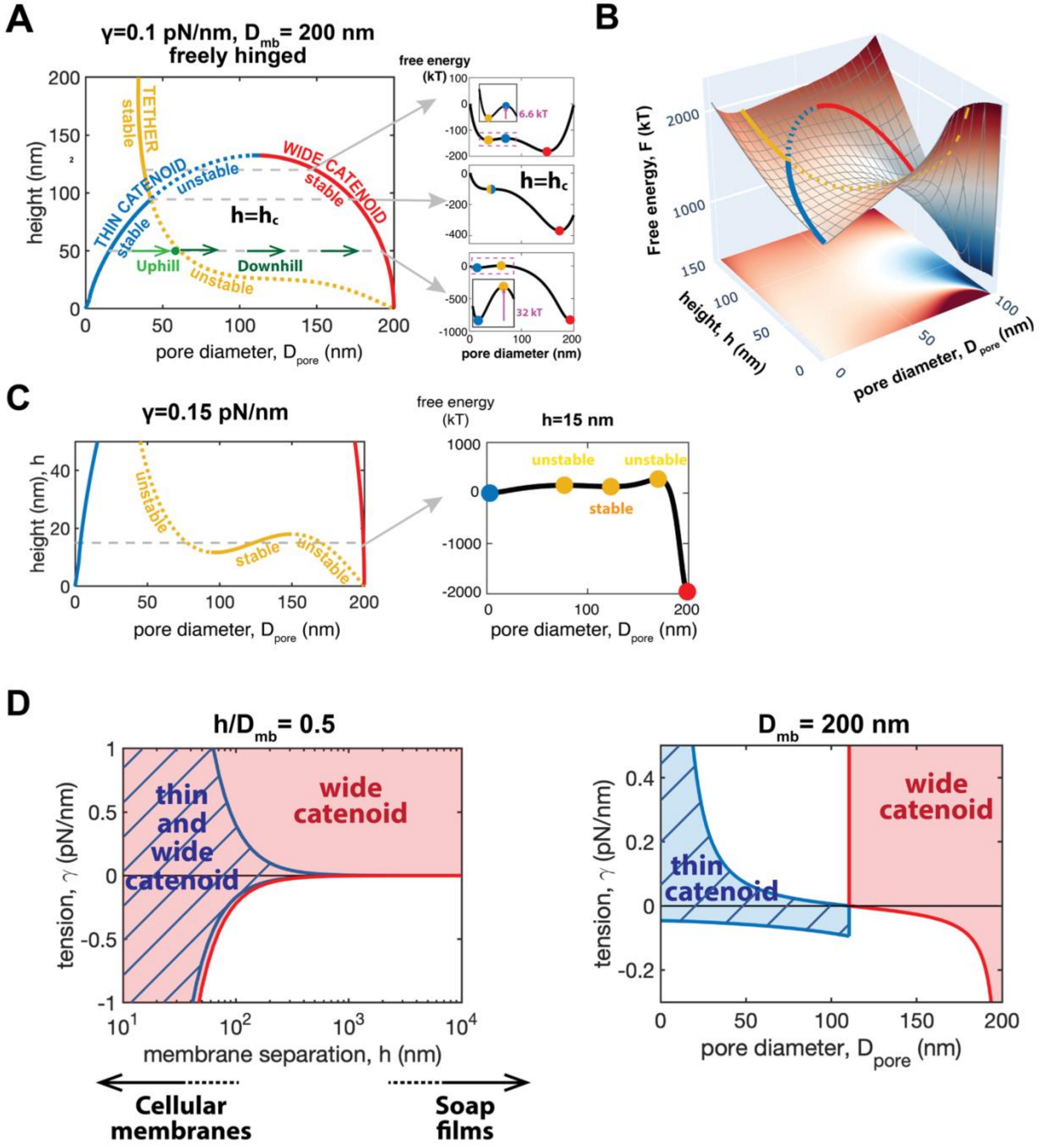

Figure 2.2. Two microscopic catenoidal fusion pores are observable between freely hinged membranes.
(A) Stability of the three fusion pore families. At sufficiently small membrane separation, thin and wide catenoids are both stable. Free energy landscape is shown for three h values (right). The stable (unstable) fusion pores localize in valleys (ridges). Pore dilation from a

thin to wide catenoid requires surmounting an energy barrier set by the tether. At the critical height h_c the tether and the thin catenoid coincide. (B) Free energy landscape. (C) For higher membrane tensions and sufficiently close membrane there are five pore families, three of which are stable. (D) Thin catenoidal fusion pores are only observable on microscopic scales within band of tensions which shrinks to zero on macroscopic scales.

Free energy landscape for fusion pore expansion

The three families (thin catenoid, wide catenoid and tether) are different minimum energy fusion pore shapes with different fusion pore diameters, D_{pore}. Each family defines a valley (or ridge, if unstable) in (say) the $h - D_{\mathrm{pore}}$ plane (Fig. 2.1D). Which pore family has lowest energy, and what energy barriers oppose transitions between pores? This is crucial in the context of exocytosis, when an initially small pore must dilate for full contents release (18, 91, 92). To address this we solved the shape equation, Eq. **2.3**, constraining the pore diameter to have an arbitrary value D_{pore} (see SI Text). The radial force to maintain a pore with this diameter is $2\kappa(dH/ds)$ evaluated at the pore (122). Integrating this force over a range of D_{pore} values and using the free energies of thin catenoids calculated from Eq. **2.1** as the reference levels, we obtained the free energy landscape of Figs. 2.2A-C.

For a given membrane separation h, the free energy reaches maxima or minima at the pore diameters corresponding to the three solution families (Fig. 2.2A). Consistent with the stability analysis, the thin catenoid where predicted to be stable (unstable) lies in a valley (on a ridge). The tether solution has the opposite stability to the thin catenoid. For $h < h_c$ (typically the physiologically relevant scales for exocytosis) the wide catenoid is also stable and has the lowest energy. Separating the thin and wide catenoids is a barrier, at the peak of which lies the unstable tether. Thus, if membrane fusion creates a thin catenoid pore, a thermodynamic driving force tends to dilate the pore to the wide catenoid. However, the dilation pathway must traverse a substantial barrier whose height is determined by the unstable tether intermediate which plays the role of a transition state.

For high tensions, the tether solution oscillates in the $h - D_{\text{pore}}$ plane at small separations, with five solutions (two catenoids and three tethers) for a given separation (Fig. 2.2C). Calculating the free energy landscape as a function of D_{pore} at such a fixed h we found three valleys and two ridges as the fusion pore expands. Thus, in addition to the thin catenoid, a second metastable fusion pore is the tether with intermediate pore diameter in the middle valley.

With realistic membrane bending constraints there are three fusion pore families

Next we solved the shape equation, Eq. **2.3**, accounting properly for the bending constraints supplied by the planar membranes connected by the fusion pore. We used the appropriate zero slope BC at the boundaries, not freely hinged BCs, to account for the far field bending constraint. The exact catenoids are no longer solutions as they violate the boundary conditions, but we find there are still three fusion pore families (Figs. 2.3A, S2.4).

Again, we find there are three pore families whose properties depend on the capillary length $\lambda \equiv (\kappa/2\gamma)^{1/2}$. Scales smaller (larger) than λ are dominated by bending (membrane tension). For high membrane tensions such that the capillary length is smaller than the membrane diameter D_{mb}, the three families are close to those freely hinged BCs (Figs. 2.3A, 2.3B, S2.4). For physiologically relevant small separations, the fusion pore with the smallest width resembles the thin catenoid (we call it the thin quasi-catenoid) while the pore with the largest width resembles the wide catenoid (we call it the wide quasi-catenoid). A third unstable family with intermediate width appears. Note that switching on the bending constraint disconnects the quasi-thin catenoid and the unstable pore families.

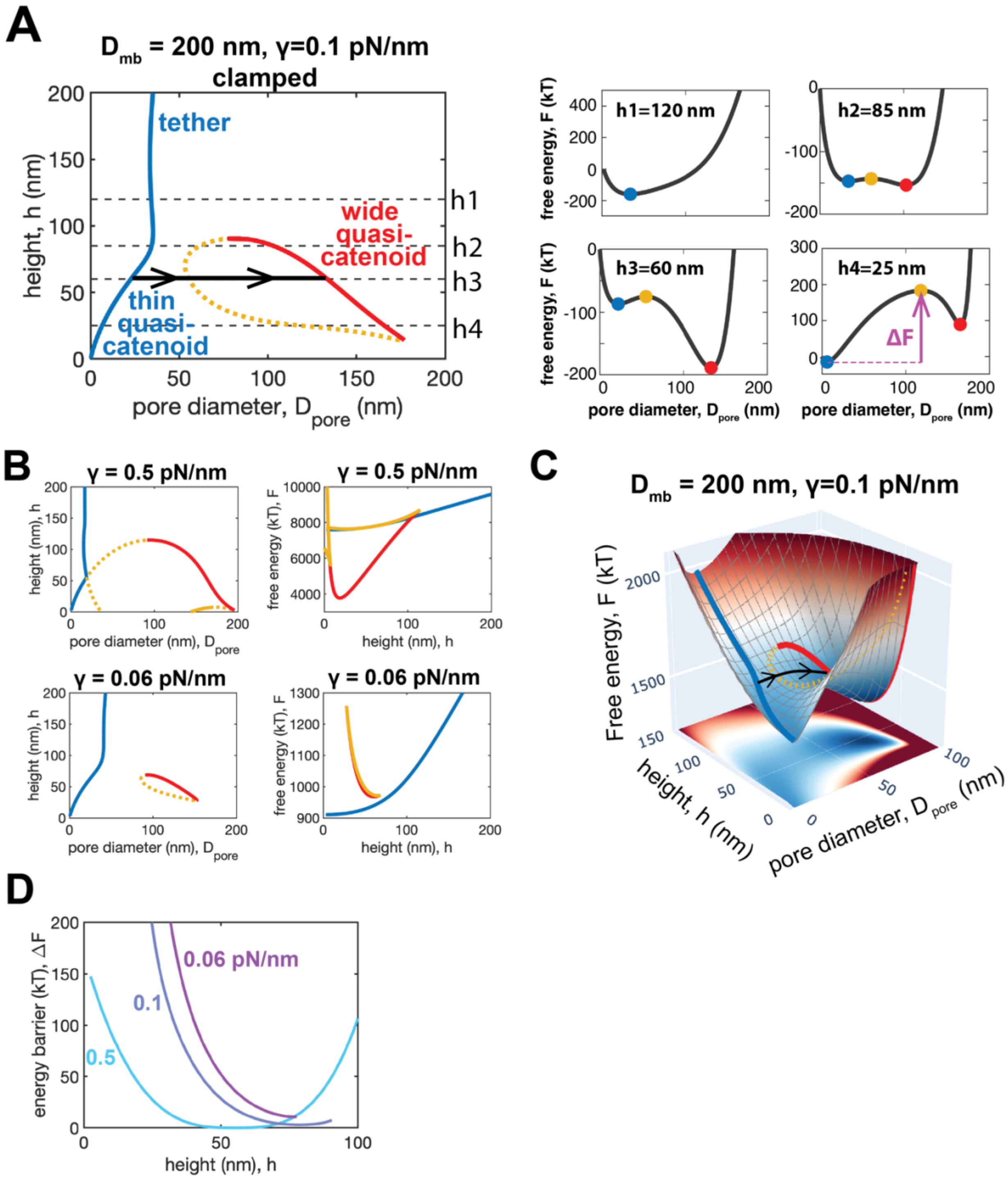

Figure 2.3. A narrow and a wide fusion pore family are stable for realistic membrane bending constraints.
Solid lines: stable. Dashed lines: unstable. (A) Stability of the three fusion pore families with realistic clamped boundary conditions. Free energy landscape for four values of h (right). Dilation from the thin to the wide catenoidal pores requires crossing an energy barrier ΔF set by the third unstable solution. (B) Three fusion pore families and their free

energies for two membrane tensions. (C) Free energy landscape. (D) Energy barrier for pore dilation vs height for three membrane tensions. An example of a dilation transition is shown (black line, $h = 60$ nm, barrier height ~10 kT). The barrier is lower at higher tensions.

Realistic membrane bending constraints: free energy landscape

To determine the stability of the three families, their relative energies and the barriers for transitions, we repeated the free energy calculations above, but with clamped BCs. We find the thin and wide quasi-catenoids are stable, while the intermediate pore is unstable and sets the barrier separating the thin and wide pores which increases for smaller membrane separations (Figs. 2.3A, 2.3C). For example, for membrane separation 60 nm and membrane tension 0.1 pN/nm, the barrier is ~10 kT. Dilation, however, is thermodynamically favored only when the membranes are sufficiently distant, when the wide catenoid energy drops below that of the thin catenoid (Fig. 2.3A).

The free energy landscape is highly sensitive to membrane tension (Fig. 2.3B). Increased tension lowers the free energy barrier ΔF for physiologically relevant small heights (Fig. 2.3D). When tension is below a certain threshold, the wide quasi-catenoid family disappears (Fig. S2.5), so that dilation of the narrow thin catenoid is no longer possible. These findings are consistent with experiments showing high membrane tension favors full-fusion exocytosis (94) and correlates with larger fusion pores (17).

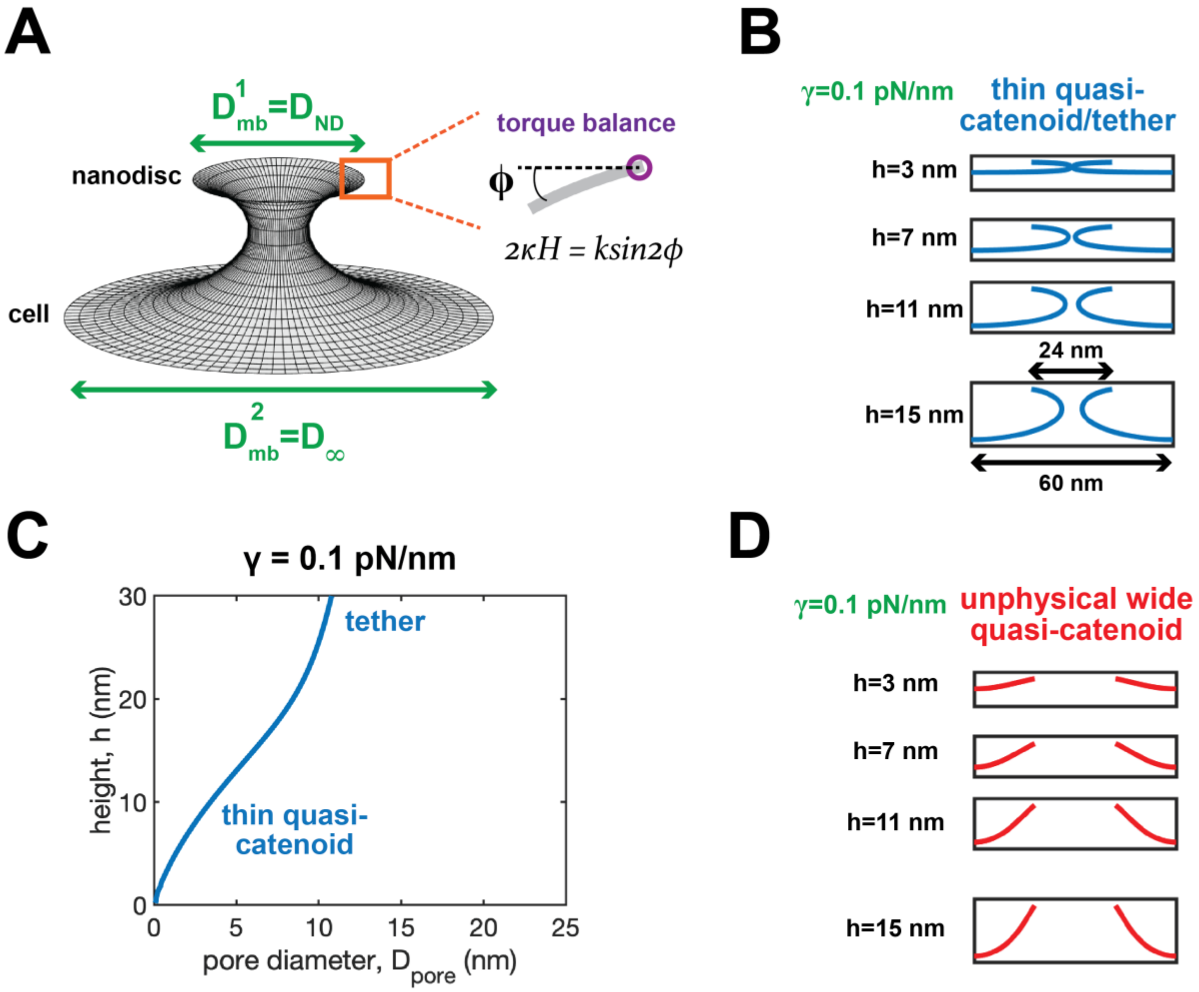
A
$D^1_{mb}=D_{ND}$
torque balance
nanodisc
φ
$2\kappa H = k\sin 2\phi$
cell
$D^2_{mb}=D_\infty$
B
γ=0.1 pN/nm
thin quasi-catenoid/tether
h=3 nm
h=7 nm
h=11 nm
24 nm
h=15 nm
60 nm
C
γ = 0.1 pN/nm
tether
thin quasi-catenoid
height, h (nm)
0
10
20
30
0
5
10
15
20
25
pore diameter, D_{pore} (nm)
D
γ=0.1 pN/nm
unphysical wide quasi-catenoid
h=3 nm
h=7 nm
h=11 nm
h=15 nm

Figure 2.4. Nanodiscs lock fusion pores into thin quasi-catenoids.
(A) Fusion pore between a nanodisc (ND) and a planar membrane. A torque balance boundary condition is imposed at the upper membrane edge, representing resistance to twisting from the ND scaffold. (B) Thin quasi-catenoid fusion pores. (C) Pore diameter vs height for the thin quasi-catenoid pore family. The thin quasi-catenoid develops into tether-like shapes for large h. (D) Unphysical wide quasi-catenoid pores. The ND scaffold is twisted by a large angle $\phi > 90°$ which may disassemble the scaffold.

Fusion pore between a nanodisc and a planar membrane

Membrane nanodiscs (NDs) are powerful systems for the study of individual pores (23, 24, 95, 123, 124). NDs are nanosized phospholipid membrane patches bounded by a lipoprotein scaffold forming a wall of two parallel alpha helices (125). By stabilizing fusion pores, NDs allow pore sizes and fluctuations to be inferred from conductance measurements. However, the mechanism of pore stabilization and the relation to pores in larger membranes of phycological relevance is not understood.

Here we used a simple elastic model (23) to determine the torque required to rotate the scaffold a certain angle and we repeated pore shape calculations with this torque-balance BC at the ND edge (Fig. 2.4A, see Appendix). This BC is intermediate between the clamped and freely hinged limits. With a typical ND diameter $D_{\mathrm{ND}} = 24$ nm and membrane tension 0.1 pN/nm, we find the ND fusion pores can only adopt thin quasi-catenoidal shapes (Figs. 2.4B, 2.4C). The wide quasi-catenoid is theoretically also accessible (Fig. 2.4D), but the membrane is forced to bend outward at the ND edge, rotating the scaffold $> 90°$. We suggest this would disassemble the scaffold and the ND. Furthermore, an energy barrier > 150 kT (set by the third unstable pore solution) impedes transition to this wide pore (Fig. S2.6). Our results also suggest the ND studies are not able to probe fusion pores under high membrane tension, as tensions as high as 2 pN/nm may activate the wide catenoidal pore since the barrier is lowered to ~10 kT (Fig. S2.6). In summary, we conclude that NDs stabilize fusion pores by banishing access to the dilated wide catenoidal pore.

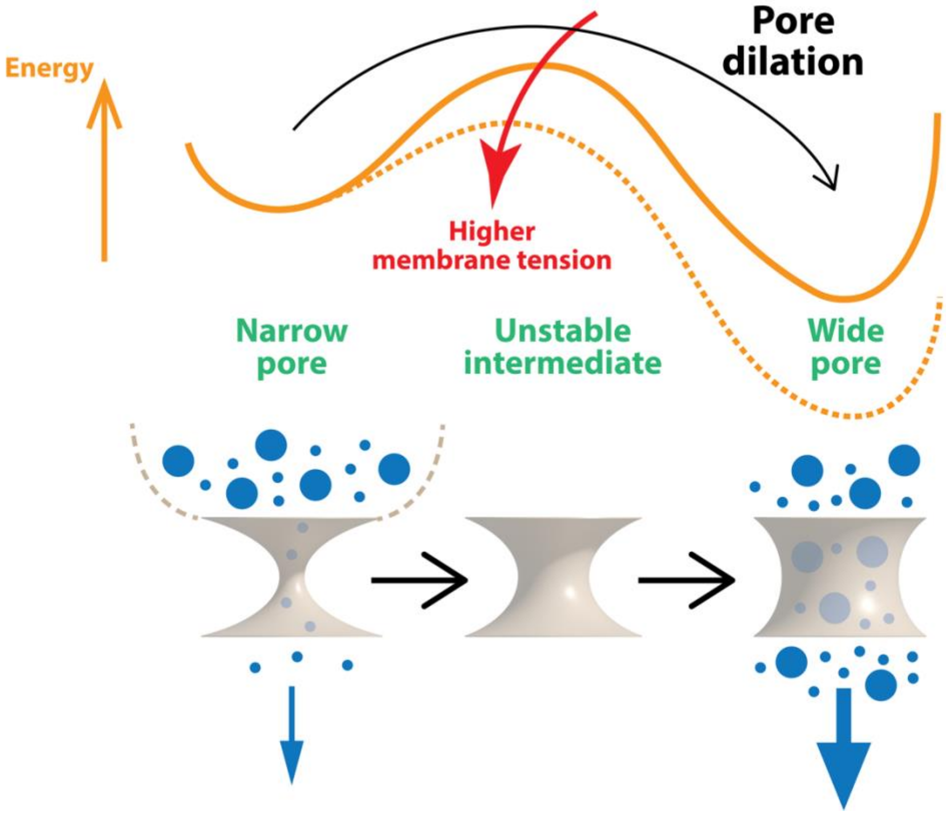

Figure 2.5. Model of the pore dilation transition during exocytosis.
Three fusion pore families define the dilation pathway. Membrane fusion generates a narrow pore permitting release of smaller molecules only. Dilation to the wide pore family requires a barrier to be surmounted, whose height is set by the unstable intermediate pore and is lowered by increased membrane tension. The wide pore permits full contents release including larger molecules.

2.3 Discussion

Membrane fusion pores are critical to many fundamental processes such as neurotransmission, hormone release, trafficking and fertilization (16). Here we identified three fusion pore families: two quasi-catenoids and a third unstable family that sets the scale of the energies (Fig. 2.3A). The thin catenoid family has the narrowest waist, and is unique to the microscopic scales of cellular membranes, being stabilized by membrane bending forces, while the wide catenoid is a fully dilated pore. These conclusions are based on properly accounting for the bending constraints provided by the membranes away from the fusion pore. For sufficiently low membrane tensions or large membrane separations, the wide catenoid fusion pore no longer exists, leaving only thin catenoids (Figs. 2.3A, 2.3B). We call the pore of intermediate size the unstable intermediate; however, for certain membrane separations this family in fact has regions of stability, corresponding to oscillations in the membrane separation-pore size plane ($h - D_{\mathrm{pore}}$ plane of Fig. 2.3B). A related oscillation was found for pulled membrane tethers (107).

In contrast to microscopic membrane surfaces, macroscopic soap films adopt only the wide catenoid, as bending forces contribute negligibly so that thin catenoids are always unstable. Indeed, using the freely hinged BCs appropriate to soap films, we showed the thin catenoid family is then stable for a band of tensions (with positive and negative upper and lower bounds) which shrinks to almost zero for macroscopic scales, while the wide catenoid is stable for any tension above a minimum value which tends to zero on macroscopic scales (Fig. 2.2D).

During exocytosis vesicle-plasma membrane fusion generates a small nascent ~1 nm fusion pore (14, 18), which must dilate if full release of the vesicle contents is to occur. Pore dilation has been characterized by amperometry recordings during dense core vesicle release, showing an initial small flickering pore (prespike foot) that suddenly dilates to a large pore (spike) (18, 91, 92, 126). The energy barrier for membrane fusion was estimated (127), but the energy landscape for pore dilation has not been clear. Here, the three families of fusion pores from our analysis suggest the initial flickering pore belongs to the stable narrow pore family, and the abrupt dilation is a transition to the stable wide pore family over a barrier whose height is set by the unstable intermediate pore family (Fig. 2.5). For example, for ~ 400 nm dense core vesicles in chromaffin cells, we estimate the barrier is ~30 kT, depending on membrane tension and separation (Fig. 2.3D). This energy landscape that the three pore families belong to is the landscape that pore size-regulating factors such as dynamin, amisyn, Syt and SNARE family proteins (13, 22-24, 95) must navigate (Fig. 2.3C). Its knowledge will help to establish the molecular mechanisms controlling pore dilation.

An important study showed that the initial small fusion pore is longer lived for larger vesicles, reflected by amperometric feet of greater duration (128). It was argued that larger vesicles have dilated pores of higher energy, explaining the increased dilation delay time. Correspondingly, we also found that the dilated (wide quasi-catenoidal) pore has higher energy for larger fusing membranes (larger D_{mb}, Fig. S2.7). However, more importantly the barrier to dilation is lower for larger membranes, the dominant effect being the large energy increase of the thin quasi-catenoid due to its large increase in area. For example, at tension $0.1\ \mathrm{pN\ nm^{-1}}$ the barrier is ~ 30 kT for 200 nm membranes and a pore height 50 nm, comparable to dense core vesicle sizes in neuroendocrine cells, decreasing to ~ 5 kT for 300 nm membranes with the same pore height ratio. We speculate this may be due to vesicle size dependence of other factors such as pore regulation by dynamin, amisyn, Synaptotagmin and SNARE family proteins (13, 22-24, 95).

For synaptic vesicles, our results suggest pore dilation is energetically challenging, given their typical ~ 50 nm diameter. Thus, full release may occur via the “omega-shrink” mode, where vesicles merge with the membrane without shape change (93). For example, at tension $0.1\ \mathrm{pN\ nm^{-1}}$ a 12 nm tall pore between 50 nm membranes cannot fully dilate as the wide pore is not a solution (Fig. S2.8). However, the dilation barrier is mechanosensitive (Fig. 2.5): higher tensions activate the wide pore, though the dilation barrier is high (e.g. ~ 70 kT at $1\ \mathrm{pN\ nm^{-1}}$, Fig. S2.9). For large dense-core vesicles of ~400 nm diameter, membrane tension has been shown to correlate with larger fusion pores and favor full-fusion over kiss-and-run (17, 94). Our analysis rationalizes these observations, as we found the barrier to pore dilation decreases with increasing membrane tension (Figs. 2.5, 2.3D). As membrane tension decreases, dilation becomes increasingly energetically demanding, until below a certain tension dilation cannot occur as the stable wide pore family ceases to exist (Fig. S2.5).

Finally, we studied fusion pores between a nanodisc and a large planar membrane (such as an extended cell plasma membrane). Nanodiscs are nanoscale membranes, powerful systems to study single fusion pores by conductance measurements (23, 24, 95, 123, 129), but it has been unclear how representative these fusion pores are of physiological pores. For typical 10-30 nm nanodiscs, we find only the narrow pore family is accessible. Theoretically, if a large energy barrier is surmounted wide pores are also accessible. However, the wide catenoid requires outward-oriented membrane at the nanodisc edge (Fig. 2.4D), a disruption imposing large twisting forces that we suggest would destabilize the nanodisc. In effect, only the small nascent fusion pore is realizable. This quantifies how nanodiscs stabilize fusion pores, by locking them into the narrow pore family and blocking dilation.

2.4 Appendix: Derivation of the model and numerical methods to solve the model

Model description

Here we present a concise derivation of the shape of catenoid, a minimal surface, and the shape equation for axisymmetric membranes, the stability analysis of catenoidal membranes with subject to classic Helfrich free energy (Eq. **2.1**, (51)) using variational principles.

Basic differential geometry

We parameterize an arbitrary surface $\underline{\boldsymbol{X}}(u^1, u^2)$ with coordinate (u^1, u^2). The two tangent vectors e_1, e_2 are

$$\boldsymbol{e}_1 \equiv \frac{\partial \underline{\boldsymbol{X}}}{\partial u^1}, \boldsymbol{e}_2 \equiv \frac{\partial \underline{\boldsymbol{X}}}{\partial u^2} \quad [S2.1.1]$$

The metric tensor, or the first fundamental form, is defined as

$$g_{ij} \equiv \boldsymbol{e}_i \cdot \boldsymbol{e}_j. \quad [S2.1.2]$$

The inverse metric g^{ij} is the inverse of the metric tensor g_{ij} such that

$$g_{ij} g^{ij} = \delta_i^k, \quad [S2.1.3]$$

where δ_i^k is the Kronecker symbol. The second fundamental form b_{ij} is given by

$$b_{ij} \equiv \boldsymbol{e}_i \cdot \boldsymbol{n}_{,j} \equiv \boldsymbol{e}_i \cdot \partial \boldsymbol{n} / \partial u^j, \quad [S2.1.4]$$

where $\boldsymbol{n}$ is the normal vector given by

$$\boldsymbol{n} \equiv \frac{\boldsymbol{e}_1 \cdot \boldsymbol{e}_2}{|\boldsymbol{e}_1 \times \boldsymbol{e}_2|}. \quad [S2.1.5]$$

The mixed second fundamental form b_i^j is defined as

$$b_i^j \equiv b_{ik} g^{kj}. \quad [S2.1.6]$$

The mean curvature H is defined as

$$H \equiv \frac{1}{2} b_i^i, \quad [S2.1.7]$$

while the Gaussian curvature G is defined as

$$K \equiv b/g, \quad [S2.1.8]$$

where g and b are the determinant of the first fundamental g_{ij} and the second fundamental b_{ij}.

Minimal surface

A minimal surface is a surface whose area is locally minimized. To derive a minimal surface we consider the area variation with subject to an infinitesimal perturbation $\underline{\boldsymbol{X}} \to \underline{\boldsymbol{X}} + \delta \underline{\boldsymbol{X}}$. The perturbation $\delta \underline{\boldsymbol{X}}$ has a normal component (in the direction of $\boldsymbol{n}$) and two tangent components (in the directions of $\boldsymbol{e}_1$ and $\boldsymbol{e}_2$),

$$\delta\underline{\boldsymbol{X}} \equiv \phi^i \boldsymbol{e}_i + \psi \boldsymbol{n}. \quad [S2.2.1]$$

The variation in the tangent vector is

$$\delta\boldsymbol{e}_i = \frac{\partial}{\partial u_i}\left(\phi^i \boldsymbol{e}_i + \psi \boldsymbol{n}\right) = \left(\nabla_i \phi^k - \psi b_i^k\right)\boldsymbol{e}_k + (\phi^k b_{ki} + \nabla_i \psi)\boldsymbol{n}, \quad [S2.2.2]$$

where ∇_i is the covariant derivative with respect to u_i. Note that $\delta\boldsymbol{e}_i$ only has the first order term. The variation of the first fundamental form g_{ij} has a first order term $\delta^{(1)} g_{ij}$ and a second order term $\delta^{(2)} g_{ij}$,

$$\delta g_{ij} = \left(\delta\boldsymbol{e}_i \cdot \boldsymbol{e}_j + \delta\boldsymbol{e}_j \cdot \boldsymbol{e}_i\right) + \delta\boldsymbol{e}_i \cdot \delta\boldsymbol{e}_j$$

$$= \nabla_i \phi_j + \nabla_j \phi_i - 2\psi b_{ij} + \mathcal{O}(2),$$

$$\equiv \delta^{(1)} g_{ij} \ + \ \delta^{(2)} g_{ij} \quad [S2.2.3]$$

where $\phi_i \equiv \phi^j g_{ji}$. The variation of the determinant g is then

$$\delta g = (g_{11} + \delta g_{11})(g_{22} + \delta g_{22}) - (g_{12} + \delta g_{12})(g_{21} + \delta g_{21}) - (g_{11} g_{22} - g_{12} g_{21}). \quad [S2.2.4]$$

Extracting the first order term $\delta^{(1)} g$ in δg, we have

$$\delta^{(1)} g = g\left(2\nabla_i \phi^i - 4H\psi\right). \quad [S2.2.5]$$

The infinitesimal area $dS = \sqrt{g}\, du_1 du_2$. The first variation in area $\delta^{(1)} A$ is

$$\delta^{(1)} A = \int \delta^{(1)} \sqrt{g}\ du_1 du_2 = \int \left(\nabla_i \phi^i - 2H\psi\right)\sqrt{g}\ du_1 du_2$$

$$= \int -2H\psi\sqrt{g}\ du_1 du_2. \quad [S2.2.6]$$

Note since the tangent terms only reparametrize the surface and do not change the area, we only keep the normal term.

A minimal surface requires $\delta^{(1)} A = 0$. Thus a minimal surface has zero mean curvature $H = 0$.

Catenoid

To derive the shape of catenoid, the axisymmetric minimal surface, we parametrize the surface by the arclength of the contour in a meridian plane s and the azimuthal angle θ, such that

$$\underline{\boldsymbol{X}}(s,\theta) = \underline{\boldsymbol{X}}\big(r(s)cos\theta, r(s)sin\theta, z(s)\big), \quad [S2.3.1]$$

where r and z is the correctional and vertical coordinate, respectively (Fig. 2.1B). The two tangent vectors are

$$\boldsymbol{e}_1 = (r'cos\theta, r'sin\theta, z'),$$

$$\boldsymbol{e}_2 = (-rsin\theta, rcos\theta, 0). \quad [S2.3.2]$$

The first fundamental g_{ij} is

$$g_{ij} = \begin{pmatrix} 1 & 0 \\ 0 & r^2 \end{pmatrix}. \quad [S2.3.3]$$

The second fundamental b_{ij} is

$$b_{ij} = \begin{pmatrix} z'r'' - z''r' & 0 \\ 0 & -rz' \end{pmatrix}. \quad [S2.3.4]$$

The mean curvature H is

$$H = \frac{1}{2}\left(\phi' + \frac{sin\phi}{r}\right). \quad [S2.3.5]$$

where ϕ is the tangent angle (Fig. 2.1B, different from the tangent variation ϕ^i) such that $tan\phi = -dz/dr$. To solve the shape of catenoids $r_{\mathrm{cat}}(z)$, we set $H = 0$ which gives

$$r_{\mathrm{cat}}(z) = \frac{D_{\mathrm{pore}}}{2}\cosh\left(\frac{2z}{D_{\mathrm{pore}}}\right). \quad [S2.3.6]$$

Shape equation

The shape of the membrane that minimizes the classic Helfrich free energy (Eq. **2.1**) has to satisfy the shape equation

$$2\kappa(\nabla^2 H + 2H^3 - 2HK) - 2\gamma H = 0, \quad [S2.4.1]$$

For an axisymmetric membrane the Laplace–Beltrami operator ∇^2 is

$$\nabla^2 \equiv \frac{1}{\sqrt{g}}\frac{\partial}{\partial u^i}\left(\sqrt{g}g^{ij}\frac{\partial}{\partial u^j}\right) = \frac{1}{r}\frac{\partial}{\partial s}\left(r\cdot 1\cdot\frac{\partial}{\partial s}\right) + \frac{1}{r}\frac{\partial}{\partial\theta}\left(r\cdot\frac{1}{r^2}\cdot\frac{\partial}{\partial\theta}\right) = \frac{\partial^2}{\partial s^2} + \frac{r'}{r}\frac{\partial}{\partial s}, \quad [S2.4.2]$$

Note that $\partial/\partial\theta = 0$ for axisymmetric membranes. Also the Gaussian curvature K is

$$K = \frac{sin\phi}{r}\phi'. \quad [S2.4.3]$$

By plugging Eq. S2.3.4, Eq. S2.4.3 into Eq. S2.4.2 we derive the shape equation for axisymmetric membranes (Eq. **2.3**). Note that $r' = cos\phi$.

Catenoid stability

To analytically derive the stability of the catenoidal membranes, we consider the second variation. For soap films with no bending energy, we consider the second variation in the area, $\delta^{(2)}A$. For a membrane of an arbitrary shape,

$$\delta^{(2)}A = \frac{1}{2}\int \psi(-\nabla^2 + 2K)\psi\, dS \equiv \frac{1}{2}\int \psi L\psi\, dS. \quad [S2.5.1]$$

The derivation is similar to that of the first variation $\delta^{(1)}A$, but the variations in the metric tensor elements g_{ij} have to be expanded to second order. A detailed derivation can be found in ref. (119).

We parameterize the catenoidal surface S_{cat} with two parameters, azimuthal angle u and normalized height v, such that

$$\boldsymbol{S_{cat}}(u,v) = (c\cosh v\cdot\cos u\,, c\cosh v\cdot\sin u\,, cv), \quad [S2.5.2]$$

where c is half of the pore diameter D_{pore} (Fig. 2.1A).

The two tangent vectors are

$$\boldsymbol{e}_1 \equiv \frac{\partial\boldsymbol{S_{cat}}}{\partial u} = (-\,c\cosh v\cdot\sin u\,, c\cosh v\cdot\cos u\,, 0)$$

$$\boldsymbol{e}_2 \equiv \frac{\partial \underline{\boldsymbol{X}}}{\partial u^2} = (c \sinh v \cdot \cos u\, , c \sinh v \cdot \sin u\, , c), \quad [S2.5.3]$$

The metric tensor g_{ij} is

$$g_{ij} = \begin{pmatrix} c^2 \cosh^2 v & 0 \\ 0 & c^2 \cosh^2 v \end{pmatrix}. \quad [S2.5.4]$$

The determinant g is

$$g = c^2 \cosh^2 v. \quad [S2.5.5]$$

The Laplace–Beltrami operator ∇^2 is

$$\nabla^2 = \frac{1}{c^2 \cosh^2 v}\left(\frac{\partial}{\partial u^2} + \frac{\partial}{\partial v^2}\right). \quad [S2.5.6]$$

The Gaussian curvature K is

$$K = \frac{1}{c^2 \cosh^4 v}. \quad [S2.5.7]$$

Thus keeping only the axisymmetric term $\partial/\partial v^2$ the operator $L \equiv -\nabla^2 + 2K$ is

$$L = \frac{1}{c^2 \cosh^2 v}\left(\frac{\partial}{\partial v^2} + \frac{2}{\cosh^2 v}\right). \quad [S2.5.8]$$

The eigenvalue problem $L\psi = \lambda\psi/c^2$ leads to a Sturm-Liouville problem

$$\psi'' + \frac{2}{\cosh^2 v}\psi + \lambda \cosh^2 v\, \psi = 0. \quad [S2.5.9]$$

whose eigenfunctions and eigenvalues are ψ_i and λ_i. For a perturbation $\psi = \sum_{1=1}^{\infty} c_i \psi_i$Thus, in terms of ψ_i and λ_i the second variation in area is

$$\delta^{(2)}A = \frac{1}{2}\int \psi L\psi\, dS$$

$$= \frac{1}{2}\int_{-h/2c}^{h/2c}\int_{0}^{2\pi}\sum_{i=1}^{\infty} c_i\psi_i \cdot \sum_{i=1}^{\infty}\frac{c_i\lambda_i}{c^2}\psi_i \sqrt{g}\, dudv$$

$$= \frac{1}{2}\int_{-h/2c}^{h/2c} 2\pi c^2 \cosh^2 v \sum_{i=1}^{\infty} c_i\psi_i \cdot \sum_{i=1}^{\infty}\frac{c_i\lambda_i}{c^2}\psi_i\, dv$$

$$= \frac{1}{2}\int_{-h/2c}^{h/2c} 2\pi \cosh^2 v \sum_{i=1}^{\infty} c_i^2\lambda_i\psi_i^2\, dv = \pi\sum_{i=1}^{\infty} c_i^2\lambda_i, \quad [S2.5.10]$$

where h is the height of the catenoid. The properties of Sturm-Liouville eigenfunctions are used

$$\int_{-h/2c}^{h/2c} \cosh^2 v\, \psi_i\psi_j\, dv = \begin{cases} 1, if\ i = j \\ 0, if\ i \neq j \end{cases}. \quad [S2.5.11]$$

With the inclusion of bending energy, the second variation in Helfrich free energy (Eq. **2.1**) is

$$\delta^{(2)}F = \frac{\kappa}{2}\int \psi[(\nabla^2)^2 + 4Hb^{ij}\nabla_i\nabla_j + (2H^2 - 4K)\nabla^2 + 2b^{ij}\nabla_i\nabla_j H - 2H\nabla^2 H + 2(\nabla^i H)(\nabla_i H)$$

$$+ 4K^2 + 16H^4 - 20H^2K - 4G_{ij}b^{ij}H]\psi\, dS$$

$$+ \frac{\gamma}{2}\int \psi(-\nabla^2 + 2K)\psi\, dS, \quad [S2.5.12]$$

where b^{ij} is the inverse of the second fundamental form b_{ij}, $\nabla^i \equiv g^{ij}\nabla_j$, G_{ij} is the Einstein tensor and the integral is over the reference surface. A detailed derivation can be found in ref. (119)

For a catenoid whose mean curvature is zero, Eq. S2.5.9 can be greatly simplified to

$$\delta^{(2)}F = \int \frac{\kappa}{2}\psi L^2\psi + \frac{\gamma}{2}\psi L\psi\, dS, \quad [S2.5.13]$$

The variation in the bending term $\delta^{(2)}F_{\text{bend}}$ is

$$\delta^{(2)}F_{\text{bend}} \equiv \int \frac{\kappa}{2}\psi L^2 \psi \, dS$$

$$= \frac{\kappa}{2}\int_{-\frac{h}{2c}}^{\frac{h}{2c}} \int_0^{2\pi} \sum_{i=1}^{\infty} c_i \psi_i \cdot L\left(\sum_{i=1}^{\infty} \frac{c_i \lambda_i}{c^2}\psi_i\right)\sqrt{g}\, dudv$$

$$= \pi\kappa \int_{-\frac{h}{2c}}^{\frac{h}{2c}} \sum_{i=1}^{\infty} c_i \psi_i \;\; c^2 \cosh^2 v \cdot \sum_{i=1}^{\infty} \frac{c_i \lambda_i^2}{c^4}\psi_i \, dv = \frac{\pi\kappa}{c^2}\int_{-\frac{h}{2c}}^{\frac{h}{2c}} \cosh^2 v \sum_{i=1}^{\infty} c_i^2 \lambda_i^2 \psi_i^2 \, dv$$

$$= \frac{\pi\kappa}{c^2}\sum_{i=1}^{\infty} c_i^2 \lambda_i^2, \quad [S2.5.14]$$

Thus the second variation of the free energy is

$$\delta^{(2)}F = \frac{\pi\kappa}{c^2}\sum_{i=1}^{\infty} c_i^2 \lambda_i^2 + \pi\gamma \sum_{i=1}^{\infty} c_i^2 \lambda_i = \sum_{i=1}^{\infty} \lambda_i \left(\frac{c^2\gamma}{\kappa} + \lambda_i\right)\frac{\pi\kappa}{c^2} c_i^2, \quad [S2.5.15]$$

Radial force on the pore

To calculate the free energy landscape of fusion pores with an arbitrary diameter D_{pore}, we need to calculate the radial force acting on the pore to maintain D_{pore}. Because the two membranes have the same size, $D_{mb}^1 = D_{mb}^2$ (Fig. 2.1A), the minimal cross-sectional diameter will always appear in the middle, $z = 0$. Thus, we solve the same shape equation Eq. **2.3** but only solve the shape of half of the pore ($-h/2 < z < 0$) where the imposed pore diameter comes into the boundary condition at $z = 0$. To calculate the radial force acting on $z = 0$ we use the stress tensor (a derivation see ref. (130))

$$\boldsymbol{f^i} = \left[2\kappa H\left(b^{ij} - Hg^{ij}\right) - \gamma g^{ij}\right]\boldsymbol{e}_j - 2\kappa\left(\nabla^i H\right)\boldsymbol{n}, \quad [S2.6.1]$$

where $\boldsymbol{f^i}$ is a 3×2 tensor.

The force per unit length exerted on the boundary $z = 0$ is

$$F_{\boldsymbol{ext}} = l_i \boldsymbol{f}^i, \quad [S2.6.2]$$

where l_i $(i = 1,2)$ are constants such that $l_i\boldsymbol{e_i}$ is the normal vector that lies in the tangent plane and is perpendicular to the boundary. Here $l_i\boldsymbol{e_i}$ is the unit vector pointing in the z direction (Fig. 2.1B). Using the axisymmetric parameterization $\underline{\boldsymbol{X}}(s,\theta)$ (Eq. S2.3.1), the two normal vectors at the boundary $z = 0$ where $\phi = \pi/2$ are

$$\boldsymbol{e}_1 = (\cos\phi\, cos\theta, \cos\phi\, sin\theta, sin\phi) = (0,0,1),$$

$$\boldsymbol{e}_2 = (-rsin\theta, rcos\theta, 0). \quad [S2.6.3]$$

Thus $l_1 = 1$ and $l_2 = 0$. $F_{\boldsymbol{ext}}$ is then

$$\boldsymbol{F_{ext}} = f^1 = \left[2\kappa H\left(b^{1j} - Hg^{1j}\right) - \gamma g^{1j}\right]\boldsymbol{e}_j - 2\kappa(\nabla^1 H)\boldsymbol{n}. \quad [S2.6.4]$$

Since we are interested in the radial force we only extract the normal component,

$$\boldsymbol{F_{ext}} = 2\kappa \left.\frac{dH}{ds}\right|_{z=0}. \quad [S2.6.5]$$

The free energy change ΔF from a pore diameter D_{pore}^1 to anther diameter D_{pore}^2 is

$$\Delta F = \int_{D_{pore}^1}^{D_{pore}^2} 2\pi D_{pore} F_{ext}\, dD_{pore}, \quad [S2.6.6]$$

where the factor of 2 comes from the fact that both the upper $(0 < z < h/2)$ and the lower membrane $(-h/2 < z < 0)$ are exerting forces on the boundary.

Torque balance boundary condition

To more realistically model the nanodisc (ND) fusion pores, we further used a torque-balance boundary condition where the fusion pore meets the ND scaffold (Fig. 2.4A). Our torque-balance condition relies on a simple elastic model of the ND scaffold originally developed in ref. (23). Because of the two-alpha helix structure of the ND scaffold, it is more difficult to bend the scaffold in one material direction than another. Approximating the cross section of the scaffold as a rectangle with dimensions $w \times 2w$, where $w = 1.2$ nm is the diameter of a typical alpha helix, it is much harder to bend the scaffold across its wider face (in the transverse direction) than across the thinner face (in the lateral direction).

The elastic energy of the scaffold is given by

$$F_{\text{scaffold}} = \pi D_{\text{ND}} \left\{ \frac{K_{\text{soft}}}{2} C_{\text{soft}}^2 + \frac{K_{\text{hard}}}{2} C_{\text{hard}}^2 \right\} \quad [S2.7.1]$$

where D_{ND} is the ND diameter, K_{soft} and K_{hard} are the respective moduli for lateral and transverse bending modes of the scaffold, and C_{soft} and C_{hard} are the respective material curvatures of the scaffold in the lateral and transverse directions. Classical elasticity theory shows that, for a rod with a $w \times 2w$ rectangular cross section, the bending moduli are given by

$$K_{\text{soft}} = 2\,K$$

$$K_{\text{hard}} = 8\,K, \quad [S2.7.2]$$

where K is the bending modulus of a $w \times w$ rod. The bending modulus of a typical single alpha helix is $K \approx 100\ kT \cdot \text{nm}$; thus the ND scaffold has bending moduli $K_{\text{soft}} = 200\ kT \cdot \text{nm}$, $K_{\text{hard}} = 800\ kT \cdot \text{nm}$. We find that torque balance between the membrane and the ND scaffold is achieved when

$$2\kappa H = \frac{K_{\text{hard}} - K_{\text{soft}}}{2(D_{\text{ND}}/2)^2} \sin 2\phi \equiv k \sin 2\phi, \quad [S2.7.3]$$

where ϕ is the angle by which the cross section of the ND scaffold has been rotated, and k is the twisting stiffness of the ND (see SI). A non-elastic soft scaffold ($K_{\text{hard}} = K_{\text{soft}}$) will lead to freely hinged boundary condition ($H = 0$) while a stiff scaffold ($K_{\text{hard}} \gg K_{\text{soft}}$) will give a clamped zero-slope boundary condition.

To model the fusion pore of a membrane ND fusing with a cell membrane, we solved the shape equation Eq. **2.2**, applying the torque balance condition, Eq. S2.7.3, at the ND edge, $z = h/2$, and clamped boundary conditions where the fusion pore meets the cell membrane, $z =$

$-h/2$. The ND scaffold is assumed to have a diameter of 24 nm, while the diameter of the boundary meeting the cell, D_∞, is chosen to be a much larger value, 60 nm (23) (Fig. 2.4A).

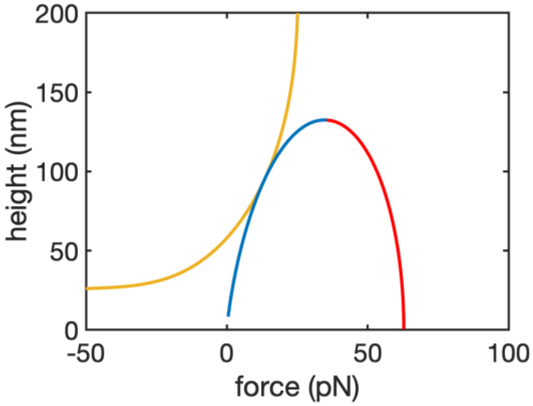

Figure S2.1. Force vs height for the fusion pore families with freely hinged boundary conditions.
Membrane tension is 0.1 pN/nm and the membrane diameter D_{mb} is 200 nm. Catenoids (red and blue) require a pulling (positive) force to maintain the height, while for tethers of small heights compressive forces are required.

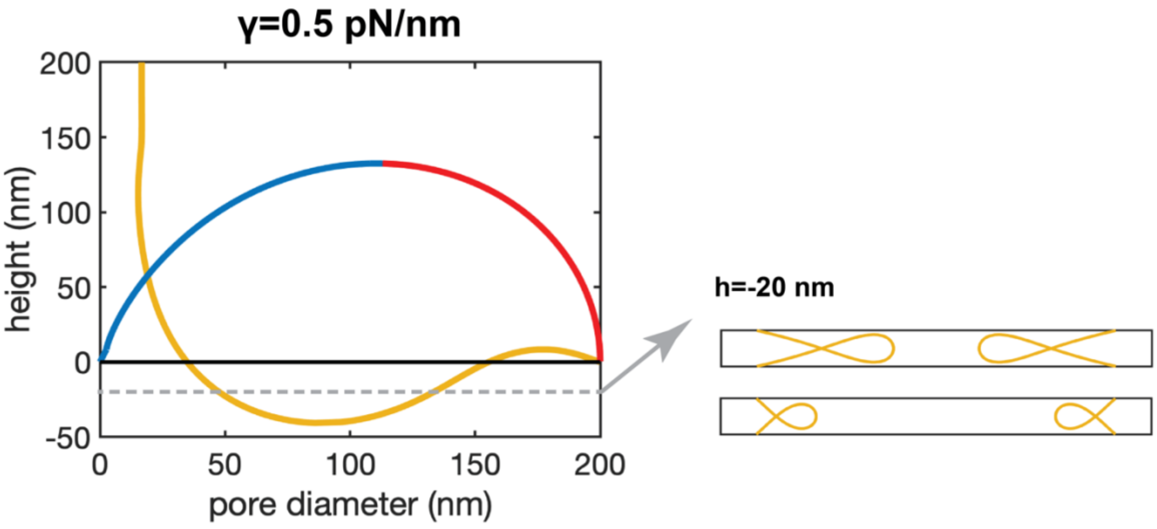

Figure S2.2. Large tether oscillations under a higher membrane tension.
Under freely hinged boundary conditions, the tether family oscillates to negative separations. However, these solutions are not physical.

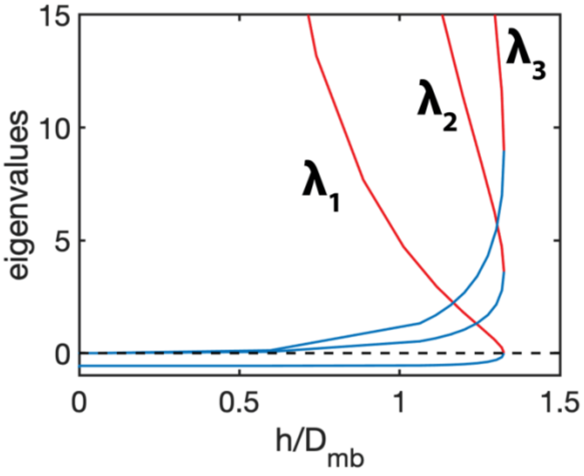

Figure S2.3. The smallest three Eigenvalues of Equation 2.8.
For thin catenoids (blue), the first (smallest) eigenvalue λ_1 is negative but other eigenvalues λ_2, λ_3, … are always positive. For wide catenoids (red), all the eigenvalues are positive.

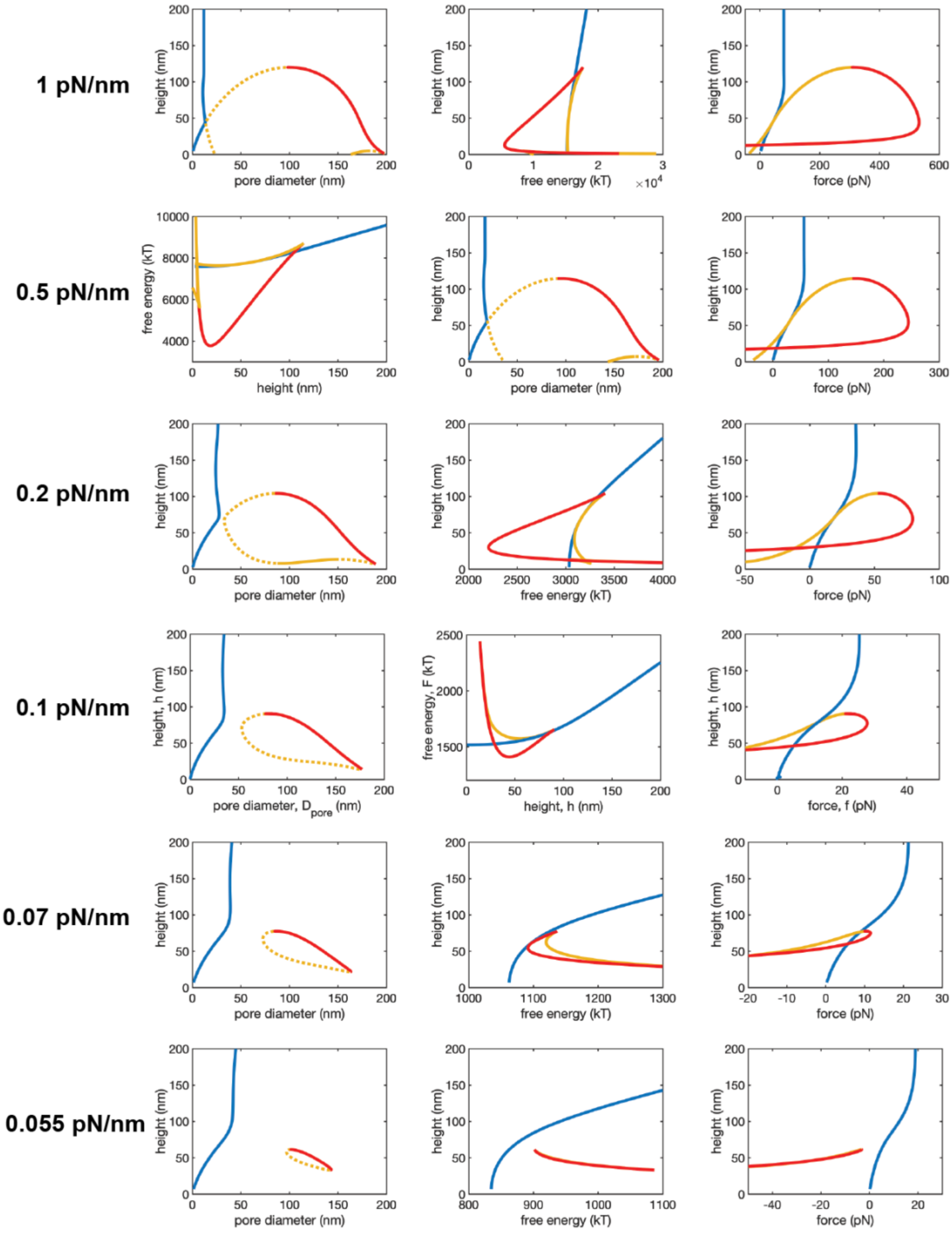

Figure S2.4. Pore diameter, free energy and force of the three fusion pore families vs pore height under clamped boundary conditions.

Membrane diameter is 200 nm. With decreased membrane tension, the wide quasi-catenoids (blue) only exist in a smaller range of heights, and below a certain tension, the thin quasi-catenoids (red) starts to have the lowest energy.

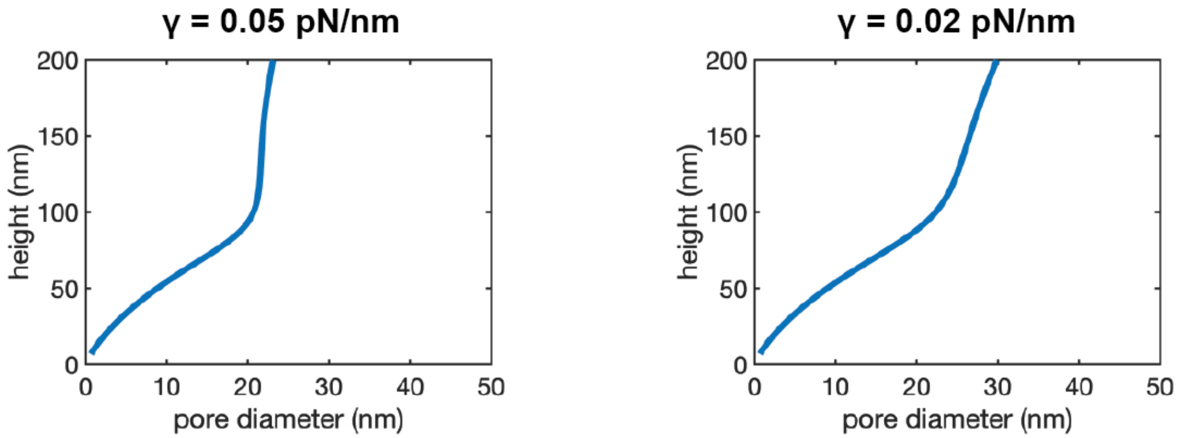

Figure S2.5. Thin quasi-catenoid is the only realizable pore under low membrane tension and clamped boundary conditions.
With membrane diameter is 200 nm, only the thin catenoid pores are found, consistent with Fig. S4 where the other two families, wide catenoid and the unstable intermediate, exist in a smaller and smaller height range with decreased tension.

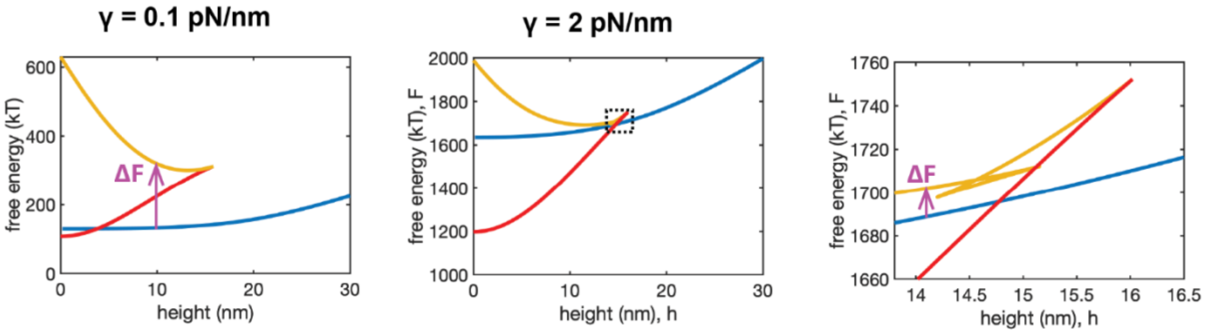

Figure S2.6. Nanodiscs lock the fusion pore into the thin quasi-catenoid family but high tension may activate pore dilation.
Under normal tension (left), the transition from the thin catenoidal pore (blue) to the unphysical wide catenoidal pore (red) is blocked by a high energy barrier Δ*F* of ~150 kT. However, under high tension (middle), the barrier decreases to ~10 kT (right, zoom-in of the dotted box in the middle panel) which makes the unphysical wide catenoidal pore realizable.

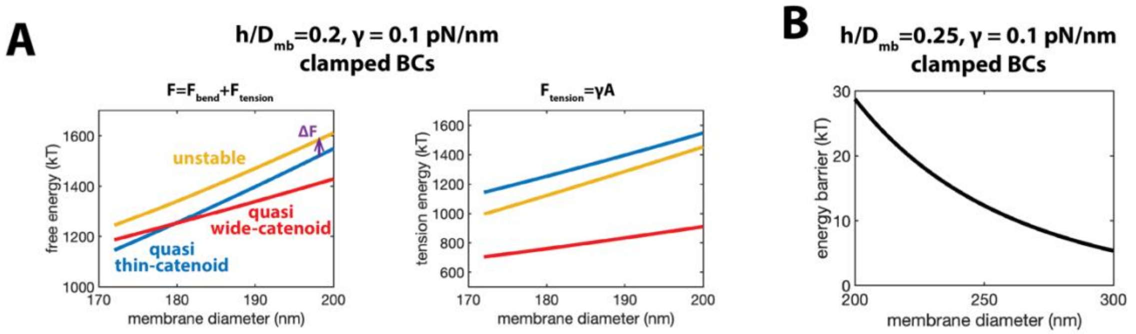

Figure S2.7. Pore dilation is favored by larger vesicles.

(A) The free energies of the three families of fusion pore all increase with increased membrane diameter, but at different rate. The energy of the thin quasi-catenoid increases the most, mainly attributed to the large area increase (right). The energy of the unstable intermediate only increases moderately, thus the energy barrier for pore dilation ΔF is smaller with increased vesicle size. (B) Energy barrier of pore dilation decreases with membrane diameter.

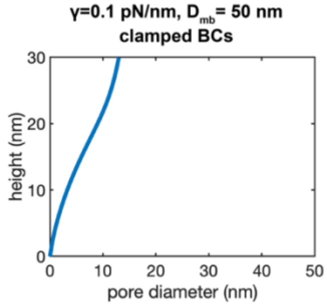

Figure S2.8. Only the thin quasi-catenoid fusion pore exists for small membrane diameter and normal tension.

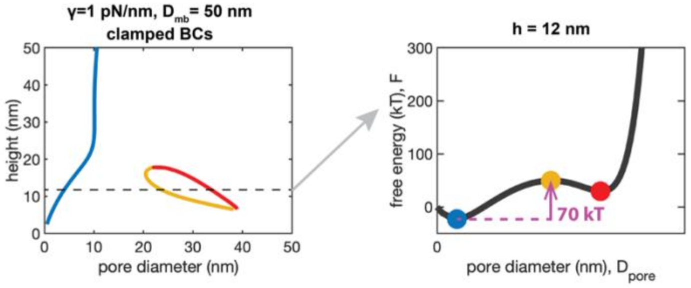

Figure S2.9. High membrane tension activates the wide pore.

For a membrane diameter comparable to synaptic vesicle diameters, $D_{mb} = 50$ nm, the wide pore (red) becomes a solution at high tensions. At tension 1 $\mathrm{pN} \cdot \mathrm{nm}^{-1}$ the energy

barrier for the transition from the small pore (blue) to the wide pore has height 70 kT for membrane separation h=12 nm.

Chapter 3: Spatiotemporal regulation of exocytosis by a membrane reservoir via release site availability

In this chapter, I describe computational work on understanding spatiotemporal regulation of exocytosis in chromaffin cells. The experiments I analyzed here were done by the Ling-gang Wu group at National Institute of Health. Dong An, a Ph.D. student in the O'Shaughnessy group, also contributed to this work.

3.1 Introduction

Exocytosis involves a vesicle enclosing bioactive molecules such as hormones and neurotransmitters to fuse with the plasma membrane (PM) of excitable cells, leading to release of content molecules to the extracellular environment and delivery of proteins and lipids to the PM (8, 14, 16, 131). Exocytosis is spatially regulated by cells. The location of vesicle release is carefully controlled. In neurons synaptic vesicles are released at the active zone (AZ), a highly specialized region of ~0.2 μm (132) consisting of a dense protein network tightly attached to the presynaptic terminal membrane (133). The AZ is precisely aligned with receptors on the postsynaptic density, allowing ultrafast information passage at the synapse by minimizing the diffusion distance of the neurotransmitters (25). In endocrine cells, however, the existence of such AZ is not obvious from microscopy studies (26). Instead, for example, in insulin secreting cells, vesicle fusion can happen repeatedly at hotspots (27-29). Lacking such hotspots might be the cause of impaired insulin secretion in type 2 diabetes (28).

Exocytosis is also temporally regulated, reflected as highly modulated exocytosis rates upon different stimulus protocols in different cells (30). The exocytosis rate is an overall measurement taking all steps of vesicle release into consideration, including delivering the vesicles to the PM, docking the vesicles to sites of release, catalyzing vesicle membrane fusion upon stimulus, recycling vesicles and refilling the vesicles with signaling molecules (134). These steps are regulated by cellular machineries on different time and length scales, and which step is the rate-limiting one is stimulation and cell dependent. (135). For example, repeated stimulation in neurons lowers the exocytosis rates, known as short-term depression (31-34). The traditional view attributes depression to failure in replenishing the readily releasable pool (RRP), a subgroup of docked and primed synaptic vesicles that fuse rapidly upon an action potential (34). In secretory cells such as chromaffin cells, disruption of the actin cortex results in an overall increase but initial decrease in exocytosis rates, revealing a dual role of the cortex (136). Being a barrier, the actin cortex has to disassemble for a vesicle to approach the PM (35), while being a carrier, the associated proteins in the cortex such as myosin II navigate the vesicle to the docking sites (36). Finally, vesicle release probability determines the number of docked vesicles that release their contents per stimulus, providing another layer of exocytosis rate regulation (137, 138). This release probability is determined by the membrane fusion rate set by the conserved fusion machinery across eukaryotes. Among the fusion machinery, SNARE and Synaptotagmins are the core proteins and they work cooperatively in a calcium-dependent manner to surmount the large energy barrier of vesicle fusing with the PM (96, 139, 140).

Temporal regulation of exocytosis may also be regulated via the availability of release sites. Availability of locations where vesicles can dock and then fuse may be the bottleneck for sustained synaptic vesicle release (39). This proposal contradicts the widely accepted hypothesis that the available vesicles in the RRP is the bottleneck (34). Evidence supporting a fixed number of release sites dates back to statistics of the postsynaptic currents, which is triggered by release of neurotransmitters from the postsynaptic vesicles. The fluctuations of the postsynaptic current become very small at high stimulus frequency (37). This suggests the number of release sites is fixed and almost all vesicles dock to the release sites will release, as either a varying release site number or a moderate release probability will greatly enhance the fluctuations in the postsynaptic response (39). Consistently, a small fluctuation in the number of release sites (~10 ± 1 sites per hippocampal bouton) was observed from a recent microscopy study (141). However, not all the sites are available all the time. After a vesicle release its content, the site experiences a refractory period during which the next vesicle is not able to dock (38). It is proposed that to make the site reusable again the vesicular component of the previous exocytosis event has to be cleared either by passive diffusion of the component or by active removal of the local membrane (39).

The need for clearance of release sites leads to an underestimated role of endocytosis. Under mild stimulation which does not deplete the RRP, inhibiting endocytosis in hippocampal neurons caused accumulation of exocytosed vesicular component and release depression (142). This provides strong evidence that release site availability regulates exocytosis rate and endocytosis serves to clear release sites. Cells use different forms of endocytosis to clear protein and recycle membrane on different time scale. For example in neurons, clathrin-mediated endocytosis takes 30 s (143), kiss-and-run (whose existence is still under debate) takes 1-2 s (15). Recently ‘flash-and-freeze’ electron microscopy revealed another form of endocytosis, ultrafast endocytosis, occurring within 100 ms at sites flanking the active zone (144). Given an estimation of refractory time of < 200 ms during high-frequency stimulation (39), ultrafast endocytosis may play a key role in this scenario to clear the release sites and make them usable again.

However, the mechanism by which site availability is regulated is not fully understood. Hotspots were visualized in multiple cell types, but how this repeated usage of release sites regulates exocytosis rate is not clear. Recent breakthrough using super resolution microscopy revealed a variety of exocytosis and endocytosis evolution in chromaffin cells at single vesicle level (13, 93, 145). Vesicles can shrink into the PM driven by osmotic pressure and PM tension (93), but a significant number of vesicles either stay at the release site maintaining their original size, or even grow in size. The mechanism by which these unmerged vesicles occupy the release sites is not known. A unified picture of spatiotemporal exocytosis regulation via these different vesicle evolutions is also missing.

Here we used confocal microscopy to measure the spatiotemporal distribution of dense-core vesicle exocytosis events in chromaffin cells. By analyzing the spatiotemporal profile, we found a novel mechanism of spatiotemporal exocytosis regulation via release site availability. We found a membrane reservoir consisting of unmerged and slowly merged vesicles emerges from repeated exocytosis at hotspots. In turn, the release sites occupied by unmerged vesicles in the reservoir locally suppress exocytosis event frequency. We use mathematical modeling to reveal such spatiotemporal regulation is via membrane tension. PM tension has to drop below a threshold otherwise the membrane reservoir would not form as the driving force for vesicle merging from osmotic pressure still exists. Repeated exocytosis is likely to lower the plasma membrane tension locally by providing excessive lipids. The vesicles in the reservoir may further be cut away from the PM and recycled. This shortcut to endocytosis will make the sites reusable and might be important for sustained release.

3.2 Results

Imaging exocytosis events

We used inverted confocal microscopy to image individual exocytosis events in live, primary-cultured bovine adrenal chromaffin cells (17). Exocytosis of ~400-nm diameter dense-core vesicles was triggered by whole-cell dialysis of 1.5 μM Ca^{2+}, in which a pipette solution of Ca^{2+} and EGTA was injected into the cell to maintain an intracellular concentration of 1.5 μM. Two fluorescent dyes were added to the bath solution culturing the chromaffin cells: A647 (red) and A488 (green). To image exocytosis events in which vesicles fused with the lower planar plasma membrane (PM) in contact with the coverslip, the focal plane included this part of the PM and a region extending ~ 350 nm into the cell (Fig. 3.1A). The lateral resolution was ~230 nm, and the imaging area comprised 400×255 pixels with a pixel size of 46.5, 56.42, or 58.85 nm, for a total area of ~220, ~325, or ~353 μm^2, respectively.

Before exocytosis is triggered, a dark region with baseline fluorescence intensity indicates the region where the PM contacts the coverslip (Fig. 3.1A). Confocal images were collected every 18.5 or 40.5 ms, beginning immediately following calcium dialysis (time $t = 0$). Each movie lasts either 60 or 90 s. Calcium dialysis caused dense-core vesicles to fuse with the PM. When a fusion event occurred, solution containing the dyes flowed into the fused vesicles and a bright spot was suddenly apparent (Fig. 3.1B). These spots are typically circular with ~500 nm diameter, comparable to the dense-core vesicle diameter. At the onset of imaging ($t = 0$), some pre-existing spots are present whose sizes are similar to the vesicle size (Fig. 3.1B).

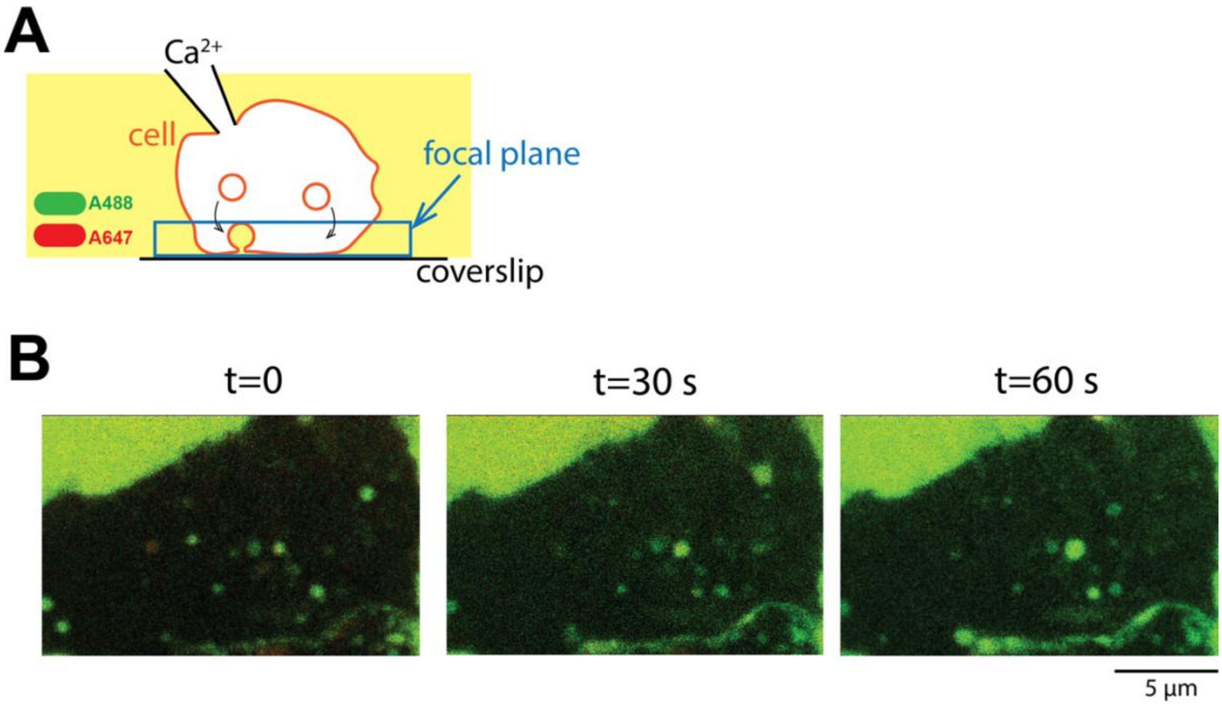

Figure 3.1. Confocal imaging of cultured chromaffin cells following whole-cell calcium dialysis.
(A) Schematic of a chromaffin cell dialyzed by Ca^{2+}. The lower plasma membrane and a region ~ 350 nm deep into the cell is imaged. (B) Images at the indicated times following Ca^{2+} dialysis.

Analysis of the exocytosis events

For $n = 26$ movies of 60 or 90 seconds each from nine cells total, we measured 678 exocytosis events in total, with 5-70 exocytosis events in each movie. An exocytosis event is manifested by the sudden appearance of a bright circular spot. For each such event, we measured the fluorescence intensities of the two dies in the spot region as function of time. The A488 dye (green) is excited weakly, so its intensity is almost unchanged over the course of the entire movie and can be used to measure the evolving size of the fused vesicle. Since the A647 dye (red) is strongly excited, if the fusion pore closes the dye within the vesicle is rapidly bleached and the intensity decays to background, whereas an open pore allows turnover of the dye within the vesicle so the intensity is maintained. Thus, an open pore is indicated by non-decaying red and green signals, while for a closed pore the green signal is maintained but the red signal decays to background.

To analyze the spatiotemporal profile of the exocytosis events, for each event we recorded its position in the confocal plane (the planar surface where the cell membrane meets the coverslip) and the time when the spot appeared. We define the location of an exocytosis event $\boldsymbol{r_i} \equiv (x_i, y_i)$ as the coordinate of the brightest pixel in the ~ 500 nm spot, and we define its time of appearance t_i as the frame when both A647 and A488 intensities increased to > 2-fold the baseline level. This two-fold increase typically occurs over ~200 ms (5 or 11 frames). From the measured locations and times of many exocytosis events, we calculated $P_{\mathrm{cum}}(R, T)$, the spatiotemporal cumulative distribution function (cdf) for the pairwise separation $\Delta r_{ij} \equiv |\boldsymbol{r}_i - \boldsymbol{r_j}|$ and time interval $t_{ij} \equiv |t_i - t_j|$ between two exocytosis events i, j in the same movie. $P_{\mathrm{cum}}(R, T)$ is defined as the fraction of pairs of exocytosis events which occurred within a distance R of one another ($\Delta r_{ij} \leq R$) and within a time T of one another ($\left|t_i - t_j\right| \leq T$), averaged over all movies.

We estimated the evolving surface area of a fused vesicle, the area of membrane enclosing the vesicle. For an exocytosis spot, at each time t we measured the total green A488 intensity relative to background intensity integrated over a circular region just covering the spot, which we took to be proportional to the total vesicle volume. To convert from total intensity to volume, we measured the peak intensities relative to background for 50 (subsequently shrinking) spots and assumed this average represents the volume of a vesicle having the mean diameter, 300 nm, measured from electron microscopy (2). Given the volume of a vesicle inferred in this way, we estimated its area by making the approximation that the vesicle is spherical.

Four fundamental classes of exocytosis event

Among the total of 678 measured exocytosis events, we found four fundamental classes (Figs. 3.2A-D) (12, 13). (i) Shrink events (77.8 ± 2.7% of all events, mean ± s.e.m). Following appearance of a spot, the green A647 spot intensity decreases to baseline, indicating a continuous merging of the vesicle into the membrane. (ii) Stay events (12.8 ± 2.4%). The vesicle size does not change, from the instant of fusion to the end of the movie (constant A647 intensity). (iii) Grow events (3.3 ± 1.0%). The vesicle grows, continuing to grow until the end of the movie (increasing A647 intensity). (iv) Close events (0.6 ± 0.5%). The fusion pore closes immediately (constant green A647 intensity, decay of red A488 intensity to background.)

While ~ 95% of exocytosis events belonged to these four fundamental categories, the remaining ~5% were composite events, in which a vesicle first underwent one type of evolution and then switched to another class (Fig. 3.2D). Composite events were either (i) grow-shrink (1.8 ± 0.7%), (ii) stay-shrink (0.8 ± 0.4%), or (iii) shrink-stay (2.9 ± 0.7%).

In addition to the above, several fluorescent spots were present at the beginning of each movie, presumably indicating vesicles already fused with the membrane. Over time these shrank, stayed or grew.

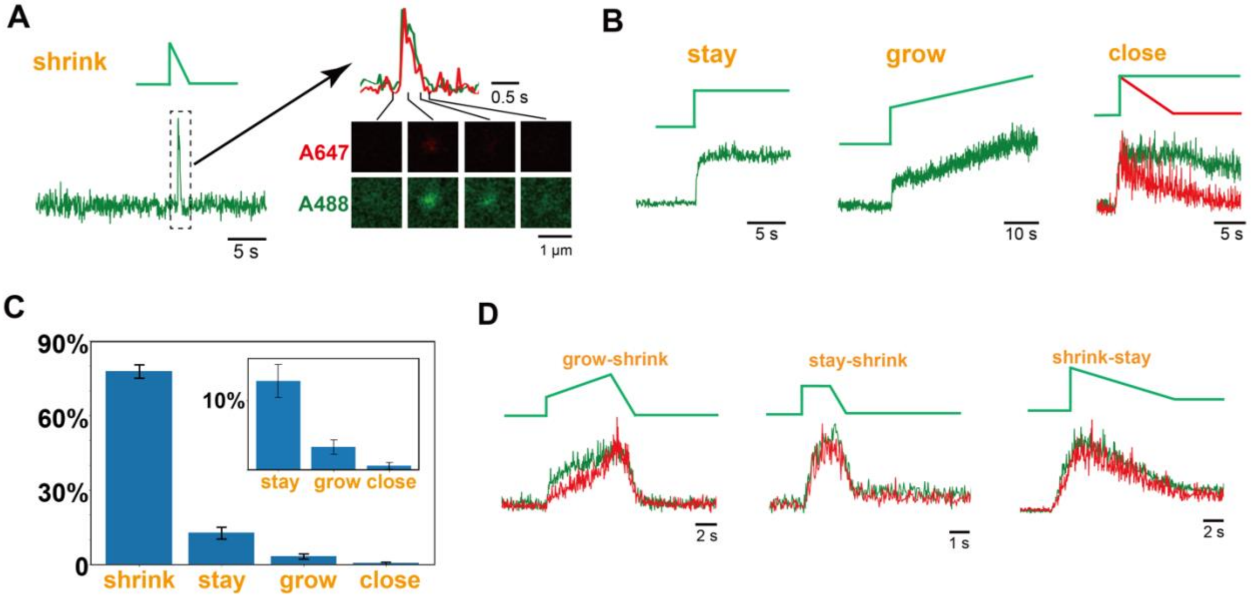

Figure 3.2. Four fundamental classes of vesicle evolution during exocytosis.
(A) Typical shrink event. Fluorescence intensity traces of the green A647 and red A488 dyes show abrupt increase at the instant of vesicle fusion, followed by a decay as the vesicle merges with the membrane. Confocal microscopy images of the spot at four times (right). Idealized intensity trace is shown (top left). (B) Fluorescence intensity traces for typical shrink, grow and close events, respectively. Symbolic trace for each is shown at top. For close events the red A488 dye trace decays to baseline, indicating a closed fusion pore. (C) Fraction of events belonging to the shrink, stay, grow, or close categories (mean ± s.e.m) in $n = 26$ movies from 9 cells (678 events total). (D) Three classes of observed composite events.

Almost half of exocytosis events are clustered at hotspots

“Hotspot” sites where repeated exocytotic release occurs have been identified in insulin-secreting endocrine cells such as INS-1 cells and pancreatic β cells (27-29). However, the functional roles of these hotspots in exocytosis regulation have not been identified.

We analyzed the present exocytosis data for evidence of hotspots. From a visual inspection of the release sites, it was evident that in some cases successive release events occurred at the same location (Fig. 3.3A), and release sites tended to be clustered (Fig. 3.3B). To quantify these observations, we calculated the cumulative pair distribution function (cdf) $P_{\text{cum}}(R)$, the mean fraction of pairs of release events occurring within distance R of each other,

Fig. 3.3C. We defined a release event to have occurred at a hotspot if its location was within 0.4 µm (the mean vesicle diameter) of at least one other release event in the same movie.

From $P_{\mathrm{cum}}(R)$, we found ~1.4% of pairwise distances being less than 0.4 µm, corresponding to ~38 % of exocytosis events (255 out of 678) occurring at hotspots. Further, for smaller separations ($R < 2$ µm) $P_{\mathrm{cum}}(R)$ is significantly greater than the cdf for completely randomly positioned sites, $P_{\mathrm{cum}}^{\mathrm{rand}}(R)$. For small R, $P_{\mathrm{cum}}^{\mathrm{rand}} = \pi R^2 < N_{\mathrm{release}}/A_{\mathrm{cell}} >/< N_{\mathrm{release}} >$ where N_{release} and A_{PM} are the total number of release events and PM area in one movie, and the average $< \cdots >$ is over all observed release events (see methods). For the random distribution, only $\sim 9.0 \pm 1.0$ % of release sites lie within 0.4 µm of another release site (~ 0.28 ± 0.05 % of pairwise distances). The chance of observing a hotspot event (38%) is four times larger than that of the random distribution (9%) Moreover, the probability distribution (pdf), minus the derivative of the cdf, exceeded the random pdf for relevant distances, $R \leq 6$ µm (Fig. 3.3D). We conclude that release sites tend to be clustered. Overall, the data provides strong quantitative evidence for a significant amount of hotspot release.

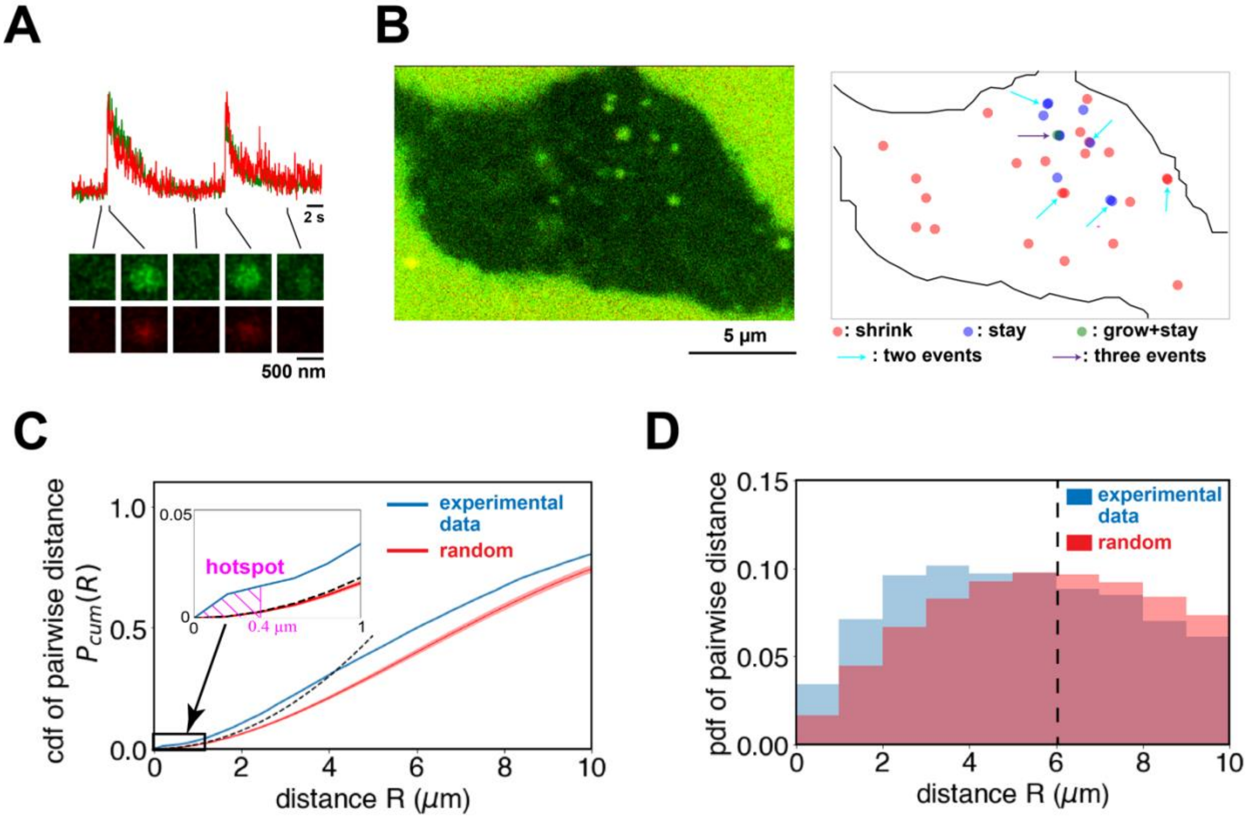

Figure 3.3. Vesicles release at hotspots.
(A) Two vesicles successively merge into the PM at a hotspot. (B) Spatial distribution of exocytosis events. The positions of all exocytosis events for a 60 s movie whose final frame of the A488 intensity is shown, are replotted regardless when they happen. Note at some places two or three vesicles fused with PM. (C) Cumulative distribution of the pairwise distance of exocytosis events. We define a hotspot exocytosis if another vesicle releases within 0.4 µm. The analytical approximation $P_{\text{cum}}^{\text{rand}} = \pi R^2 < N_{\text{release}}/A_{\text{cell}} >/< N_{\text{release}} >$ for small R is shown with black dashed lines. (D) Probability distribution function (pdf) of the pairwise distance shown in (C).

Repeated exocytosis generates a membrane reservoir storing a small proportion of added membrane

Over the course of a typical $60s - 90s$ movie, ~5-70 vesicles fused with the imaged portion of the PM of total area ~ 100-250 μm^2. Given a typical vesicle membrane area ~ 0.5 μm^2, the net vesicle membrane area added to the PM is the equivalent of $\sim 7 \pm 4\%$ ($n = 26$ movies) of the original PM area. This is a huge addition, given that the tension of a membrane is highly sensitive to its area: an additional ~ 2% of area typically suffices to lower the membrane tension to a negligibly small value (146).

Take the movie whose data shown in Fig. 3.4 as a typical example. Exocytosis added ~ 10 μm^2 to the PM by 20s, with a total of ~ 20 μm^2 added in 69 vesicles after 60s. Most of this added membrane merged with the PM, but ~ 1.5-2.2 μm^2 remained fused to the membrane as ~4-5 unmerged or slow merging (duration >10 s) vesicles (Figs. 3.4A-B). This reservoir of internal exocytosis-generated membrane was established within ~ 20s, showing only a small ~15% fluctuation in total area (1.9 ± 0.3 μm^2) over the remaining 40 s of the movie. Note that at the start of each movie ($t = 0$) a few fused vesicles are present of unknown history, most of which subsequently merge with the PM (shrink events).

A membrane reservoir storing membrane was seen for all 26 movies. The reservoir is highly dynamical: vesicles that fuse with but do not merge with the PM (stay and grow events) add the reservoir area, while the slowly merging vesicles remove the area. For >70 % of the movies (19 out of 26), the reservoir area (summed over all vesicles in the reservoir) reached a steady state within 15-30 s, while in the remaining 7 movies the reservoir area kept increasing till the end (60 or 90 s). The cause for the steady state area is rate of adding membrane by new stay or grow events is equal to the rate of removing membrane by slowly merging vesicles (or both rates go to zero at the end). Averaging over all the 26 movies, the final reservoir contains ~8 vesicles and stores ~20% of the area added by exocytosis (Fig. 3.4C).

Membrane reservoir sites are spatially correlated with hotspots

We hypothesized that the large amount of membrane added to the PM by exocytosis was the driving force for formation of the membrane reservoir. Indeed, from visual inspection, sites containing the unmerged or slowly merged vesicles that constitute the reservoir tend to be close to hotspots of repeated vesicle release, Fig. 3.4D. To test this hypothesis quantitatively, we determined the reservoir-hotspot pdf $P^{\mathrm{res-hot}}(R)$ and the reservoir-non-hotspot pdf $P^{\mathrm{res-nonhot}}(R)$, averaged over all movies (Fig. 3.4E). For all separations up to ~4 µm, $P^{\mathrm{res-hot}}$ is larger than $P^{\mathrm{res-nonhot}}$, and by summing up the pdfs, ~34% of the pairwise distance between a reservoir site and a hotspot event is within 4 µm, while only ~25% of the distance between a reservoir site and a non-hotspot event is within 4 µm. This indicates it is more likely for a reservoir site to have a hotspot neighbor than a non-hotspot neighbor.

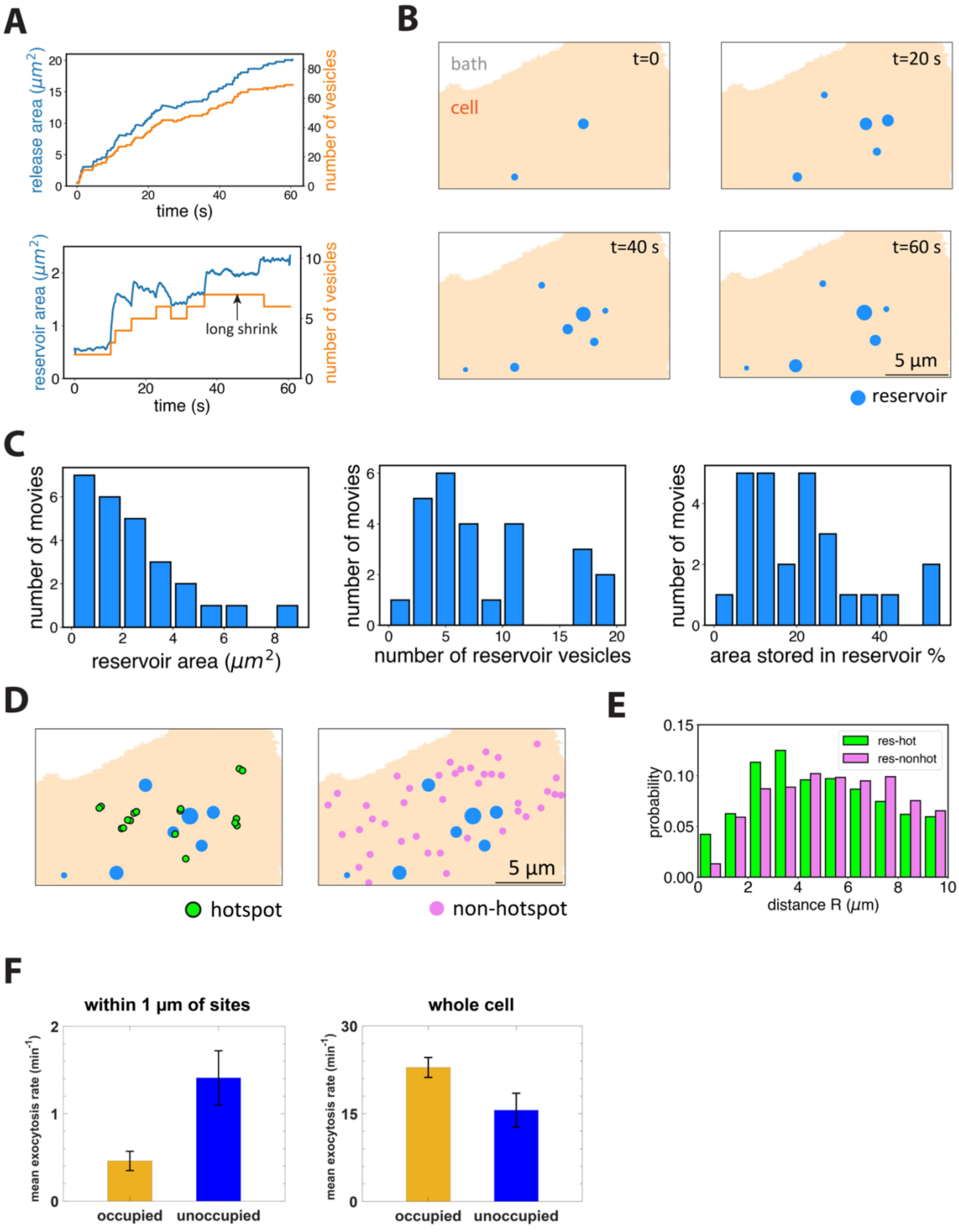
A
release area (μm^2)
number of vesicles
time (s)
reservoir area (μm^2)
long shrink
B
bath
cell
t=0
t=20 s
t=40 s
t=60 s
5 µm
reservoir
C
number of movies
reservoir area (μm^2)
number of reservoir vesicles
area stored in reservoir %
D
5 µm
hotspot
non-hotspot
E
res-hot
res-nonhot
probability
distance R (μm)
F
within 1 µm of sites
whole cell
mean exocytosis rate (min^{-1})
occupied
unoccupied

Figure 3.4. Repeated exocytosis generates a membrane reservoir spatially close to hotspots (A) A small proportion of the membrane added by exocytosis are stored in the reservoir. In an example movie, 69 vesicles fused with PM adding ~20 $\mu\mathrm{m}^2$ membrane (top), while ~5 vesicles remained unfused and contributed to the reservoir (~2 $\mu\mathrm{m}^2$, bottom). (B) Location of the reservoir sites and evolution of the vesicle size. For the movie in (A), the vesicles in the reservoir (blue) are drawn 4 times the measured length for visibility. The two vesicles appeared at $t = 0$ continuously grew and become the largest two at the end. (C) Histograms of final reservoir membrane area, final reservoir vesicle number, and the ratio of final reservoir area and the membrane area added by exocytosis for all 26 movies. The final values were averaged over the last 5 s of each movie. The final reservoir area is $2.5 \pm 2.1\ \mu\mathrm{m}^2$, consisting of 7.8 ± 5.4 vesicles and accounting for $21 \pm 14\%$ of the total membrane area added by exocytosis. (D) Location of the reservoir sites, the hotspots, and non-hotspot release events. In the same movie as (B), the hotspots (green, twice the length), the reservoir vesicles (blue, the final size for stay/grow events or the initial size for shrink events is drawn), and non-hotspot shrink events (pink, twice the length) are drawn. (E) Hotspots are closer to the reservoir than other non-hotspot shrink events. The probability distribution function (pdf) of the pairwise distance of reservoir-hotspot pairs is larger than that of reservoir-shrink pairs on small scales $R < 4$ μm, averaged $n = 26$ movies. (F) Occupied sites locally suppress exocytosis frequency. For each of the 71 sites in 26 movies, the mean exocytosis rate (number of release events divided by duration time of occupied period or unoccupied period) was measured for within 1 μm of the site (left) and the whole cell (right). Then the rate is averaged over 71 sites (mean ± s.e.m. was plotted).

An occupied reservoir site locally suppresses exocytosis frequency

How does the reservoir in turn regulate exocytosis? To answer this question, from a total of 210 reservoir sites out of all 26 movies, we selected 71 sites that have a period of being occupied and a period of being unoccupied by unmerged or slowly merged vesicles during the movie. The other sites are always occupied by vesicles during the entire movie. For these 71 sites, we measured the local time-averaged exocytosis frequency (number of release events per minute) within 1 μm of these sites, for the occupied period and unoccupied period, respectively. We found that the local exocytosis frequency averaged over these 71 sites is ~2 times lower when the site is occupied than unoccupied (Fig. 3.4F). To rule out the possibility that this ratio reflects lower exocytosis frequency of the whole cell, we measured the whole-cell exocytosis frequency for these 71 sites, during the occupied period and unoccupied period, respectively, and found the frequencies were similar (Fig. 3.4F) Thus, we conclude the reservoir suppresses the local exocytosis frequency.

Mathematical modeling suggests membrane reservoir requires plasma membrane tension below a threshold

From the above analysis we found vesicles that do not merge into the PM form a reservoir, accounting for a ~20% of the membrane added by exocytosis and spatially correlated with hotspots. Interestingly, some of the fused vesicles even grow in size. What drives formation of membrane reservoir and what determines the reservoir vesicle size?

To address this we consider a simple mathematical model of the reservoir considering effects from membrane tension and osmotic pressure. We consider a portion of the PM at tension γ_{PM} with N release sites (Fig. 3.5). The vesicles are under a squeezing pressure ΔP tending to minimize the volume of the vesicles. Such ΔP was shown to be a biophysical driving force to merge vesicles in chromaffin cells (93). The PM away from the release sites is attached to the cytoskeleton which provides adhesion energy per unit area ϵ. We ask what's the equilibrium state, or the final destiny, if N vesicles fuse with membrane at the N sites. The total free energy F of the reservoir-PM system is

$$F = F_0 + \sum_{i=1}^{N} (\gamma_{\mathrm{PM}} + \epsilon) \cdot A_i - \sum_{i=1}^{N} \gamma_i A_i + \sum_{i=1}^{N} \Delta P \cdot V_i, \quad [3.1]$$

where F_0 is the reference free energy where all N release sites are unoccupied, γ_i, A_i and V_i are the membrane tension, area and volume of the ith vesicle. In equilibrium, F is minimized with respect to A_i, such that $\partial F / \partial A_i = 0$, which gives

$$\gamma_{PM} + \epsilon = \gamma_i. \quad [3.2]$$

Under mild compression, the vesicle would adopt a spherical shape (56, 93) so its membrane tension γ_i is determined by the squeezing pressure ΔP via an equation similar to the Laplace's law but in the compression regime,

$$\gamma_i = -\frac{\Delta P \cdot R_i}{2}, \quad [3.3]$$

where R_i is the radius of the ith vesicle. Eq. 3.3 is a good approximation as long as the squeezing pressure ΔP does not exceed the critical value $\Delta P_{\mathrm{C}} \equiv 12\kappa/R_i^3$ where κ is the bending modulus of the membrane. For typical values $R = 200$ nm (for chromaffin vesicles) and $\kappa = 80$ pN · nm, ΔP_{C} is 120 Pa, which is smaller than the intracellular pressure measured in a range of cells (147).

Combining Eq. 2 and Eq. 3 gives the equilibrium vesicle radius $R_{\mathrm{eq},i}$ in the reservoir,

$$R_{\mathrm{eq},i} = -2\frac{\gamma_{\mathrm{PM}} + \epsilon}{\Delta P}. \quad [3.4]$$

Eq. 3.4 implies all reservoir vesicles adopt the same size set by the local PM tension. Any fused vesicle will shrink or grow until its radius reaches $R_{\mathrm{eq},i}$. Eq. 3.4 also implies a critical PM tension γ_{PM}^* above which the reservoir would not form,

$$\gamma_{\mathrm{PM}}^* = -\epsilon. \quad [3.5]$$

If $\gamma_{\mathrm{PM}} > \gamma_{\mathrm{PM}}^*$, Eq. 3.4 will not be suitable as it will give a negative $R_{\mathrm{eq},i}$. Instead, the R_i minimizing the free energy F (Eq. 3.1) will be zero, implying no reservoir will form. This critical tension can be reached by repeated exocytosis events as a fused vesicle will deliver large amount of low-tension lipids. This is consistent with our finding that the reservoir is spatially correlated with hotspots.

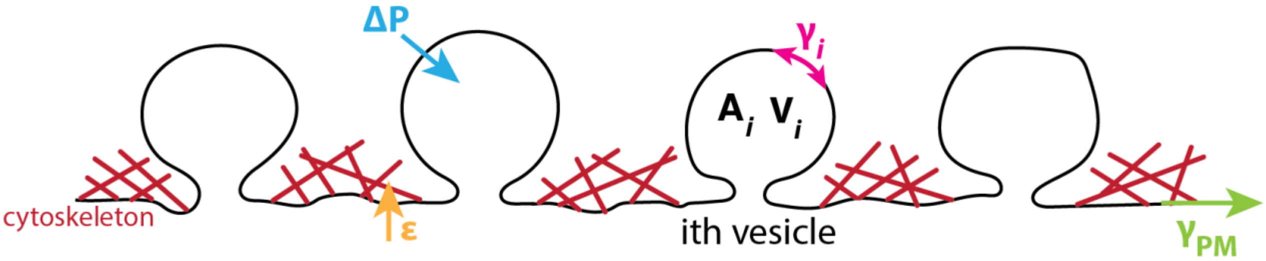
ΔP
γ_i
A_i V_i
cytoskeleton
ε
ith vesicle
γ_PM

Figure 3.5. Schematic of the mathematical model of the reservoir.
We consider a portion of PM under tension γ_{PM} with N release sites. Each release site is occupied by a vesicle under squeezing pressure ΔP. The PM away from the release site is attached to the cytoskeleton with adhesion energy ϵ.

Chapter 4: Host cell membrane capture by the SARS-CoV-2 spike protein fusion intermediate

In this chapter, I describe computational work on predicting the structure of SARS-CoV-2 spike protein fusion intermediate and measuring its membrane binding time via molecular dynamics simulations. This work has been made available on bioRxiv. Jin Zeng, a former Ph.D. student in the O'Shaughnessy group, also contributed to this work. The cryo-electron tomography data that this computational study compared to were obtained by Dr. Tara Marcink from Professor Anne Moscona's lab at Columbia University.

4.1 Introduction

The COVID-19 global pandemic is this century's third coronavirus epidemic following SARS-CoV in 2002 and Middle East respiratory syndrome coronavirus (MERS-CoV) in 2012, suggesting that coronaviruses will remain a global health threat for the foreseeable future. The responsible pathogen is the severe acute respiratory syndrome coronavirus 2 (SARS-CoV-2), a ~100-nm diameter betacoronavirus (148) whose lipid envelope encloses a positive-sense single-stranded RNA genome complexed with the nucleocapsid (N) protein. The lipid envelope houses the spike (S) glycoprotein, the envelope (E) protein and the membrane (M) protein (149). The S protein is a trimeric class I fusion protein that catalyzes entry into lung, nasal mucosa or small intestine cells and has two subunits, S1 and S2 (150, 151). Following S1-mediated binding to host cell membrane Angiotensin-Converting Enzyme 2 (ACE2) receptors and proteolytic activation at locus S2′ by TMPRSS2 on the plasma membrane (PM) (152) or by endosomal cathepsins B and L (153), S1 and S2 are thought to dissociate, releasing S2.

Entry is the job of the S2 subunit, by fusion of the viral envelope and host cell membrane. To become fusion competent, S2 must first undergo a major structural transition from its prefusion state to the potent, fusogenic form, the extended fusion intermediate (FI) (154, 155) which bears three N-terminal fusion peptides (FPs) that capture the host cell membrane. Subsequent refolding of the fusion intermediate into its postfusion configuration (156) pulls the viral envelope and target membrane together for fusion and delivery of viral genomic material (157).

The fusion intermediate is the unsheathed weapon of CoV-2 entry, but the mechanism and timescales of FI-mediated host cell membrane capture are unknown. Little is known about this critical machinery. While the prefusion and postfusion CoV-2 S protein structures are known from cryo-EM and x-ray crystallography (150, 156, 158, 159), the FI structure is undetermined. Extended intermediate states of class I fusion proteins have generally proved experimentally elusive, likely due to their estimated sec-min lifetimes, far shorter than the pre- or postfusion lifetimes (154, 160, 161) . Indeed, no class I fusion protein intermediate had been visualized until very recently, when the HIV-1 gp41 intermediate, the parainfluenza F intermediate and the influenza HA2 intermediate (161-163) were visualized with cyro-EM for the first time.

The spike protein is a target for vaccines, therapeutic antibodies and other antivirals. Most current recombinant neutralizing or vaccine-elicited antibodies to CoV-2 bind S1 (164-167). Viral fusion inhibitors targeting S2 (159, 168) and the fusion-executing subunits of other class I fusion proteins have been developed, including one FDA-approved drug against HIV (169-171). Importantly, recently emerged CoV-2 variants harboring spike protein mutations, B.1.351 (South African variant) and P.1 (Brazilian variant), escaped from two S1-targeting antibodies one of which has FDA emergency authorization, whereas the efficiency of S2-targeting antivirals was unaffected (172). Moreover, S2 is conserved among coronaviruses (99).

Thus, unveiling the mechanisms of the CoV-2 S2 fusion intermediate will be vital in the search for robust and pan-coronavirus antiviral drugs.

Detailed computational studies of the CoV-2 FI and the kinetics of FI-mediated membrane capture are unavailable, to our knowledge. However the prefusion S protein was atomistically simulated (173-175), one study revealing a highly flexible prefusion structure due to three hinge-like regions, consistent with cryo-ET (174). Membrane binding by the isolated FP was simulated (176-178), including Ca^{2+}-dependent binding which involved the conserved coronavirus LLF motif in the N-terminal FP helix (176). A coarse-grained model of the whole virion was developed (179). For other class I fusion proteins, a model structure of the Ebola GP2 extended intermediate was constructed (180) and local transitions of the influenza HA and HIV gp41 intermediates were modelled (181, 182).

Here, we constructed a full-length structural model of the CoV-2 FI by extrapolating from known CoV-2 pre- and postfusion structures. The model suggests a “loaded spring” mechanism triggers the prefusion-to-FI transition, similar to that for influenza HA thought triggered by folding of the B-loop into a helix (183). We studied membrane capture by the FI, using all-atom (AA) and MARTINI coarse-grained (CG) molecular dynamics (MD) simulations to access timescales up to a ms. Simulations showed the FI is highly flexible, subject to large orientational and extensional fluctuations due to three hinges in the C-terminal base closely related to the prefusion hinges (174). These fluctuations greatly increased the volume swept out by the FI, helping it capture target cell membrane. The highly liberal FI configurations in the simulations agree well with the recent cryo-ET data showing flexible FIs spanning the membranes, which strongly supports our proposed FI model. A critical N-terminal amphiphilic helix in the FP mediates membrane binding, but we find FP-only simulations severely mispresent the kinetics, as membrane capture is far slower in the native structure with the FP attached to the FI. Our CG simulations suggest FI-mediated membrane capture requires ~ 2 ms, a critical step on the pathway to fusion. In addition to facilitating membrane capture, we propose that large FI fluctuations set the timing of fluctuation-triggered FI refolding on the pathway to membrane fusion. Our work identifies several novel potential drug targets.

4.2 Results

Model of the CoV-2 spike protein fusion intermediate

Entry of SARS-CoV-2 is catalyzed by the trimeric S protein, consisting of three S1 heads sitting upon a trimeric S2 stem (150). Following binding of S1 to the host cell ACE2 receptor (152), S1 dissociates from S2 (184) and the prefusion S2 trimer undergoes a major structural transition to its potent, fusogenic form, the fusion intermediate (FI) (154) (Fig. 4.1A).

We predicted the structure of the FI based on information from the partially solved pre- and postfusion cryo-EM structures (156) (Figs. 4.1B-C). A natural question is whether formation of the FI from its prefusion state uses a load spring mechanism similar to that used by influenza HA for the analogous transition (183). We hypothesized that in S2 a transition converts the prefusion heptad repeat 1 (HR1) domain into a continuous alpha helix, itself continuous with the downstream central helix (CH). That is, all unstructured loop domains in HR1 become helical and rotate like torsional springs, straightening HR1 (Figs. 4.1A, 4.1D). The result is a three-helix HR1-CH coiled coil in the FI trimer, the mechanical backbone of the FI. The hypothesis is tantamount to assuming CH and HR1 adopt their postfusion structures in the FI, since the postfusion HR1 and CH are continuous helices in a trimeric coiled coil (156) (Fig. 4.1C).

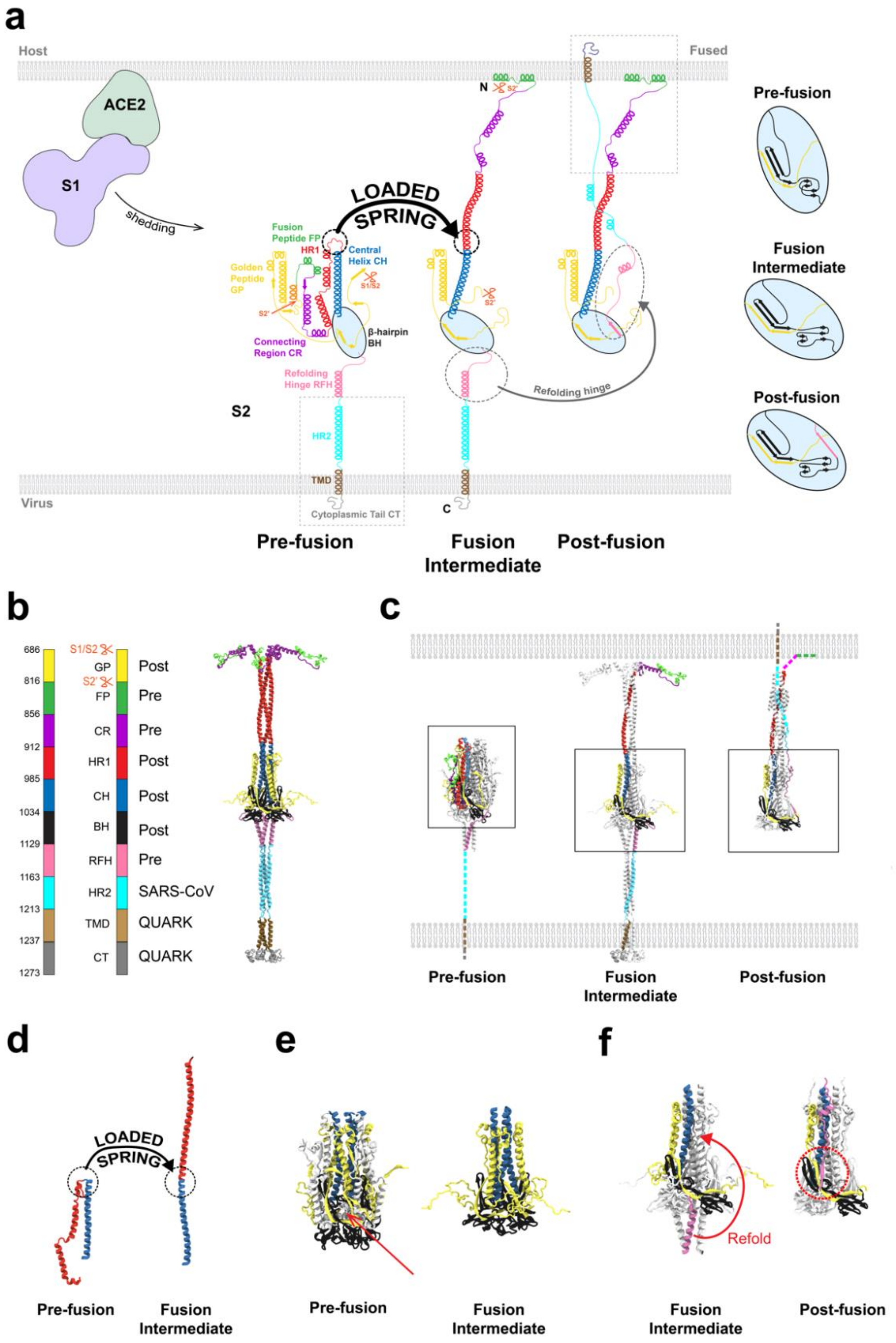
a
Host
Fused
ACE2
S1
shedding
LOADED SPRING
N
S2'
Fusion Peptide FP
HR1
Central Helix CH
Golden Peptide GP
S1/S2
S2'
Connecting Region CR
β-hairpin BH
Refolding Hinge RFH
S2
HR2
TMD
Cytoplasmic Tail CT
Refolding hinge
C
Virus
Pre-fusion
Fusion Intermediate
Post-fusion
Pre-fusion
Fusion Intermediate
Post-fusion
b
686
816
856
912
985
1034
1129
1163
1213
1237
1273
S1/S2
GP
S2'
FP
CR
HR1
CH
BH
RFH
HR2
TMD
CT
Post
Pre
Pre
Post
Post
Post
Pre
SARS-CoV
QUARK
QUARK
c
Pre-fusion
Fusion Intermediate
Post-fusion
d
LOADED SPRING
Pre-fusion
Fusion Intermediate
e
Pre-fusion
Fusion Intermediate
f
Refold
Fusion Intermediate
Post-fusion

Figure 4.1. Model of the SARS-CoV-2 spike protein fusion intermediate.
(A) Model of the fusion intermediate (FI) of the CoV-2 spike (S) protein, schematic. One protomer of the S trimer is shown. Schematics of the pre- and postfusion S2 states from the known structures, other than unknown regions (boxed). Details of BH and adjacent domains, at right. Following dissociation of S2 from S1, the unstructured pre-fusion HR1 loops become helical (loaded spring release), giving the HR1-CH backbone that thrusts the FPs toward the host cell membrane. The FI subsequently refolds into the postfusion structure, driven by structural changes in RFH and chaperoned by GP, with RFH and HR2 providing leashes that pack the HR1-CH backbone grooves. (B) Model of the FI of the CoV-2 spike (S) protein, exact structure. Source structures for each S2 subunit domain are indicated, either CoV-2 prefusion (PDB: 6XR8), CoV-2 postfusion (PDB: 6XRA) or HR2 of CoV (PDB: 2FXP). Transmembrane domain (TMD) and cytoplasmic tail (CT) structures predicted by QUARK. (C) Comparison between predicted FI structure and known crystal structures of the prefusion (PDB: 6XR8) and postfusion (PDB: 6XRA) CoV-2 S2 subunit. One protomer highlighted in color. Dashed lines: missing domains from partially solved crystal structures. (D) Details of loaded spring transition. (E) β-hairpin (BH) domains in the known prefusion and predicted FI structures (boxed regions of (C)). The RFH domain is omitted from the FI BH for clarity. Following the loaded spring transition, HR1, CR and FP (shown faint in the prefusion BH) vacate their prefusion locations in BH. The resultant cavity (arrow) would presumably be unstable. We assume the FI adopts the more compact postfusion BH structure (right). (F) The golden peptide (GP) domain chaperones refolding of the fusion intermediate (FI) into the postfusion structure. Blowups of boxed regions in (C) are shown. Refolding of the refolding hinge (RFH) domain is guided by GP. RFH forms a parallel β-strand with GP (red circle), the RFH unstructured portion packs the CH-GP groove, and RFH helices interact with two GP helices. Colored BH and CH belong to one protomer; colored RFH belongs to a different protomer.

The S2′ site is assumed cleaved before this transition, exposing the FP N-terminus ready for host membrane capture, consistent with CoV-2 lung cell entry being blocked by inhibition of the serine protease TMPRSS2 that cleaves S2′ at the host cell plasma membrane (152). This cleavage disconnects the golden peptide (GP) domain, but GP remains physically attached to S2 (156). (We tested an uncleaved model with connected GP and FP, but the FPs were sequestered and unable to access the target membrane, Fig. S4.1.)

We assumed the β-hairpin (BH) domain adopts its postfusion configuration in the FI. Straightening of HR1-CH pulls these domains away from their prefusion locations and would leave large destabilizing cavities in BH, favoring transition to the postfusion configuration where

BH is raised to fill the cavities and assembles into a pyramidal base (Fig. 4.1E). The same is assumed of GP, since a GP β-strand interacts strongly with an antiparallel β-sheet in BH (Fig. 4.1A). GP also contributes two small helices, and a long helix in a CH coiled coil groove completing a six-helix bundle (Figs. 4.1A, 4.1E) providing structural support at the base of the CH-HR1 backbone (see below).

Downstream of BH the refolding hinge (RFH) domain, remote from the loaded springs, was taken as the prefusion structure, while we used the HR2 structure of SARS-CoV from NMR (185) whose HR2 sequence is the same as that of CoV-2 (159). The unknown TM and CT structures were predicted by QUARK (186).

These components were integrated into the predicted CoV-2 FI structure shown in Fig. 4.1B (see Appendix). The model implies that subsequent refolding of the FI to the postfusion conformation occurs by the unstructured N-terminal loop of the refolding hinge (RFH) domain folding into BH by contributing a β-strand to an antiparallel β-sheet (Figs. 4.1A, 4.1F). The remainder of RFH folds back as a leash packing a GP-CH groove in the six-helix bundle, ending in a small helix that attaches between the two small GP helices of the other two protomers, oriented almost perpendicular to the HR1-CH backbone. Refolding is completed when the helical HR2 becomes partially unstructured to pack a second leash into a HR1-CH groove and supply one helix to a six-helix postfusion bundle with HR1, the fusion core (156).

All-atom simulation of the fusion intermediate

Using complementary atomistic and coarse-grained MD methods, we tested the FI model of Fig. 4.1B and measured its configurational statistics and dynamics (see Appendix).

During ~ 0.4 μs of AA simulation the basic secondary structure remained unaltered (Fig. S4.2), lending credibility to the model. Far from the rigid extended object one might anticipate given its long helical domains (Fig. 4.1B), the FI was highly flexible and underwent large configurational fluctuations, adopting bent configurations without structural damage (Fig. 4.2). The structural robustness was due to energy-absorbing features. The RFH-HR2 base region downstream of the BH domain was highly flexible, allowing large tilt (Fig. 4.2B). Relative to the prefusion structure the three RFH helices, known as the stem helices, became splayed with separated N-termini, in an inverted tripod suspension system that buffered large displacements of the upstream BH and backbone. The HR2 helices became partially unstructured, a structural plasticity that helped the FI tilt to greater angles at the membrane (Fig. 4.2B).

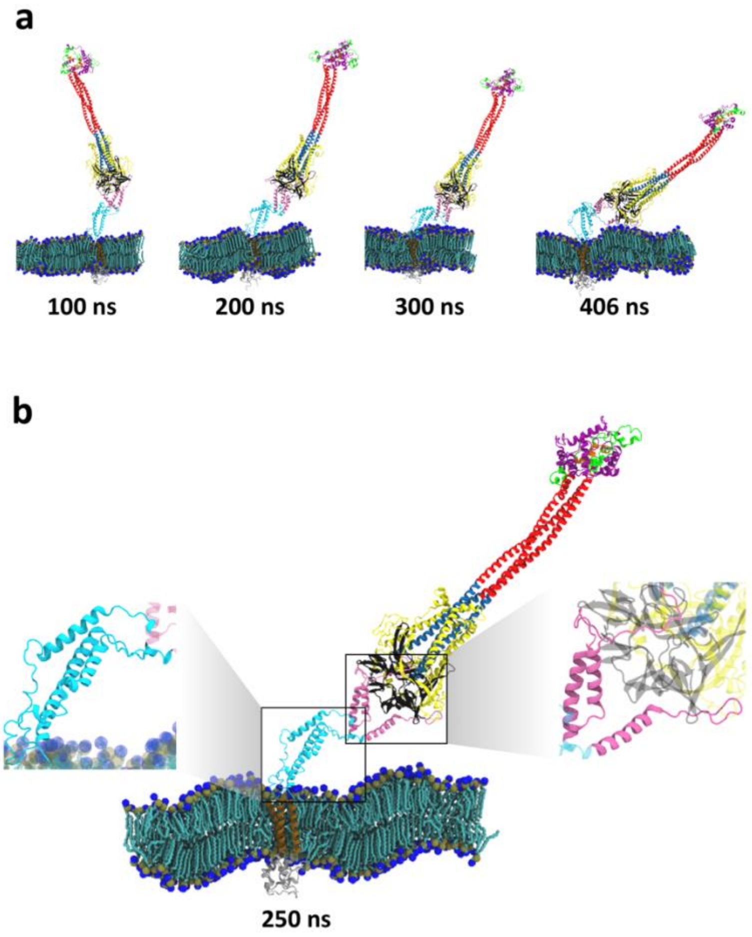

Figure 4.2. All-atom simulation of the SARS-CoV-2 fusion intermediate
Color code for this and all subsequent Figures., as for Fig. 4.1. In addition, the N-terminal helices of the fusion peptides are shown orange. (A) Snapshots of the FI during the ~ 0.4 μs all-atom simulation of the model of Fig. 4.1B. The FI undergoes large bending and

extensional fluctuations. (B) Snapshot of the FI after 250 ns of the AA simulation. The RFH and HR2 domains (highlighted) show secondary structural plasticity. Relative to the prefusion structure, the RFH stem helices splayed into an inverted tripod that behaves as a mechanical suspension system for the BH and GP domains and the HR1-CH backbone. The HR2 secondary structure is dynamic. Bending of the FI stretched the outermost HR2 helices, triggering partial conversion into unstructured sections.

Three hinges endow the fusion intermediate with high flexibility

Next we measured longer time FI dynamics using MARTINI CG simulations which fix the secondary structure but access timescales two orders of magnitude beyond those accessible with AA.

In 40 μs total running time over 5 runs, the FI exhibited large configurational fluctuations as in the AA simulation, bending and reorienting over a wide range of angles (Figs. 4.3A, 4.3C). To quantify the flexibility we measured the curvature statistics along the FI (Figs. 4.3B, S4.3, and Appendix). This procedure identified three high flexibility hinge regions in the base, with similar mean magnitudes of curvature and large fluctuations (Fig. S4.4). Mapping back to the atomistic structure located the hinges as unstructured loops at the BH/RFH, RFH/HR2 and HR2/TMD interfaces, respectively (Figs. 4.3B-C).

These hinges have roughly the same locations as three hinges identified in the prefusion CoV-2 S protein by a study combining cryo-ET and MD simulations (174). Thus we adopt the “ankle, knee, hip” notation of that study. However, the hip hinge (RFH/BH interface) in the FI structure is more flexible than the prefusion hip due to the significantly altered RFH structure with splayed stem helices (Fig. 4.2B).

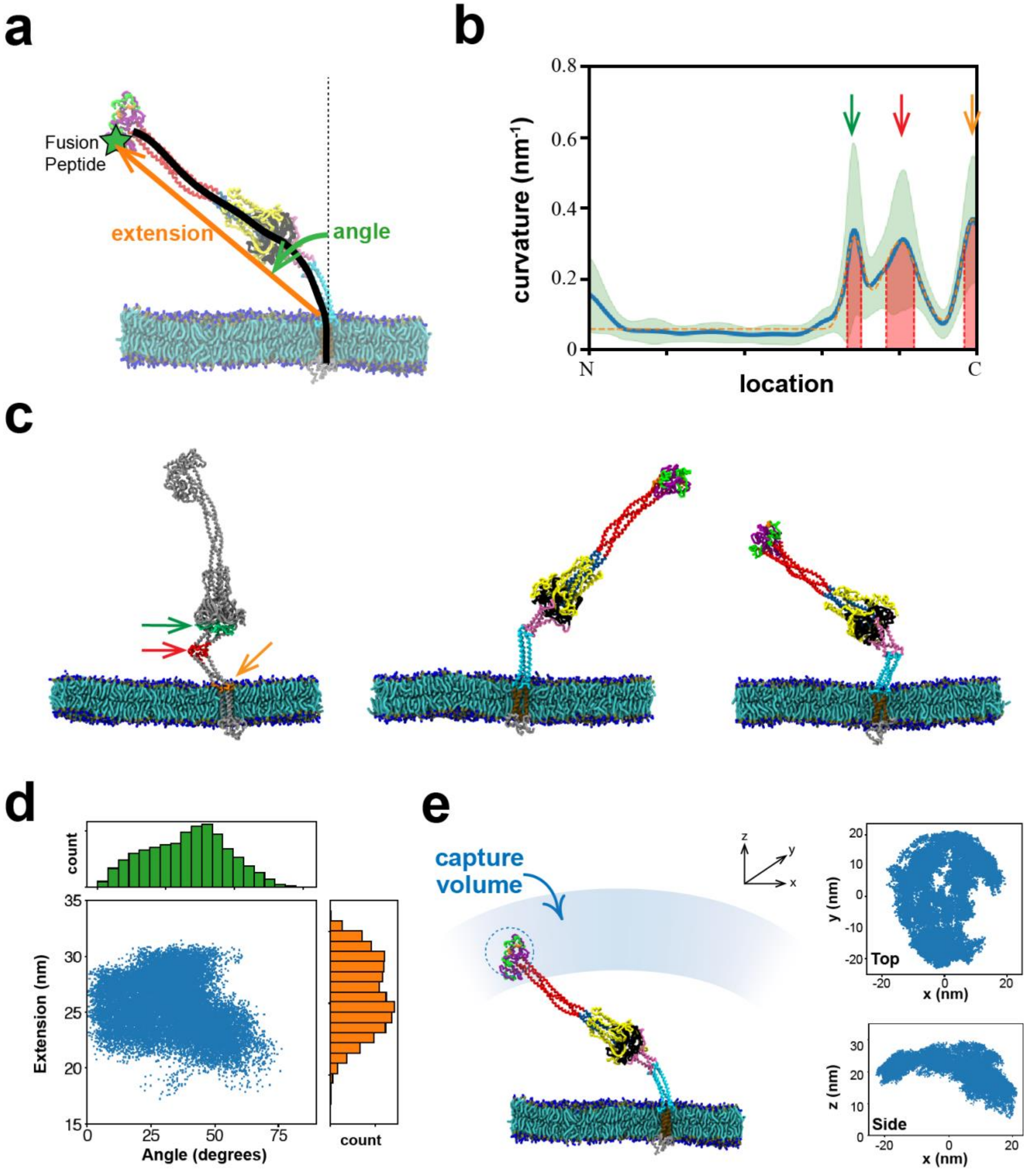

Figure 4.3. The fusion intermediate is highly flexible and visits a large capture volume. (A) In coarse-grained MARTINI simulations the FI had large configurational fluctuations, measured by the extension and angle of orientation of the FI backbone (black curve). (B) Time averaged backbone curvature versus normalized backbone arclength. Three high curvature hinges are apparent (arrows). Each hinge region (red) was defined as the quarter width of a fitted Gaussian (orange). Green envelope indicates SD. (C) Simulation snapshots

with the three hinges highlighted, identified as residues 1084-1138, 1156-1178 and 1204-1213. (D) Distributions of FI extensions and angles. (E) The FI has a large capture volume. Top and side views of FP locations visited. The FI extension and orientation ranges are ~21-30 nm and of $\pm 56°$, respectively (95% of sampled values) so that a large capture volume is swept out over time, shown schematically (left). Dashed circle: approximate region explored by the FP in 1 μs. (B), (D), (E) Statistics are averages over the last 4 μs of five 8 μs runs, for a total of 20 μs simulation time.

Large fluctuations of the fusion intermediate lead to a large membrane capture volume

The first task of the unleashed FI is thought to be capture of the host target membrane by insertion of the fusion peptides at the protomer N-termini. Due to its flexibility the FI extension ranged from ~ 21-30 nm (mean ~ 26 nm), its orientation varied over angles ~ $\pm 60°$ to the membrane normal, and the FPs in consequence swept out a volume ~ 25,000 nm^3 at rate ~ 750 nm^3 $\mu\mathrm{s}^{-1}$ (Figs. 4.3D-E, 95% of sampled locations).

Thus, due to the flexible base hinges combined with the large reach of the HR1-CH backbone, the FI accesses a substantial capture volume, equivalent to that of a ~ 36-nm-diameter sphere. Following dissociation of S2 from the S1/ACE2 complex, this may help the virus rapidly reconnect with the host cell and limit refolding back into the virion membrane in a postfusion configuration without host cell contact. Indeed, postfusion spike proteins were observed by cryo-ET on intact SARS-CoV-2 virions (187).

Structure and dynamics of the membrane-bound fusion peptide

We used a multiscale approach to study the secondary structure and spatiotemporal statistics of the membrane-bound FP removed from its host FI (Fig. 4.4A). The FI model of Fig. 4.1B assumed the prefusion FP, but once bound its structure likely changes in the radically altered membrane environment. Thus we used CG MARTINI MD to bind and equilibrate the bound FP (24 μs total), followed by 2 μs of AA simulation to realistically evolve the bound secondary structure (Fig. 4.4B).

During the AA simulation the secondary structure evolved (Figs. 4.4B-C). The N-terminus helix barely changed, but the two C-terminal helices merged into one. (The mean total helix content was 35%, compared to ~20% from circular dichroism spectroscopy (188), a difference possibly explained by the differing simulated and experimental membrane compositions.) The equilibrated helices were amphiphilic and anchored the FP to the membrane with hydrophobic and hydrophilic residues oriented towards and away from the membrane, respectively (Figs. 4.4D-E).

In an 80 μs CG simulation we then measured the statistics of the bound, equilibrated FP. The depth of residues decreased somewhat (Fig. S4.5A), and the C-terminal helix became repeatedly unanchored (Fig. S4.6). The bound FP had rms length ~ 1.5 nm and width ~ 0.9 nm, defined as the greater and smaller of the gyration tensor eigenvalues in the x-y plane, while the rms thickness was ~ 1.0 nm (Figs. 4.4F, S4.7 and Appendix). The FP extended with the anchored helices at either end, roughly speaking, as the length was strongly correlated with their separation. The radius of gyration autocorrelation function revealed a configurational memory time of ~ 270 ns (Fig. 4.4G), with similar times for the length, width and thickness (Fig. S4.8).

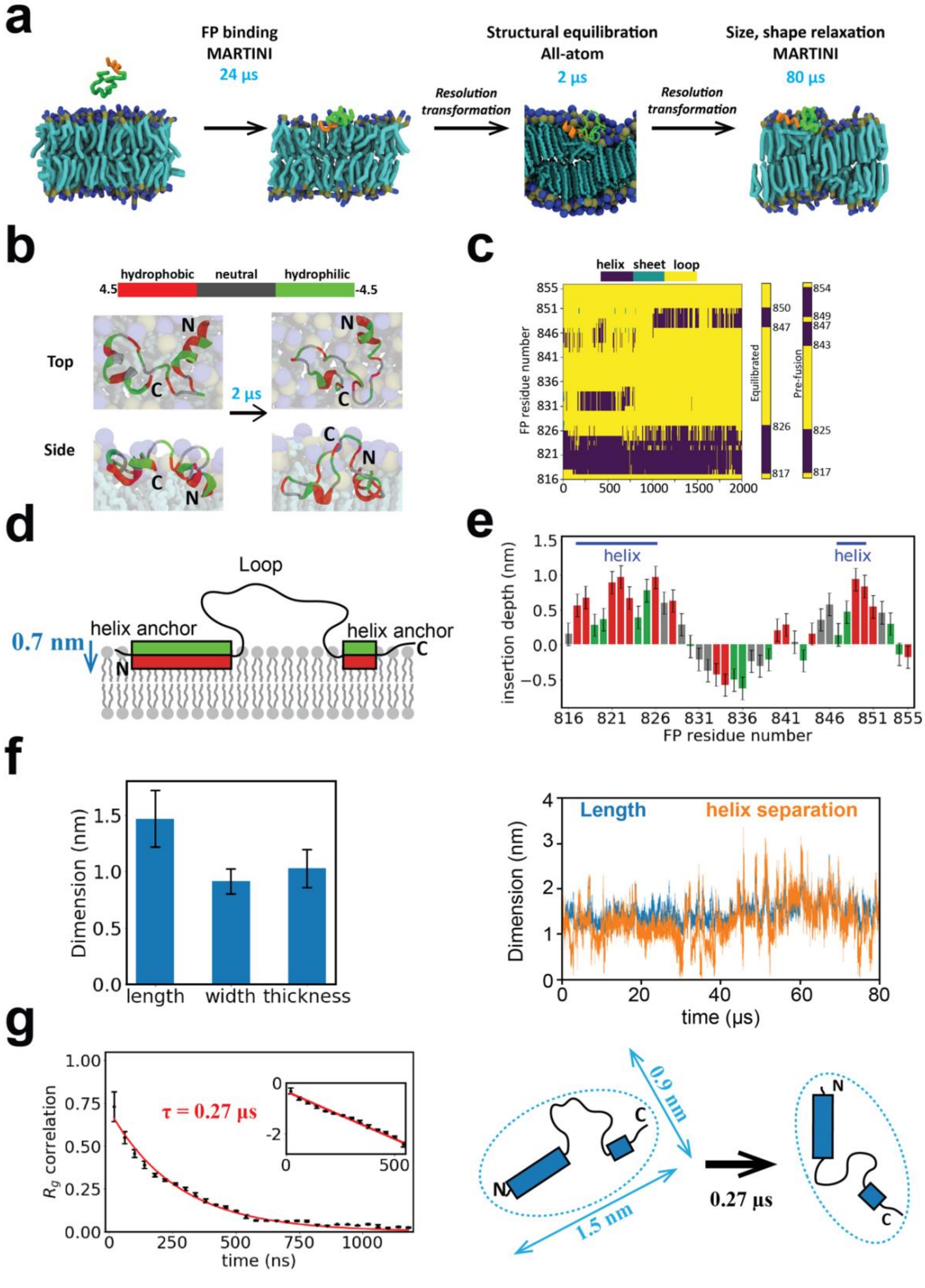
a
FP binding
MARTINI
24 µs
Resolution transformation
Structural equilibration
All-atom
2 µs
Resolution transformation
Size, shape relaxation
MARTINI
80 µs
b
hydrophobic
neutral
hydrophilic
4.5
-4.5
Top
Side
N
C
2 µs
c
helix
sheet
loop
FP residue number
855
851
846
841
836
831
826
821
816
0
500
1000
1500
2000
Equilibrated
850
847
826
817
Pre-fusion
854
849
847
843
825
817
d
Loop
helix anchor
helix anchor
0.7 nm
N
C
e
helix
helix
insertion depth (nm)
1.5
1.0
0.5
0.0
−0.5
816
821
826
831
836
841
846
851
855
FP residue number
f
Dimension (nm)
1.5
1.0
0.5
0.0
length
width
thickness
Length
helix separation
Dimension (nm)
4
3
2
1
0
0
20
40
60
80
time (µs)
g
R_g correlation
1.00
0.75
0.50
0.25
0.00
0
250
500
750
1000
time (ns)
τ = 0.27 µs
0
-2
0
500
0.9 nm
1.5 nm
0.27 µs
N
C

Figure 4.4. Multiscale simulations of the membrane-bound fusion peptide.
(A) Multiscale simulation strategy to measure secondary structure and spatiotemporal statistics of the membrane-bound FP. The prefusion structure is coarse-grained to MARTINI representation and bound to and relaxed within the membrane in a $24\ \mu\mathrm{s}$ simulation (binding required ~ $4\ \mu\mathrm{s}$). Following backmapping to atomistic resolution, the secondary structure of the membrane-bound FP is relaxed in a $2\ \mu\mathrm{s}$ AA simulation. Assigning each residue its most frequently visited secondary structure during the final 0.8 µs of the AA simulation, the FP is again coarse-grained and its spatial dimensions and relaxation time measured in an 80 µs CG simulation. (B) Evolution of FP structure during the $2\ \mu\mathrm{s}$ AA simulation of (A). Initial and final states are shown. FP resides in one of three colors depending on the hydrophobicity. (C) Evolution of bound FP secondary structure during the $2\mu\mathrm{s}$ AA simulation of (A). The initial (prefusion) and final (equilibrated) structures are compared. For each residue the equilibrated structure shows the most frequently adopted in the final 0.8 µs. (D) Equilibrated bound FP following the AA equilibration of (A), schematic. The principal anchor is the amphiphilic N-terminal helix, with a secondary amphiphilic C-terminal helix anchor. Hydrophobicity color scheme as for (B). (E) Mean membrane insertion depth profile along the bound FP in the equilibrated structure represented in (C) (see Appendix). Mean values over 0.8 µs. (F) Length and helix separation of the bound FP during the $80\ \mu\mathrm{s}$ MARTINI simulation of (A). Mean dimensions averaged over the final $78\ \mu\mathrm{s}$ (left). (G) Temporal correlation function of the radius of gyration of the bound FP yields shape memory time $\tau = 269 \pm 1\ \mathrm{ns}$. (Bin size, 40 ns. 100 data points per bin.) Inset: log-lin representation. Dashed lines: exponential fit. Top view, schematic (right). All error bars: SD.

Measurement of fusion peptide-membrane binding rate constant

The target membrane is captured by insertion of the fusion peptide. To quantify the binding kinetics, we removed a FP from its FI host and measured the binding rate constant between two membranes separated by $h = 5.5$ nm (Fig. 4.5). The binding time itself is not an invariant quantity, as it depends on the proximity of the membranes.

Defining a collision as an approach to within the rms FP end-to-end distance, $R_{\mathrm{FP}} \sim 1.6$ nm, the FP collided ~ 27 times per µs with the membrane before irreversibly binding (Fig. S4.9). Thus, effects of initial condition dependence and diffusion-control were negligible (189). Averaged over 10 CG MARTINI simulations the unbound probability decayed exponentially with time constant $\tau_{\mathrm{bind}} \sim 4.0 \pm 0.6$ µs (Fig. 4.5A). The binding rate constant k_{bind} is defined by an imagined situation with a solution of FPs at density c_{FP} contacting a membrane, such that $d\rho/dt = k_{\text{bind}}\, c_{\text{FP}}$ where ρ is the areal number density of bound FPs (189). From the binding assay,

$$k_{\text{bind}}^{\text{FP}} = \frac{h}{2\,\tau_{\text{bind}}} \approx 0.7\ \text{nm}\ \mu\text{s}^{-1}, \quad [\mathbf{4.1}]$$

where the factor of 2 reflects the two membranes.

Importantly, binding was mediated by the N-terminal helix of the FP, which provided first contact with the membrane during a binding event (Fig. 4.5B). Since cleavage at the S2′ site would expose this helix, this is consistent with this cleavage being required for viral entry (152).

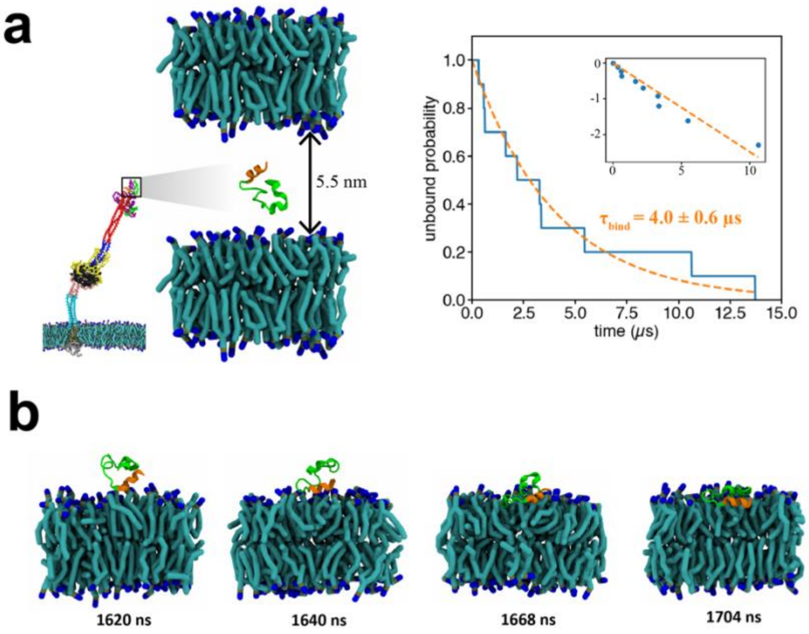

Figure 4.5. Membrane binding kinetics of an isolated fusion peptide.
(A) Binding assay to measure the membrane binding rate constant, $k_{\text{bind}}^{\text{FP}}$, of a FP removed from its host FI. Initially the FP is positioned between two membranes separated by 5.5nm (left). FP dynamics are simulated using the CG MARTINI force field and the time to irreversibly bind the membrane is measured. The unbound fraction (blue, right) among ten simulated FPs decays exponentially with time constant $\tau_{\text{bind}} = 4.0 \pm 0.6$ μs (dashed orange curves). Inset: log-lin representation. (B) Typical binding event. The N-terminal helix (orange) is the first binding contact. To show secondary structure, the FP was back-mapped to all-atom representation.

The fusion intermediate captures target membrane on a millisecond timescale

Next we studied membrane capture by the full FI (Fig. 4.6A). Surprisingly, membrane binding was so much slower than suggested by the binding kinetics of the removed FP (Fig. 4.5) as to be unobservable on available computational timescales. However, we observed binding of a truncated FI, from which we inferred a membrane capture time by the full FI of ~ 2ms.

We simulated the full FI in the presence of a target membrane 20 nm from the viral membrane. Enabled by its high flexibility hinges, the FI adopted highly bent shapes in which the FPs were oriented toward the membrane (Fig. 4.6A). However, we recorded no FP-mediated binding events during a total ~ 300 μs of CG simulation over 20 independent runs (see Appendix). Thus, binding is much slower when the FPs are attached to the FI. The FP-only binding kinetics are unrepresentative, as they suggest the FI will bind at rate ~ $k_{\mathrm{bind}}^{\mathrm{FP}}\, c_{\mathrm{FP}}^{1}(0)$ where $c_{\mathrm{FP}}^{1}(0) \sim 1/\Delta z$ is the 1D FP density evaluated at the membrane and $\Delta z \sim 10$ nm is the spread of FP N-terminal helix distances from the membrane (Fig. S4.10). This yields a binding time $\tau_{\mathrm{bind}} \sim \Delta z / k_{\mathrm{bind}}^{\mathrm{FP}} \sim 15$ μs, clearly a huge underestimate.

It is unclear if binding is computationally accessible even with CG dynamics, given that longer than ~ $.3$ ms is required. Thus we accelerated the kinetics by truncating the FI, excluding all domains downstream of HR1. We measured the binding time of this partial FI, consisting of HR1, CR and FP domains only, between two membranes separated by 8.3 nm (Fig. 4.6B). In two of six runs each lasting 160 μs, the membrane was captured by insertion of the N-terminal helix of one FP, after 23 μs and 133 μs. (In another case, binding was followed by unbinding after ~42 μs.) This implies a best estimate of ~390 ± 280 μs for the mean time for the partial FI to bind in this assay (see Appendix).

To translate this result to binding of the full FI, we measured the fractions of time for which one of the three FP N-terminal helices lies within 1 nm of the membrane. The full FI satisfied this criterion ~ 5-fold less frequently than did the partial FI (~0.07% vs. ~0.33%, Fig. 4.6C and Appendix), suggesting membrane binding is ~ 5-fold slower than in the partial FI assay. Thus we estimate the target membrane is captured by the full FI after ~ 2 ms.

Finally, to verify the full FI is capable of maintaining a bound state, we enforced binding by pulling the FP of an FI into the membrane (Fig. 4.6D). The FP remained stably bound for all of an 8 μs simulation.

Fusion peptides and connecting regions form a disordered cluster

These results show that the ability of the FP to access target membrane is strongly constrained by its local environment in the FI. In the CG simulations this environment was a disordered cluster that the FPs and neighboring CR domains organized into, laterally extended at the N-terminal end of the HR1-CH backbone (Fig. 4.6E). We call this the head of the FI. Two of the three FP N-terminal helices resided at one end of the head, and one more exposed helix at the other. With the host membrane ~ 20 nm away, likely imposed by the earlier S1-ACE2 binding episode, the FI is severely bent (Fig. 4.6E). The lateral orientation of the head appears optimal for presenting the helices to the membrane for binding in this bent configuration.

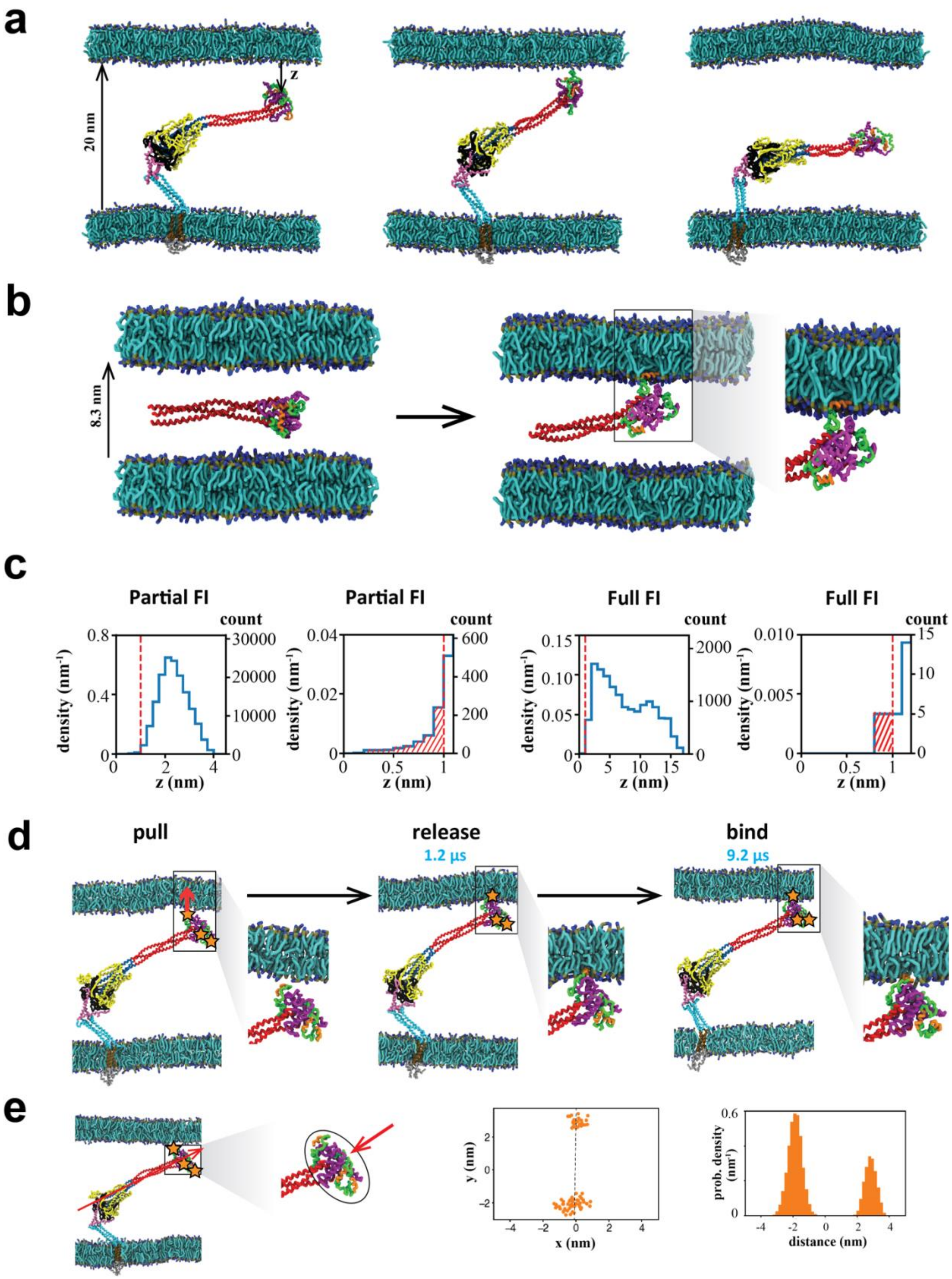
a
20 nm
z
b
8.3 nm
c
Partial FI
density (nm⁻¹)
count
0.8
0.4
0
30000
20000
10000
0
0
1
2
3
4
z (nm)
Partial FI
0.04
0.02
0
600
400
200
0
0
0.5
1
z (nm)
Full FI
0.15
0.10
0.05
0
2000
1000
0
0
5
10
15
z (nm)
Full FI
0.010
0.005
0
15
10
5
0
0
0.5
1
z (nm)
d
pull
release
1.2 μs
bind
9.2 μs
e
y (nm)
x (nm)
2
0
-2
-4
-2
0
2
4
prob. density (nm⁻¹)
0.6
0
distance (nm)
-4
-2
0
2
4

Figure 4.6. Interaction of the fusion intermediate with a target membrane.
(A) Snapshots from CG MARTINI simulations of the full FI in the presence of a target membrane 20 nm from the viral membrane. The N-terminal helices of the FPs are shown orange. (B) Simulation of membrane binding by a truncated FI consisting of the HR1, CR and FP domains between two target membranes. Initial condition (left). Binding was mediated by the N-terminal FP helix (right). (C) Probability density versus distance *z* of the nearest N-terminal FP helix from the membrane during simulations of membrane binding by the partial or full FI. In both cases the density is depleted close to the membrane. The net probability for the N-terminal helix of the FP to lie within 1 nm of the membrane was 0.33% for the partial FI and 0.07% for the full FI (hatched areas). (D) Enforced binding of a FP. The FP N-terminal helix was pulled into the membrane over a period of 1.2 μs, and then released. The FP remained bound to the membrane for all of a 8 μs CG MD simulation. (E) The three FP-CR domains organize into a disordered laterally extended blob at the N-terminal end of the FI backbone, the FI head. Two FP N-terminal helices reside at one end of the head, one at the other end (orange stars). End view (perspective of red arrow) of N-terminal helix beads and their density distribution along the principal axis (dashed black line) in the plane normal to the backbone.

Cryo-ET density is well explained by the simulated fusion intermediate configurations

So far we've simulated the unbounded FI and estimated the binding time, using a highly constrained structure constructed computationally. We recently used cryo-electron tomography (cryo-ET) to visualize the membrane-bound CoV-2 FI that bridges the membranes of virus-like particles (VLPs) and target extracellular vesicles (tEVs) (190). To lock S2 into the transient FI state, we used a lipopeptide [HR2-PEG$_4$]$_2$-chol, which consists of two HR2-derived peptides conjugated by a cholesterol (Fig. 4.7A). The cholesterol is thought to anchor into the tEV membrane and the HR2-derived peptides are thought to bind FI's HR1 to prevent binding of the FI's own HR2 which further blocks FI refolding. These stabilized FIs are highly flexible structures in cryo-ET densities (Fig. 4.7B).

To compare with the experiments we performed CG MARTINI simulations of the FI with its FP bound to the target membrane (Fig. 4.7C). The target membrane is separated from the virus envelope by 15, 20 and 25 nm, consistent with the separation range observed in cryo-ET (190). We first enforced binding by pulling one FP of the FI into the target membrane, using the same procedure as for testing robust membrane binding of the FI (Fig. 4.6D). Then we simulated the membrane-bound FI for 20 μs to generate FI configurations to fit the cryo-ET densities. The FI remained stably bound for all three separations. Although the FPs remained bound, the FI backbone bended over a large range of angles with respect to the target membrane due to the three C-terminal hinges (Fig. 4.7D).

Then we quantitatively examined the similarity of the FI configurations between the cryo-ET experiments and MD simulations. By extracting the cryo-ET density map in 3D, we identified ten membrane-spanning FIs from seven tomograms (Fig. 4.7B). For each of the ten FI densities, we searched for a best matched FI structure sampled in the three 20 μs simulation. First we estimated the end-to-end distance between the TMD and FP anchor points in the two membranes from cryo-ET and found candidate structures with similar distances from simulations. Then we properly rotated these candidates and selected the one maximizing the Pearson correlation between the simulated and experimental density distribution (see Methods). 7/10 of the observed FIs have a good fitting counterpart in the simulations (Pearson correlation > 0.15). Among these examples an elongated tubular volume in cryo-ET (Fig. 4.7B) resembling the HR1-CH backbone (Fig. 4.7A) is always found. Such tubular volume is not necessarily in the xy plane which in turn justifies the necessity of examining the density in 3D. For the remaining three potential FIs, the cryo-ET density map branches in the middle and thus the FI has two connections to the target membrane, indicating an overlap between two FIs. The good match between the experiments and simulations in turn validates our proposed highly constrained FI structure (Fig. 4.1).

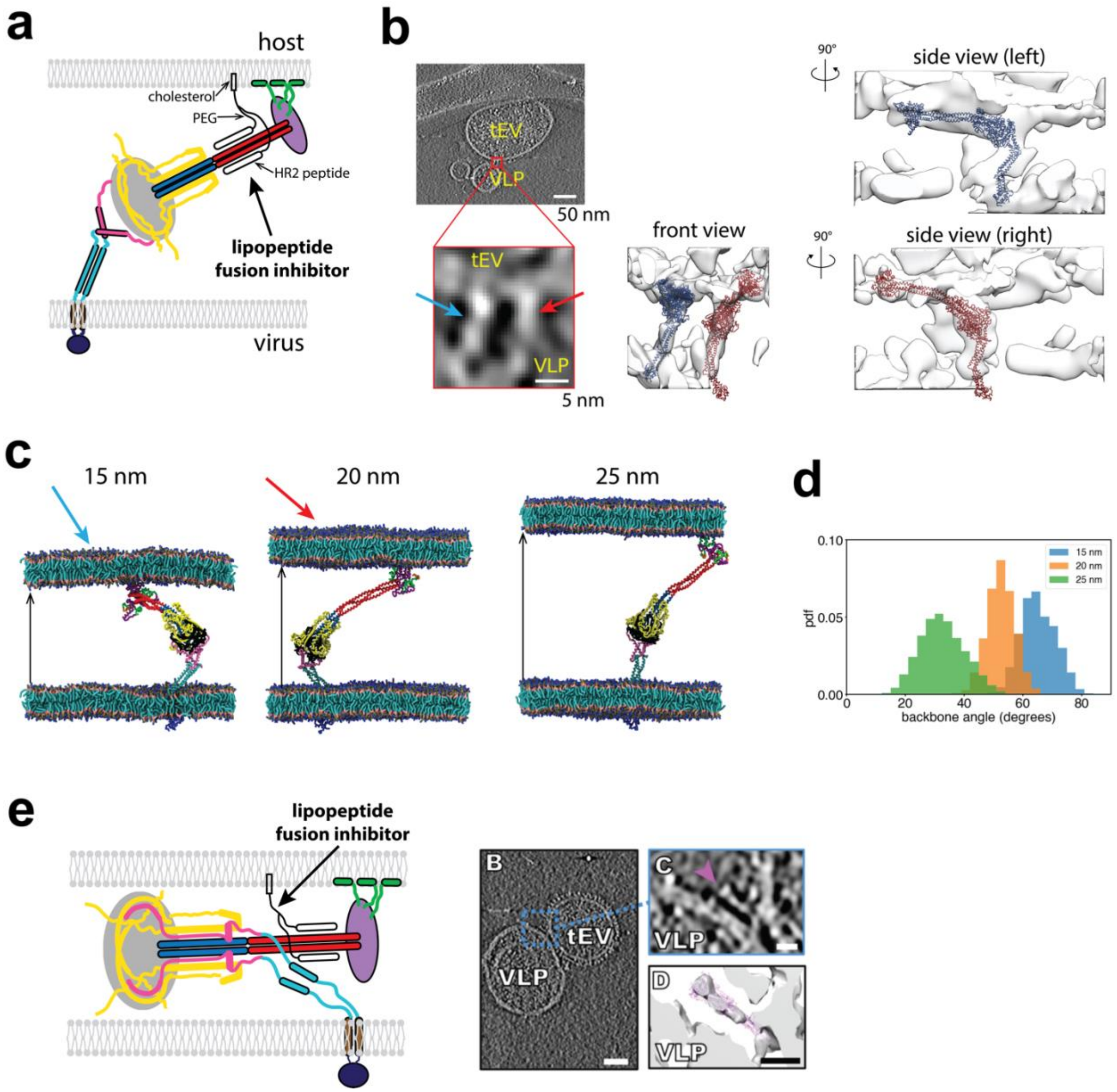
a
host
cholesterol
PEG
HR2 peptide
lipopeptide fusion inhibitor
virus
b
tEV
VLP
50 nm
tEV
VLP
5 nm
front view
90°
side view (left)
90°
side view (right)
c
15 nm
20 nm
25 nm
d
0.10
0.05
0.00
pdf
0
20
40
60
80
backbone angle (degrees)
15 nm
20 nm
25 nm
e
lipopeptide fusion inhibitor
B
tEV
VLP
C
VLP
D
VLP

Figure 4.7. Comparison of the fusion intermediate simulations with cryo-ET density maps.
(A) Schematic of the fusion intermediate stabilized by a lipopeptide inhibitor. The lipopeptide (168) (black) is anchored to the target membrane via its cholesterol. The two HR2-derived peptides of the inhibitor bind to HR1 of the FI (red) so that the FI's HR2 cannot bind to HR1 and the subsequent FI refolding is prevented.
(B) Cryo-ET images (190) showing fusion intermediates spanning the membranes of virus-like particles (VLPs) and target extracellular vesicles (tEVs). The cryo-ET density is replotted using data published in ref. (190) and a tomogram z-slice (left) shows the flexible FIs connecting the membranes (arrows). The 3D density map (middle and right, shown in the isosurface representation) was used to find the best fit structures chosen from simulation snapshots. The FIs span a long distance in the z direction (side views, right).

(C) Snapshots from CG MARTINI simulations of membrane-bound FIs for three membrane separations. The structures used to fit the cryo-ET densities in (b) are shown (arrows).
(D) Distribution of the angle that the FI backbone bends with respective to the target membrane for three membrane separations. (e) Schematic of the refolded intermediate. In the presence of the lipopeptide, the FI can almost fully refold, except that the last HR2 refolding is blocked by the lipopeptide. The refolded intermediate configuration is close to the postfusion state of S2. In cryo-ET images (190) such refolded intermediate was often observed and the density agreed well with the postfusion structure (156) (right).

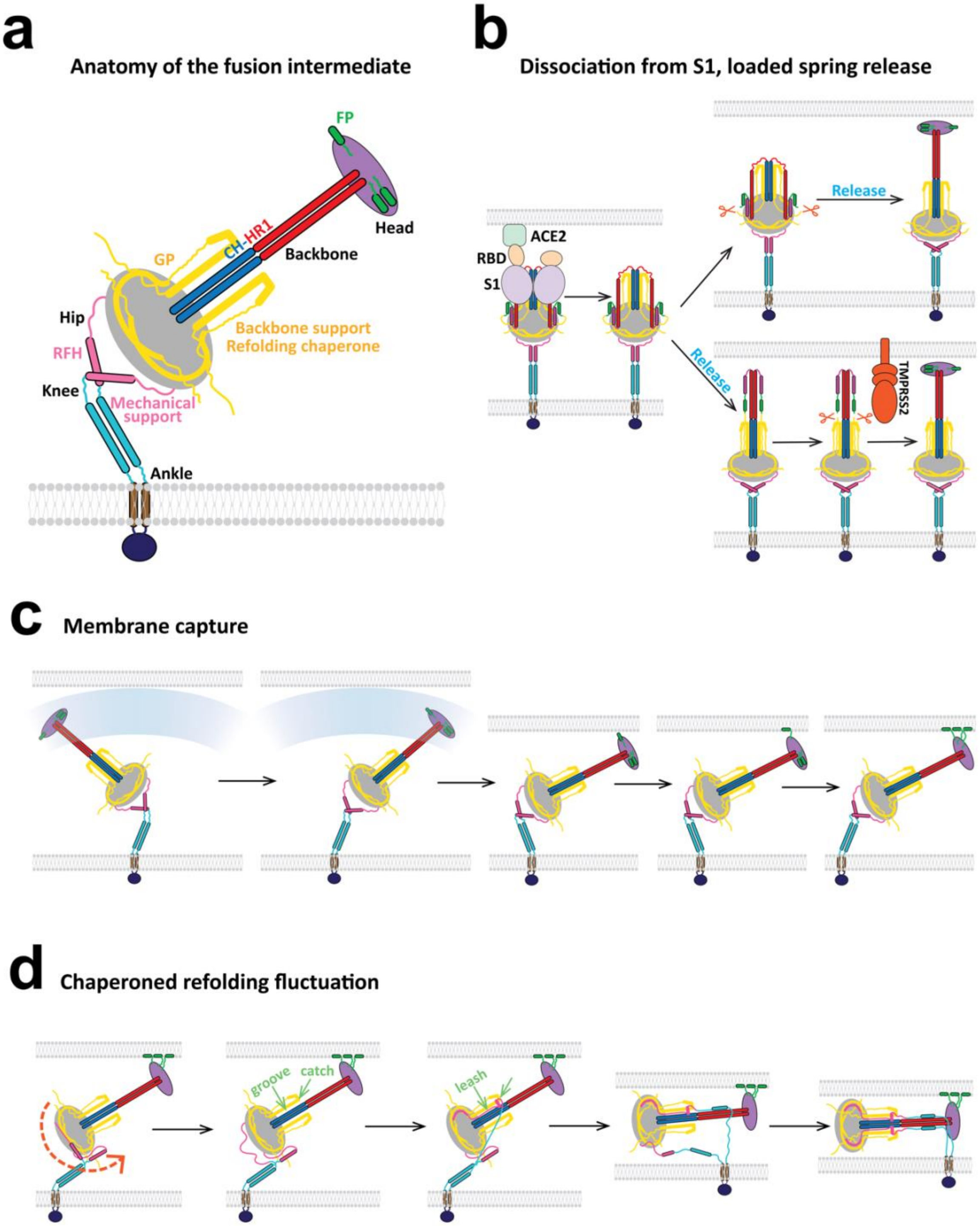
a
Anatomy of the fusion intermediate
FP
Head
CH-HR1
Backbone
GP
Hip
RFH
Knee
Mechanical support
Backbone support
Refolding chaperone
Ankle
b
Dissociation from S1, loaded spring release
ACE2
RBD
S1
Release
Release
TMPRSS2
c
Membrane capture
d
Chaperoned refolding fluctuation
groove
catch
leash

Figure 4.8. Model of the SARS-CoV-2 fusion intermediate and the pathway to fusion. (A) Schematic of the fusion intermediate. The ankle, knee and hip hinges impart high flexibility to the FI. RFH is an inverted tripod suspension system buffering longitudinal backbone fluctuations. GP supports the backbone and chaperones refolding. The CH-HR1 backbone provides mechanical strength and reach. The FP-CR head houses the fusion peptides for host membrane capture. (B) Pathway to the fusion intermediate. Following dissociation of S2 from the S1/ACE2 complex, a loaded spring release mechanism generates the fusion intermediate after proteolytic cleavage at the S2′ site (upper pathway) or before cleavage (lower pathway). RBD, receptor binding domain of S1. TMPRSS2, transmembrane protease serine 2. (C) Schematic of host cell membrane capture by the fusion intermediate. Three base hinges endow the fusion intermediate with high flexibility and large configurational fluctuations, so the N-terminal fusion peptides sweep out a large volume for membrane capture. (D) Model of fluctuation-triggered, GP-chaperoned refolding. A sufficiently large rotational fluctuation at the RFH/BH hip joint unfolds a RFH stem helix into an unstructured loop. The loop is grabbed by a GP $\boldsymbol{\beta}$-strand in BH, initiating RFH refolding, and guided into a GP-CH groove which it packs as a leash. Leash zippering into the groove is stabilized by the GP catch, preventing unzippering. Refolding of the HR2 leash completes refolding of one protomer, pulling the membranes together and helping the other protomers refold. The trans postfusion structure catalyzes membrane fusion in cooperation with other refolded fusion proteins.

4.3 Discussion

The outbreak of Covid-19 saw rapid efforts to characterize the pre- and postfusion SARS-CoV-2 spike protein structures (150, 156, 158, 159), but the structure of the fusion intermediate (FI) that facilitates fusion and entry remains unknown and the pathway to fusion and entry is poorly characterized. The first step on this pathway is capture of the host cell target membrane by the FI, but the mechanism and timescale are unknown for CoV-2 or indeed any coronavirus.

Here we built a full length model of the CoV-2 FI, extrapolating from pre- and postfusion structures (156) (Fig. 4.1A). Our FI model was validated by our cryo-ET data. The cryo-ET densities of the flexible FIs spanning the two membranes were well explained by the simulated FI configurations with huge fluctuations (Fig. 4.7B). From coarse-grained simulations we inferred a FI-mediated membrane capture time of a few ms. Macroscopically this is fast, suggesting that therapeutic strategies targeting the FP are limited by a small ~ ms window during which the FP is exposed, and that targeting the refolding process (159, 168, 191) may be more fruitful. However, a ms timescale is very long from a computational perspective: given our computational resources, membrane capture would require several hundred years of atomistic simulation (see Appendix), and so is observable only with coarse-grained MD methods. These membrane binding rates were overestimated ~ 2 orders of magnitude by simulations with the FP removed from its host fusion protein, although a 10 residue N-terminal helix directing and maintaining FP binding was identified (Fig. 4.5B) in accord with a recent study (176). Simulations of isolated viral fusion peptides are commonly implemented (176-178, 192), but our results suggest they should be interpreted with caution as the fusion peptide environment is radically altered when attached to its host fusion protein.

Atomistic and coarse-grained simulations presented a picture of the FI as a machinery designed to efficiently capture membrane (Fig. 4.8). The FI suffered large bending and tilting fluctuations due to 3 highly flexible hinge regions (Figs. 4.2, 4.3, 4.6), similar to 3 hinges identified in the prefusion structure that were proposed to aid receptor binding (174). We suggest the hinges are most critical to the FI. Large fluctuations may aid capture of host cell membrane by enlarging the region accessible to the FPs at the FI terminal (Fig. 4.7C), and may help to coordinate capture by multiple FIs at different distances. Indeed, influenza, parainfluenza and HIV-1 appear to use several FIs (161, 163, 193). Further, by allowing the ~25 nm long FI to bend significantly, the extreme flexibility may facilitate the prefusion-to-FI transition even in the confined circumstances of a nearby host cell membrane (Fig. 4.6A) and allow the FI to tilt its head and present the FPs directly to the target membrane (Figs. 4.6E, 4.7C). A milder flexibility was observed in the prefusion HA of influenza, which was reported to bend through $\sim 25^0$ mediated by a linker between the ectodomain and TMD (194).

Following binding of the FI to the target membrane on a ms timescale, the next step on the pathway to fusion and cell entry is refolding of the FI that pulls the viral and target membranes together. What sets the timing of refolding? Refolding requires a major structural transition of the RFH domain, which folds into the GP domain and the CH-HR1 backbone (Fig. 4.1A). In AA and CG simulations the RFH domains had a highly dynamic structure, permitting large bending fluctuations of the hip hinge at the RFH/BH interface (Figs. 4.2, 4.6A). This suggests the refolding time may be the waiting time for a rotational hip hinge fluctuation sufficiently large to destabilize one of the splayed RFH helices into an unstructured loop (Fig. 4.8D). The loop would be highly susceptible to GP-chaperoned refolding. FI refolding and the drawing together of the host and viral membranes may be mutually reinforcing elements in a cooperative process, as a smaller membrane separation presumably favors refolding, while refolding decreases the membrane separation.

As the machinery that achieves cell entry, the FI is a natural therapeutic target. A number of candidate drugs have targeted the refolding step. HR2-derived peptides inhibit fusion by SARS-CoV-2 and MERS-CoV, presumably blocking formation of the HR1-HR2 six-helix fusion core (159, 168, 195). Their efficiency as fusion inhibitors is insensitive to mutations in the spike protein (172), suggesting potential as robust antiviral drugs.

Understanding the mechanisms of such candidate drugs and discovery of new FI-targeting drugs will be helped by establishing the structure and dynamics of this elusive intermediate. For example, another potential target is the golden peptide (GP) domain extending from the S1/S2 to the S2′ cleavage site (Fig. 4.1). In addition to its structural role as a stabilizing socket for the CH-HR1 backbone (Fig. 4.8A), GP chaperones RFH refolding (Fig. 4.8D). First, GP helps initiate RFH refolding by providing the β-strand that the RFH N-terminus loop folds onto as a parallel β-strand. Second, GP supplies a groove with the neighboring CH helix into which the RFH leash packs, continuing refolding. Third, a small RFH helix is pinned by the GP catch, a U-shaped sequence including 2 small helices, that may rectify zippering of the RFH leash by preventing its unravelling from the groove. Thus, GP- or RFH-derived peptides could inhibit FI refolding by binding the RFH or GP domains. Such peptides might also stabilize the short-lived unfolded FI for visualization.

Interestingly, a recent study identified an 8-residue region in the prefusion RFH stem helix as the epitope of two cross-reactive monoclonal antibodies (196). This region becomes the small RFH helix that engages the GP catch during refolding, together with the four downstream residues. Thus, the antibodies may neutralize CoV-2 by binding RFH and interfering with the GP catch that rectifies RFH refolding. Our simulations suggest another possibility is that binding of the RFH stem helices in the FI alters their dynamics and lowers the hip hinge flexibility, with possible consequences for membrane capture and/or refolding. This would be similar to the effect of antibodies targeting the linker domain adjacent to the TMD of HA, which reduced the linker flexibility and suppressed orientational fluctuations (194).

Another practical issue of inhibiting FIs is whether the FI is “long-live” enough to allow binding of fusion inhibitors before it refolds. Interestingly, the observed cryo-ET FIs in the presence of HR2-derived lipopeptides suggest the subsequent refolding might be slow. The lipopeptides only block the last step of refolding, the formation of HR1-HR2 six-helix bundle, but do not interfere with the initial refolding which is probably triggered by large fluctuations in the BH/GP base (Fig. 4.8D). Thus, one should expect in the presence of such lipopeptides, the S2 should almost fully refold except for the last bundle, adopting a configuration close to the postfusion state (Fig. 4.7E). Indeed, a subset of the connections spanning the two membranes in cryo-ET resemble the rather refolded, postfusion-like S2 (190) (Fig. 4.7E). Observing these unexpected extended FIs in the presence of HR2-derived peptides suggests that the subsequent refolding of the FI might be the rate-limiting step compared to membrane capture. Measuring the life time of the extended FI would be interesting and important, as fusion inhibitors may have to bind to FI rapidly enough before the FI refolds. Interestingly, the "pioneer" extended intermediate of influenza hemagglutinin, the first hemagglutinin intermediate to bridge the virus and host cell membranes, was suggest to stably exist for a minute as it has to wait for other intermediates to form before the intermediates cooperatively refold and trigger membrane fusion (160). The dependence of membrane fusion rates on the number of CoV-2 spike FIs would be interesting to investigate.

In summary, the extended FI is the fusogenic form of the spike protein that captures host cell membrane for fusion and entry and is a critical but relatively unexplored therapeutic target. Our model suggests a loaded-spring mechanism generates the FI from the prefusion structure, related to the mechanism for HA of influenza (162, 183) . The FI has unexpectedly large bending fluctuations that help it capture membrane in a few ms and may trigger the refolding transition that draws the viral envelope and host membranes together for subsequent fusion (Fig. 4.8). These results provide an account of a critical episode during cell entry and offer a framework for rational design of new therapeutic strategies to disable the FI.

4.4 Appendix: Details of the simulations and the analysis

Building a complete structure for the fusion intermediate of the SARS-CoV-2 spike protein.

The primary sequence of the SARS-CoV-2 S protein was obtained from the NCBI database (GenBank: MN908947). We first built the HR1-RFH portion of the FI (including the associated GP domain). We used Modeller (197) with two specified templates: the postfusion structure (PDB: 6XRA) for HR1-BH and GP, and the prefusion structure (PDB: 6XR8) for RFH. Several constraints including 3-fold symmetry and preservation of secondary structure were specified. The C-terminal domains (HR2, TMD and CT) were then appended to the HR1-RFH portion one by one using Modeller. The source for HR2 was a SARS-CoV HR2 NMR structure (PDB: 2FXP), while the TMD/CT structure was predicted by the QUARK server by providing the primary sequences. The FP and CR were then extracted as a whole from the prefusion structure (PDB: 6XR8) and appended to the HR1 domain in the FI with an arbitrary angle using Pymol. Finally, a complete GP structure was made in the FI using Modeller, by appending the N-terminal portion (residues 686-702) and C-terminal portion (residues 771-815) of the prefusion structure to the solved postfusion GP (residues 703-770).

All-atom simulation of the fusion intermediate.

The full-length fusion intermediate (FI, Fig. 4.1B) with its TMD inserted in the membrane was placed in a simulation box of $16 \times 16 \times 43\ \mathrm{nm}^3$. The membrane-protein system was built using the CHARMM-GUI membrane builder (198), consisting of 786 lipids for the pure DPPC membrane. The termini and ionizable residues were treated in their charged states assuming neutral pH. The disulfide bond in FP was added according to the prefusion structure (PDB: 6XR8), while the disulfide bonds in the other domains, BH and GP, were added based on the postfusion structure (PDB: 6XRA, the disulfide bonds were conserved in the pre- and postfusion structures). The resulting simulation box contained approximately 300,000 water molecules and was neutralized with 150 mM NaCl ions. The TIP3P model was used for water (199).

The system was first energy-minimized for 1,000 steps. Then, 2 equilibrations in the NVT ensemble were each performed for 0.1 ns with position restraints on all protein atoms. Subsequently, 4 equilibrations in the NPT ensembles were each performed for 0.5 ns with position restraints on protein heavy atoms. The production simulation was run for 406 ns in the NPT ensemble at 1 bar and 310 K and with a time step of 2 fs. The temperature and pressure were maintained using the Nose´-Hoover thermostat (200, 201) and Parinello-Rahman barostat (202), respectively. All the energy-minimization, equilibration, and production simulations were performed using GROMACS 2019.6 (203, 204). The secondary structure of each residue in the FI was analyzed using the *dssp* algorithm (205, 206) for every 0.1 ns.

Coarse-grained simulation of a fusion intermediate with uncleaved S2′ sites.

Atomistic coordinates of the full-length fusion intermediate (Fig. 4.1B) were converted onto the MARTINI 2.2 topology using the *martinize* utility and placed in a simulation box of $40 \times 40 \times 50$ nm^3. The unsolved C-terminal part of the GP domain in the postfusion structure (156) (residues 771-815) was forced to be a loop, by changing the input secondary structural file to the *martinize* utility. The terminal and ionizable residues were treated in their charged states assuming neutral pH. The box was then solvated by approximately 600,000 coarse-grained water particles and was neutralized by 150 mM NaCl ions.

In each protomer, the FP N-terminus residue (residue 816) and the GP C-terminus residue (residue 815) were pulled together at a constant rate of 10 nm/μs by a harmonic potential with a force constant of 500 kJ mol^{-1} nm^{-2}. Position constrains by a harmonic potential with force constant of $1{,}000$ kJ mol^{-1} nm^{-2} were applied to the beads in the domains other than GP, FP and CR. The pulling simulation took ~1.5 μs so that in the final configuration, the COG distance between residues 815 and 816 in one of the three protomers reaches ~0.5 nm.

The final coordinates of the coarse-grained FI were then backmapped into atomistic resolution in CHARMM36 force field (207, 208). The residues 815 and 816 were covalently connected in the protomer with the smallest separation between the two residues, and this protomer was duplicated twice to make a trimer using Pymol. Now a structure of the FI with its S2′ sites uncleaved was created. Then, the all-atom structure of the FI with its S2′ sites uncleaved was converted into MARTINI coarse-grained representation using the *martinize* utility. A simulation box of $30 \times 30 \times 50\ \mathrm{nm}^3$ was generated using the *insane* utility, in which the coarse-grained FI with its S2′ sites uncleaved was inserted in a crystalline DPPC bilayer consisting of 2,831 coarse-grained lipids that represented the viral envelope.

The system containing the coarse-grained FI with its S2′ sites uncleaved on the viral envelope was first energy-minimized for 2,000 steps in the vacuum. Subsequently, the box was solvated with approximately 300,000 coarse-grained water particles and neutralized with 150 mM NaCl ions. The system was then energy-minimized for 2,000 steps and equilibrated for 4 ns in NPT ensemble sampling. Then the system was subjected to a production simulation lasting 4 μs in the NPT ensemble. The system temperature, membrane tension, and system pressure were maintained at the same value using the same thermostat and barostat as mentioned above.

Coarse-grained simulations of the fusion intermediate.

Atomistic coordinates of the modeled full length fusion intermediate (Fig. 4.2A) were converted onto the secondary structure based coarse-grained MARTINI 2.2 topology (209, 210) using the *martinize* utility. The termini and ionizable residues were treated in their charged states assuming neutral pH. Disulfide bonds were added to the same residues as in the all-atom simulation. The simulation box of $30 \times 30 \times 50\ \mathrm{nm}^3$ was generated using the *insane* utility (211), in which the coarse-grained (CG) FI with its TMD inserted in a crystalline DPPC bilayer consisting of 3,024 coarse-grained lipids that represents the viral envelope.

The system was first energy-minimized for 2,000 steps in vacuum. Subsequently, the box was solvated with approximately 300,000 coarse-grained water particles and neutralized with 150 mM NaCl ions. The system was then energy-minimized for 2,000 steps and equilibrated for 4 ns in NPT ensemble sampling. Then the system was subjected to 5 independent production simulations, each lasting 8 μs in the NPT ensemble. Equations of motion were integrated using the Verlet leapfrog algorithm with a 80 fs time step. Bonds were constrained with the LINCS algorithm. The system temperature (310K) was maintained by the velocity rescale thermostat (212). The membrane tension (0.05 pN/nm) and the system pressure (1 bar) were maintained by the Berendsen barostat with surface-tension coupling (213).

Fitting a curve to the fusion intermediate ectodomain

To fit a curve to represent the FI ectodomain backbone (residues 912-1237) in the MARTINI simulations of the FI (Figs. 4.3 and S4.2), we first represented the backbone by points. Each point represented a residue and its position was calculated by the averaged position of the MARTINI backbone bead (the non-sidechain bead) of each residue among the three protomers. The coordinates of the beads were extracted from the simulation trajectory using the *mdtraj* (214) python package. Then the FI backbone was divided into an upper part (residues 912-1191) and a lower part (1152-1237) with an overlapping region of 40 residues. Each part was separately smoothed by the following steps. (1) All points $(x_\mathrm{i}, y_\mathrm{i}, z_\mathrm{i})$ were calibrated so that the center of gravity (COG) was at the origin, (2) All points were rotated so that the new x,y,z axis are aligned with the eigenvectors of the gyration tensor of the rotated points $(x'_\mathrm{i}, y'_\mathrm{i}, z'_\mathrm{i})$. This rotation maximized the root mean square projected length onto the z axis. (3) A smoothed curve $(\overline{x_i'}, \overline{y_i'}, z_i')$ was generated by the LOWESS algorithm in python, in which the smoothed $\overline{x_i'}$ and $\overline{y_i'}$ value for each z_i' was set by its neighboring points spanning one tenth of the entire z range. Then the smoothed upper/lower part was rotated back to the original orientation and the overlapping region was averaged between the upper/lower parts. Finally the reconnected points were smoothed by the B-spline method with 4th order polynomial functions. To find the location (from the N- to the C-terminus) of each domain on the fitted the curve, the curve was first reparametrized by its normalized arclength. The location of each residue was determined as the normalized arclength of the nearest point on the fitted curve to the position of this residue averaged over the three protomers, using only the backbone bead to locate the residues.

The isolated fusion peptide binding assay.

The atomistic structure of the fusion peptide (FP, residue 816-855) was extracted from the crystal structure of the prefusion structure (PDB: 6XR8). Then the atomistic structure of the FP was coarse-grained into the MARTINI representation. The ionizable residues were treated in their charged states assuming neutral pH. The C-terminal carboxyl group at residue 855 was neutralized by changing the type of the backbone bead from Qa to Na and changing the backbone bead charge from -1 to 0 in the itp topology file, as the residue 855 connects CR in the full-length FI. The disulfide bond was added according to the solved prefusion structure (PDB: 6XR8). The coarse-grained FP was placed approximately 1 nm above a crystalline DPPC bilayer consisting of 162 coarse-grained lipids in a $7 \times 7 \times 10\ \text{nm}^3$ box using the *insane* utility(211). By implementing periodic boundary condition, this is equivalent to placing a FP between two planar membranes separated by ~5.5 nm.The system was first energy-minimized for 500 steps in vacuum. Subsequently, the box was solvated with approximately 2,000 coarse-grained water particles and neutralized with 150 mM NaCl ions. The system was then energy-minimized for 500 steps and equilibrated for 4 ns in the NPT ensemble with a 80 fs time step. Then the system was subjected to 10 independent production simulations, each lasting 24 μs in the NPT ensemble. The system temperature (310K) was maintained by the velocity rescale thermostat (212). The membrane tension (0.05 pN/nm) and the system pressure (1 bar) were maintained by the Berendsen barostat with surface-tension coupling (213). A binding event was defined to be when the z coordinate of the FP COG first had a value that positioned it below the upper membrane leaflet and above the lower membrane leaflet, where the leaflet locations were defined as the average locations of the PO4 beads in each leaflet.

All-atom simulation of a membrane-bound fusion peptide.

In one of the CG simulations in the FP-only binding assay, the final configuration of the FP and the membrane to which it was bound is converted to atomic resolution in CHARMM36 force field (207, 208) using the *backward* utility (215). The ionizable residues are treated in their charged states assuming neutral pH. The C-terminal carboxyl group is neutralized. The Disulfide bond is added to the same residues as in the FP-only binding assay. The resulting simulation box contained approximately 9,000 water molecules and was neutralized with 150 mM NaCl ions. The TIP3P model was used for water (199).

4 equilibrations in the NVT and NPT ensembles were each performed for 50 ns with position restraints on peptide heavy atoms. The production simulation was run for 2 μs in NPT ensembles at 1 bar and 310 K and with a time step of 2 fs. The temperature and pressure were maintained using the Nose´-Hoover thermostat (200, 201) and Parinello-Rahman barostat with isotropic coupling (202), respectively. The secondary structure of each residue in the FP was analyzed using the *dssp* algorithm (205, 206) for every 0.1 ns. The membrane insertion depth of

each FP residue was defined as the vertical distance between the residue COG and the COG of PO_4 groups in the membrane leaflet to which the FP was bound.

Coarse-grained simulations of an equilibrated fusion peptide bound to a membrane.

In the AA simulation of a membrane-bounded FP simulation, the final configuration of the FP and the membrane to which it was bound was converted to MARTINI CG representation using the *martinize* utility. The ionizable residues were treated in their charged state. The C-terminal carboxyl group was neutralized.

The system was first energy-minimized for 1,000 steps in the vacuum. Subsequently, the box was solvated with water particles and ions to attain a salt concentration of 0.15 M. The system was then energy-minimized for 5,000 steps and equilibrated for 0.8 ns in the NPT ensemble. Then the system was subjected to the production simulation for 80 μs in the NPT ensemble. The system temperature (310K) and pressure (1 bar) were maintained by the velocity rescale thermostat and Parinello-Rahman barostat, respectively.

The membrane insertion depth of each residue was defined in the same way as for the AA simulation (see above). The gyration tensor M of the FP was defined as

$$M = \frac{1}{N}\sum_{\mathrm{i}=1}^{N} (r_{\mathrm{i}} - r_{\mathrm{c}}) \otimes (r_{\mathrm{i}} - r_{\mathrm{c}}), \quad [S4.1]$$

where $\otimes$ represents the dyadic product, r_{i} is the coordinate of the *i*th bead in the FP, N is the total number of beads, and $\mathrm{r_c}$ is the COG of the FP, as $\mathrm{r_c} = \sum_{i=1}^{N} \mathrm{r}_i / N$. The radius of gyration R_{g} was computed as the square root of the trace of M. The length and the width of the FP were defined as, respectively, greater and smaller of the eigenvalues of M projected onto the x-y plane, and the thickness was defined as $\sqrt{M_{\mathrm{zz}}}$.

Coarse-grained simulations of the fusion intermediate interacting with a target membrane.

For ten of the simulations of the FI interacting with a target membrane, ten snapshots from three FI simulations (one membrane) were chosen as the initial condition in which the FI ectodomain protruded ~20 nm normal to the membrane. Another pre-equilibrated planar membrane (run for 4 µs) was placed 20 nm above the membrane anchoring the FI in the selected configurations. Each configuration containing an FI and two membranes was re-solvated by approximately 200,000 coarse-grained water particles and neutralized by 150 mM NaCl ions. Then, each of the 10 systems was equilibrated for 4 ns, and subject to a production simulation for 8 µs in the NPT ensemble. The system temperature (310K) was maintained by the velocity rescale thermostat. The membrane tension (0.05 pN/nm) of the two membranes and the system pressure (1 bar) was maintained by the Berendsen barostat with surface-tension coupling.

In an additional set of simulations, all ten runs started from a biased initial condition, in which the COG of the nearest N-terminal FP helix was within 1 nm of the adjacent membrane and the FI head was in the (1,2) configuration. Here, the membrane position was defined to be the mean location of all the PO4 beads in the lower leaflet of the upper membrane. Each production simulation lasted 22.4 µs with the same system temperature, pressure and the membrane tension.

Coarse-grained simulations of membrane binding by the partial fusion intermediate.

The structure of the HR1, CR and FP domains in the MARTINI CG representation was extracted from the final configuration of a simulation of the FI interacting with a target membrane. The ionizable residues were treated in their charged states assuming neutral pH. The

C-terminal carboxyl group at residue 984 was neutralized by changing the type of the backbone bead from Qa to Na and changing the backbone bead charge from -1 to 0 in the itp topology file, as the residue 984 connects CH in the full-length FI. This partial FI was positioned above ~ 0.5 nm above a crystalline DPPC bilayer consisting of 676 coarse-grained lipids in a 20 × 20 × 13 nm^3 box with periodic boundary conditions, equivalent to two planar membranes separated by ~8.3 nm.

The system was first energy-minimized for 500 steps in vacuum. Subsequently, the box was solvated with approximately 26,000 coarse-grained water particles and neutralized with 150 mM NaCl ions. The system was then energy-minimized for 2,000 steps and equilibrated for 4 ns in the NPT ensemble with a 80 fs time step. Then the system was subjected to 6 independent production simulations, each lasting 160 μs in the NPT ensemble. The system temperature (310K) was maintained by the velocity rescale thermostat (212). The membrane tension (0.05 pN/nm) and the system pressure (1 bar) were maintained by the Berendsen barostat with surface-tension coupling (213).

The exact time for a binding event was defined to be when the vertical distance between the FP N-terminal helix COG and the membrane first had a value smaller than the averaged FP-membrane distance when the partial FI was stably bound. The membrane locations were defined as the average locations of the PO4 beads in leaflet to which the partial FI was bound.

To infer the averaged binding time τ of a partial FI, we assumed that at time t the unbound probability P follows an exponential function $P = \exp{(-t/\tau)}$. Given that at the end of the six simulations $t = 160\ \mu s$ the unbound probability is $4/6$, we estimated $\tau = 390 \pm 280$ μs, where the uncertainty of the estimation is obtained using from error propagation.

Pulling the fusion peptide into the target membrane.

An initial condition was chosen with the nearest N-terminal FP helix lying within 1 nm of the membrane and with the FI head in the (1,2) configuration. The FP N-terminal helix was pulled vertically towards the upper membrane at a constant rate of 2.5 nm/μs by a harmonic potential with a force constant of $1{,}000\ \mathrm{kJ\ mol^{-1}\ nm^{-2}}$. The system temperature, membrane tension, and system pressure were maintained at the same value using the same thermostat and barostat as mentioned above. The pulling process took ~1.2 μs. In the final configuration the distance between the COG of the FP N-terminal helix and the COG of the entire upper membrane reached ~0.1 nm, and the FP N-terminal helix was pulled into the adjacent membrane patch by ~1 nm. Then the force was released and a subsequent 8 μs CG simulation was run, in which the system temperature, membrane tension, and system pressure were maintained at the same value using the same thermostat and barostat.

Fitting simulated structures to cryo-ET density map.

The raw cryo-ET data was processed and visualized in ImageJ. The data was first smoothed by a Gaussian filter of radius $2d$, where $d = 0.6484$ nm is the cryo-ET voxel size, and then the image contrast was enhanced by 0.3%. The isosurface representations of the cryo-ET data were made in Chimera, from which we found ten potential FIs connecting the membranes of VLPs and tEVs. For each of the ten FIs, the end-to-end distance between the two membrane-anchor points were calculated. For the three 20-μs CG MARTINI simulations, the FI was equilibrated for 1 μs and the FI configurations were extracted every 10 ns from subsequent trajectories of 19 μs. Among these FI configurations a subset with the FI end-to-end distance close to the experimental values was selected as simulation candidates to fit the cryo-ET density. For each of the FI candidate configurations, a simulated cryo-ET density was generated, by summing up Gaussian point spread functions whose centers are the backbone bead positions of all residues and whose widths are

$d, d, 3d$ in the x, y, z direction, respectively, of the experimental cryo-ET density map. The large width in the z direction, $3d$, accounts for the missing wedge effects. Then the position and the rotation angles of the FI simulation candidate were optimized to maximize the Pearson correlation between the simulated and experimental density map. Such optimization was repeated for each simulation FI candidate, and the simulation candidate with the highest Pearson correlation was chosen as the best fit structure.

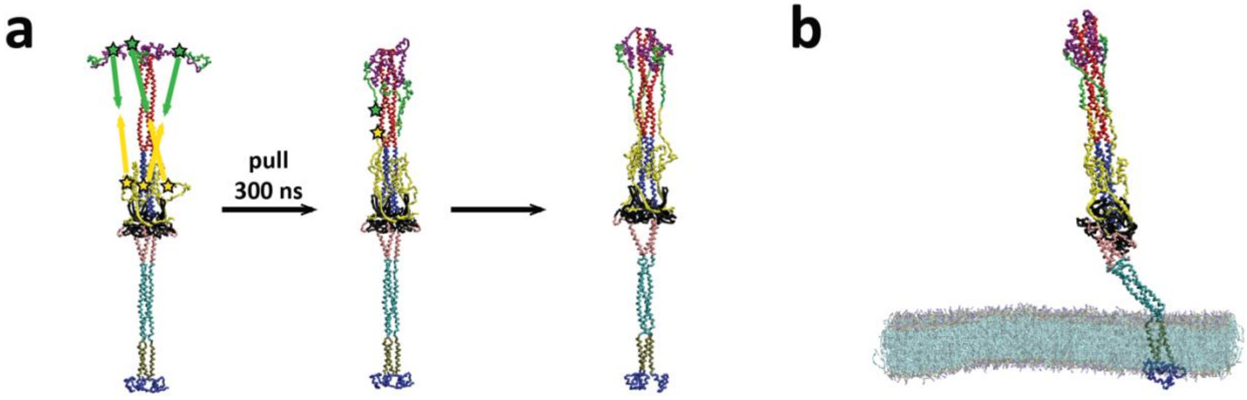

Figure S4.1. Simulation of the fusion intermediate with uncleaved S2′ sites.
(A) Construction procedure for a fusion intermediate with uncleaved S2′ sites. Starting from the model structure in Fig. 4.2B, the C-terminus of three GPs and the N-terminus of three FPs were pulled together in ~1.5 μs in a MARTINI CG simulation. Then the C-terminus of GP and the N-terminus of FP in one protomer were connected covalently (stars). This protomer was duplicated twice to generate a FI homotrimer with uncleaved S2′ sites. (B) Snapshot from a 4 μs simulation. The fusion peptides (green) are sequestered. The FI with uncleaved S2′ sites exhibits similar flexibility to the normally cleaved FI.

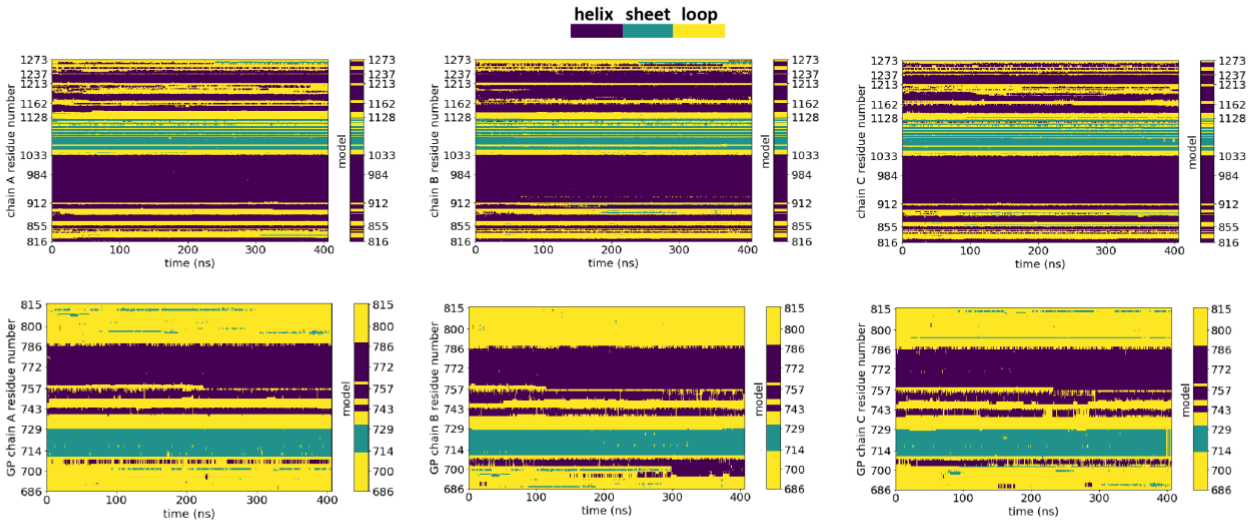

Figure S4.2. Evolution of the secondary structure of the fusion intermediate during 406 ns of all-atom simulation.

The secondary structure of each residue was measured every 0.1 ns during the AA simulation (Fig. 4.2). Each panel refers to one protomer of either the main body of the S2 subunit (top row) or the cleaved GP (bottom row). The secondary structure of the fusion intermediate model of Fig. 4.1B is shown to the right of each panel for comparison.

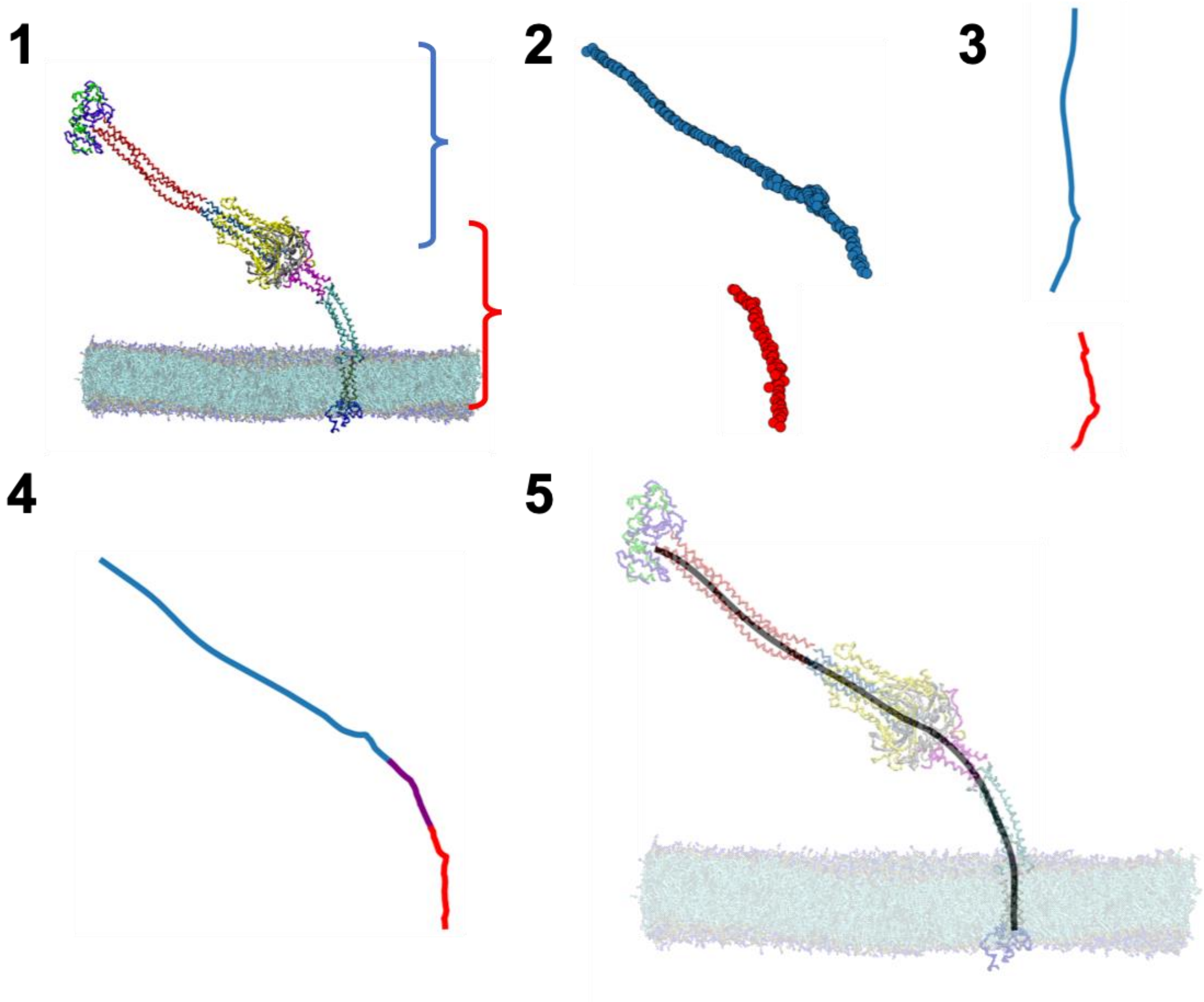

Figure S4.3. Fitting a curve to represent the fusion intermediate ectodomain.
(1) The coordinate of each coarse-grained bead is extracted by Python package *mdtraj*. (2) Each residue is represented by one point, averaged over three protomers. The upper part of the FI (blue, residues 912-1191) and the lower part (red, residues 1152-1237) are separated. (3) The upper and the lower parts are rotated so that the three principal axes are aligned with three eigenvectors of the gyration tensor of the rotated points. The rotated points are smoothed by the LOWESS algorithm. (4) The upper and lower parts are rotated back to their original orientations and reconnected. The overlapping region (purple, residues 1152-1191) is averaged over the upper and lower parts. (5) The final curve is fitted by the B-spline method.

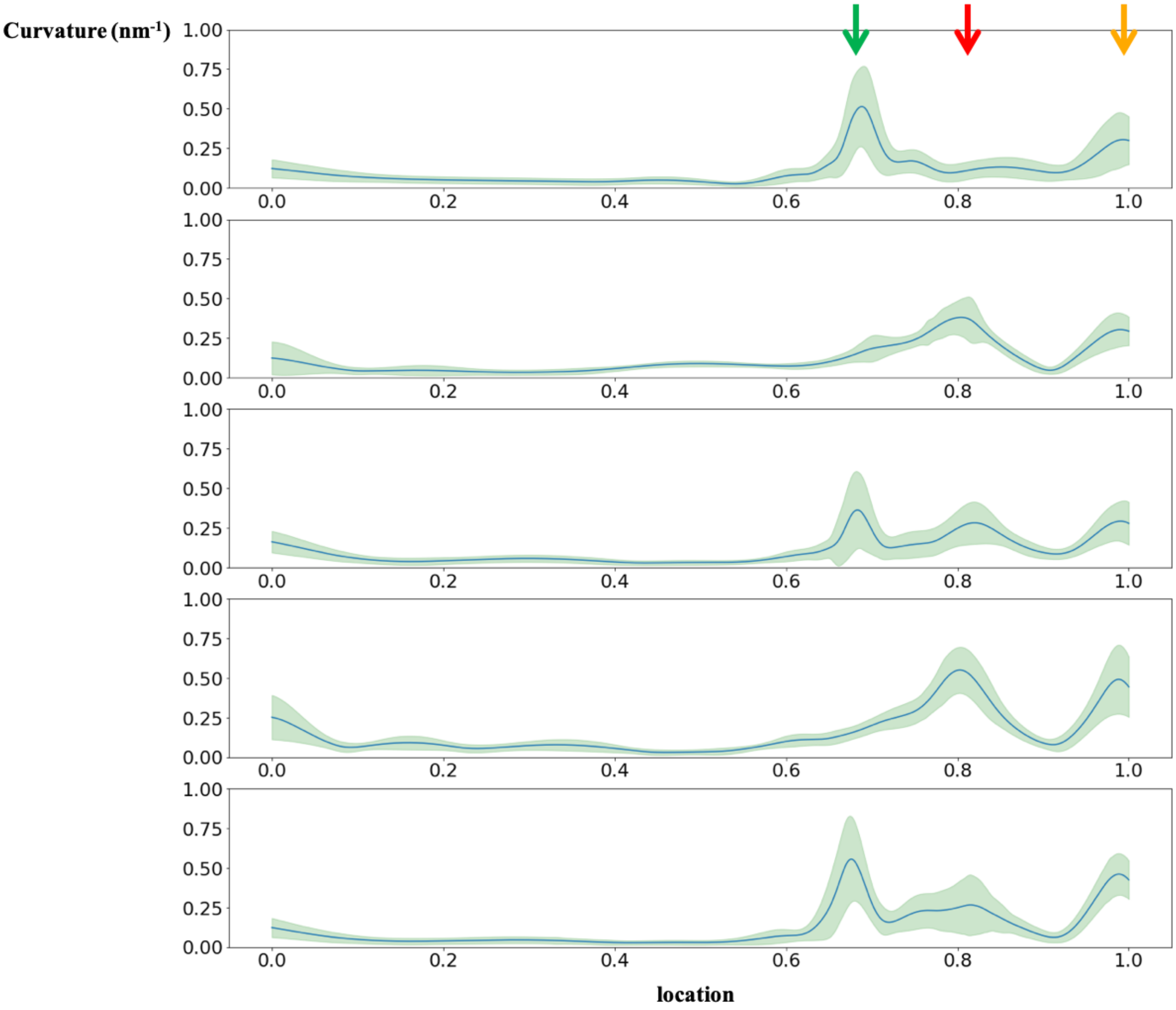

Figure S4.4. Time averaged backbone curvature versus normalized backbone arclength for five parallel runs.
The three hinges (Fig. 4.3B, arrows) show different magnitudes of curvature in the five parallel runs. Green envelope indicates SD.

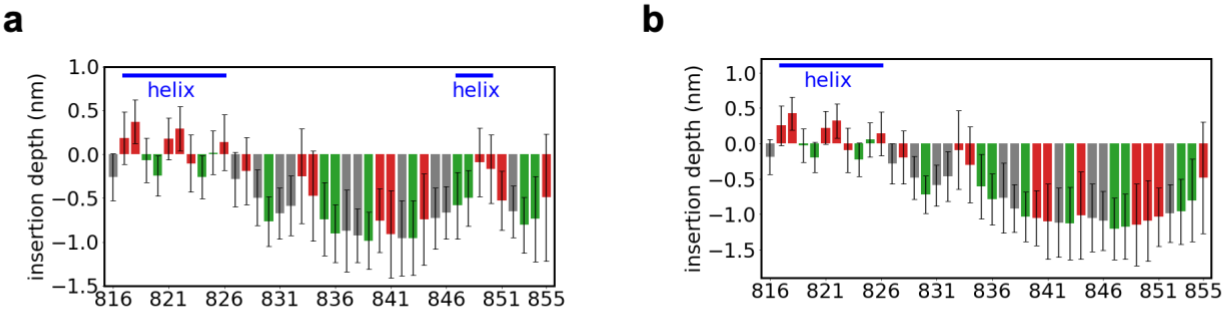

Figure S4.5. Fusion peptide residue insertion depth measured in MARTINI coarse-grained simulations.

The insertion depth is defined as the vertical distance between the center of gravity (COG) of each fusion peptide residue and the COG of the PO_4 beads in the leaflet to which the fusion peptide is bound (same definition as for the all-atom simulation). The secondary structure used is (A) the equilibrated secondary structure from the all-atom simulation, and (B) the equilibrated secondary structure but imposing the C-terminal helix to be a loop. The insertion depths are averaged over the last 78 µs. Error bars: SD over the same time frame. Bars were colored by the hydrophobicity of the corresponding residues (red: hydrophobic, grey: neutral, blue: hydrophilic), using the same color scheme as in Fig. 4.4B.

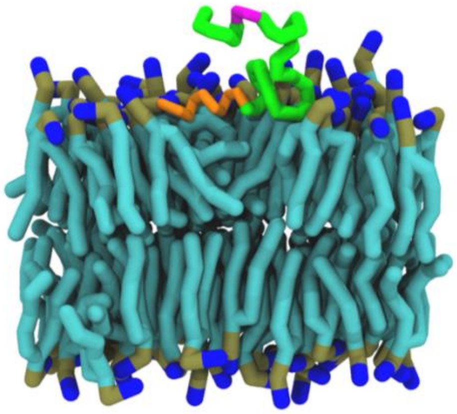

Figure S4.6. MARTINI simulation snapshot showing a transient detachment of the fusion peptide C-terminal helix.

The fusion peptide C-terminal helix (purple) unanchored transiently from the membrane for ~0.3 µs (the instance depicted here occurred after ~52 µs of the simulation). In contrast, the N-terminal helix (orange) always remained buried in the membrane.

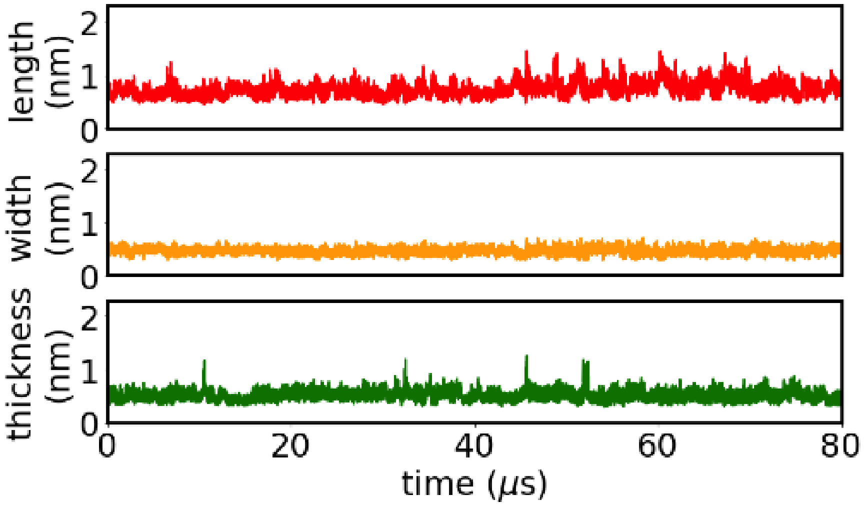

Figure S4.7. Measured length, width and thickness versus time of the fusion peptide during the MARTINI coarse-grained simulation of an equilibrated fusion peptide bound to a membrane.

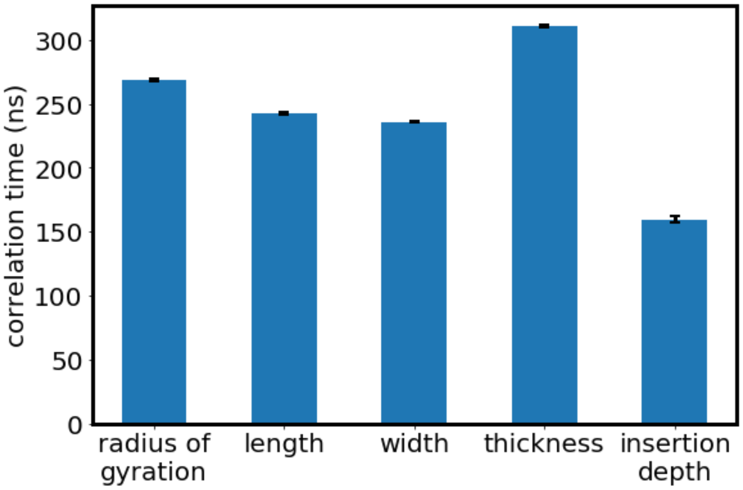

Figure S4.8. Correlation times of the fusion peptide shape properties during MARTINI coarse-grained simulation of an equilibrated fusion peptide bound to a membrane. The radius of gyration, length, width, thickness and insertion depth of the fusion peptide are calculated for the last 78 μs of the MARTINI simulation. The radius of gyration, length, width and thickness are calculated from the gyration tensor (see Appendix). The insertion depth of the entire fusion peptide is defined as the vertical distance between the center of gravity of the fusion peptide and the center of gravity of the PO_4 beads in the leaflet to which the FP is bound. The correlation time is calculated in the same way as in Fig. 4.4G. Error bars: 95% confidence interval.

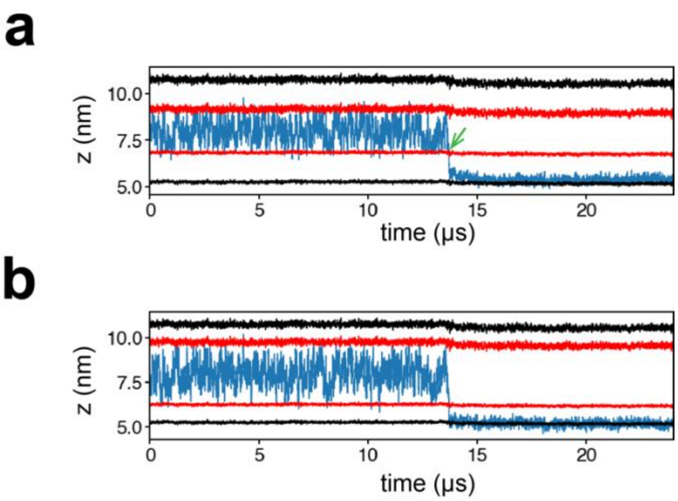

Figure S4.9. Evolution of fusion peptide vertical position during a binding assay of an isolated fusion peptide.

(A) Evolution of the center of gravity of the fusion peptide (blue). The vertical positions of the two leaflets to which the FP is likely to bind are calculated by averaging the PO_4 bead positions in each leaflet (black). A collision event is defined as an approach to the membrane to within $R_{\mathrm{FP}} \sim 1.6$ nm of either leaflet (black), where R_{FP} is the rms FP end-to-end distance. A binding event is defined to be when the FP center of gravity first has a value that positioned it below the upper membrane leaflet and above the lower membrane leaflet (green arrow). (B) Evolution of the center of gravity of the fusion peptide N-terminal helix (blue). The positions of the two leaflets are defined in the same way as for (A). Before the binding event, the N-terminal helix approached several times to within 1 nm of either leaflet (red).

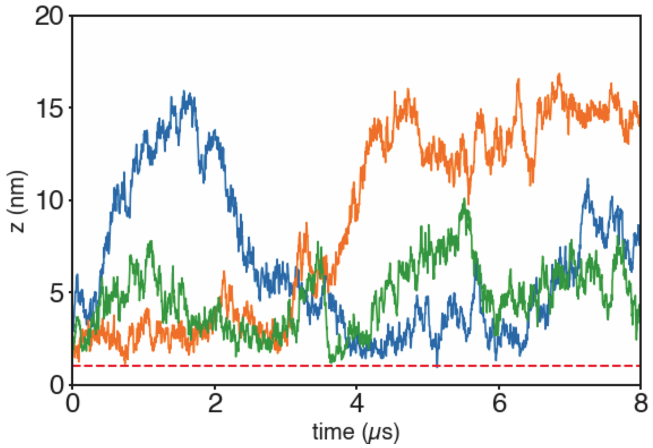

Figure S4.10. Distance of the nearest FP N-terminal helix from the membrane versus time in three runs.

Here the position of the nearest FP N-terminal helix was defined to be its COG location. The membrane position was defined to be the mean location of all the PO4 beads in the lower leaflet of the upper membrane.

Conclusion

In this thesis I made significant progress in understanding how exocytosis is regulated by biophysical forces on the vesicle and cell level. I used a combination of mathematical modeling and statistical analysis to demonstrate (i) osmotic pressure and membrane tension drives vesicle merging into the plasma membrane, (ii) fusion pore expansion requires surmounting a tension-dependent energy barrier set by three families of fusion pore solutions, and (iii) membrane reservoir regulates exocytosis rates via release site availability. Our model and analysis are highly motivated and constrained by experiments including recent breakthrough from the Wu lab. In a related project I used molecular dynamics simulations to demonstrate (iv) fusion intermediate of SARS-CoV-2 spike protein uses its structural flexibility to capture the host cell membrane in milliseconds.

i. Osmotic pressure and membrane tension drives vesicle merging into the plasma membrane

Recent super-resolution microscopy experiments in chromaffin cells revealed that fused dense-core vesicles shrink into the plasma membrane (PM) in a self-similar fashion while retaining their Ω-shaped profile of the membrane composite ("Ω-shrink") (12, 13). However, what drives Ω-shrink has not been understood. In Chapter 1, we mathematically modeled the evolution of a dense-core vesicle fused to the chromaffin cell PM, accounting for membrane bending energies and tension, osmotic forces and membrane-cytoskeleton adhesion. A novel mechanism emerged from the model, quantitatively explaining the experiments. Compressive osmotic pressure on the vesicle is instantaneously established following fusion, and this osmotic squeezing deflates the vesicle and abolishes its membrane tension. The high PM tension then reels membrane from the vesicle onto the cytoskeleton with no resistance. Interestingly, the model predicted vesicles adopt vertically elongated tubular shapes for larger vesicles or higher osmotic pressure, a vivid manifestation of the novel osmotic squeezing mechanism. In agreement with the model, the Wu lab identified such remarkable tubular shapes using super-resolution STED imaging. By comparing the predicted vesicle shapes with electron microscopy measurements, we suggest the vesicles in chromaffin cells were subject to squeezing pressures from ~40 to ~400 Pa.

ii. Fusion pore expansion requires surmounting a tension-dependent energy barrier set by three families of fusion pore solutions

Amperometric traces suggest fusion pores are initially small and may subsequently dilate for full contents release. However, exact fusion pore shapes and energies along the dilation pathway have not been available. In Chapter 2 using formalisms of differential geometry, we obtained exact solutions for fusion pores between two membranes accounting for membrane tension and bending energy constraints. We found three families: a narrow pore, a wide pore and an intermediate tether-like pore. For high tensions these are close to the catenoidal and tether solutions recently reported for freely hinged membrane boundaries. We suggest membrane fusion initially generates a stable narrow pore, and the dilation pathway is a transition to the stable wide pore family. The unstable intermediate pore is the transition state that sets the energy barrier for this dilation pathway. For ~ 400 nm dense core vesicles in chromaffin cells, we estimated the barrier is ~30 kT, depending on membrane tension and separation. Pore dilation is mechanosensitive, as the energy barrier is lowered by increased membrane tension. For sufficiently low membrane tension, pore dilation becomes impossible as the wide pore family disappears. In nanodisc-based experiments where individual fusion pores were studied, we showed that nanodiscs stabilize fusion pores by locking them into the narrow pore family.

iii. Membrane reservoir regulates exocytosis rates via release site availability

Release site availability is thought to regulate exocytosis rates and in endocrine cells exocytosis can happen at hotspots where release sites are repeatedly used. However, how release site availability is regulated and how hotspots regulate exocytosis is not known. In chapter 3 we analyzed spatiotemporal profile of exocytosis events in chromaffin cells observed by confocal microscopy, and discovered a novel mechanism of exocytosis regulation via release site availability. Vesicle fusion can happen repeatedly at hotspots, which generated a membrane reservoir consisting of unmerged and slowly merged vesicles that are spatially close to hotspots. This reservoir accounts for ~20% of the total membrane area added by exocytosis and reaches the steady state in ~20-60 s. In turn, unmerged vesicles in the reservoir occupy release sites and locally suppress exocytosis frequency. We developed a mathematical model to demonstrate that such membrane reservoir requires sufficiently low local membrane tension that abolishes the driving force of vesicle merger.

iv. Fusion intermediate of SARS-CoV-2 spike protein uses its structural flexibility to capture the host cell membrane in milliseconds

Cell entry by SARS-CoV-2 requires the prefusion S2 subunit of the spike S protein to transit to its potent, fusogenic form, the fusion intermediate (FI). However, the FI structure is unknown and the mechanisms and timing of membrane capture and fusion are not established. In chapter 4, we computationally constructed a full-length model of the CoV-2 FI by extrapolating from known CoV-2 pre- and postfusion structures. In atomistic and coarse-grained molecular dynamics simulations the FI was remarkably flexible and executed large bending and extensional fluctuations due to three hinges in the C-terminal base. Simulations suggested a host cell membrane capture time of ~ 2 ms. Isolated fusion peptide simulations identified an N-terminal helix that directed and maintained binding to the membrane but grossly underestimated the binding time, showing that the fusion peptide environment is radically altered when attached to its host fusion protein. The large configurational fluctuations of the FI generated a substantial exploration volume that aided capture of the target membrane, and may set the waiting time for fluctuation-triggered refolding of the FI that draws the viral envelope and host cell membrane together for fusion.

References

1. L. Qu, Y. Akbergenova, Y. Hu, T. Schikorski, Synapse-to-synapse variation in mean synaptic vesicle size and its relationship with synaptic morphology and function. *J Comp Neurol* **514**, 343-352 (2009).

2. A. Albillos *et al.*, The exocytotic event in chromaffin cells revealed by patch amperometry. *Nature* **389**, 509-512 (1997).

3. R. D. Vale, B. J. Schnapp, T. S. Reese, M. P. Sheetz, Movement of organelles along filaments dissociated from the axoplasm of the squid giant axon. *Cell* **40**, 449-454 (1985).

4. J. L. Ross, M. Y. Ali, D. M. Warshaw, Cargo transport: molecular motors navigate a complex cytoskeleton. *Curr Opin Cell Biol* **20**, 41-47 (2008).

5. R. Jahn, D. Fasshauer, Molecular machines governing exocytosis of synaptic vesicles. *Nature* **490**, 201-207 (2012).

6. T. C. Sudhof, The Molecular Machinery of Neurotransmitter Release (Nobel Lecture). *Angewandte Chemie-International Edition* **53**, 12696-12717 (2014).

7. T. C. Sudhof, The molecular machinery of neurotransmitter release (Nobel lecture). *Angew Chem Int Ed Engl* **53**, 12696-12717 (2014).

8. J. E. Rothman, The principle of membrane fusion in the cell (Nobel lecture). *Angew Chem Int Ed Engl* **53**, 12676-12694 (2014).

9. H. Mostafavi *et al.*, Entropic forces drive self-organization and membrane fusion by SNARE proteins. *Proc Natl Acad Sci U S A* **114**, 5455-5460 (2017).

10. A. Gucek *et al.*, Fusion pore regulation by cAMP/Epac2 controls cargo release during insulin exocytosis. *Elife* **8**, e41711 (2019).

11. R. G. Staal, E. V. Mosharov, D. Sulzer, Dopamine neurons release transmitter via a flickering fusion pore. *Nat Neurosci* **7**, 341-346 (2004).

12. H. C. Chiang *et al.*, Post-fusion structural changes and their roles in exocytosis and endocytosis of dense-core vesicles. *Nat Commun* **5**, 3356 (2014).

13. W. Shin *et al.*, Visualization of Membrane Pore in Live Cells Reveals a Dynamic-Pore Theory Governing Fusion and Endocytosis. *Cell* **173**, 934-945 e912 (2018).

14. A. A. Alabi, R. W. Tsien, Perspectives on kiss-and-run: role in exocytosis, endocytosis, and neurotransmission. *Annu Rev Physiol* **75**, 393-422 (2013).

15. N. C. Harata, A. M. Aravanis, R. W. Tsien, Kiss-and-run and full-collapse fusion as modes of exo-endocytosis in neurosecretion. *J Neurochem* **97**, 1546-1570 (2006).

16. L. G. Wu, E. Hamid, W. Shin, H. C. Chiang, Exocytosis and endocytosis: modes, functions, and coupling mechanisms. *Annu Rev Physiol* **76**, 301-331 (2014).

17. P. J. Wen *et al.*, Actin dynamics provides membrane tension to merge fusing vesicles into the plasma membrane. *Nat Commun* **7**, 12604 (2016).

18. E. Karatekin, Toward a unified picture of the exocytotic fusion pore. *FEBS Lett* **592**, 3563-3585 (2018).

19. L. He, X.-S. Wu, R. Mohan, L.-G. Wu, Two modes of fusion pore opening revealed by cell-attached recordings at a synapse. *Nature* **444**, 102-105 (2006).

20. R. H. Chow, L. von Ruden, E. Neher, Delay in vesicle fusion revealed by electrochemical monitoring of single secretory events in adrenal chromaffin cells. *Nature* **356**, 60-63 (1992).

21. S. Obermuller *et al.*, Selective nucleotide-release from dense-core granules in insulin-secreting cells. *J Cell Sci* **118**, 4271-4282 (2005).

22. S. C. Collins *et al.*, Increased Expression of the Diabetes Gene SOX4 Reduces Insulin Secretion by Impaired Fusion Pore Expansion. *Diabetes* **65**, 1952-1961 (2016).

23. Z. Wu *et al.*, The neuronal calcium sensor Synaptotagmin-1 and SNARE proteins cooperate to dilate fusion pores. *Elife* **10**, e68215 (2021).

24. H. Bao *et al.*, Dynamics and number of trans-SNARE complexes determine nascent fusion pore properties. *Nature* **554**, 260-263 (2018).

25. A. H. Tang *et al.*, A trans-synaptic nanocolumn aligns neurotransmitter release to receptors. *Nature* **536**, 210-214 (2016).

26. D. R. Stevens, C. Schirra, U. Becherer, J. Rettig, Vesicle pools: lessons from adrenal chromaffin cells. *Front Synaptic Neurosci* **3**, 2 (2011).

27. T. Yuan, J. Lu, J. Zhang, Y. Zhang, L. Chen, Spatiotemporal detection and analysis of exocytosis reveal fusion "hotspots" organized by the cytoskeleton in endocrine cells. *Biophys J* **108**, 251-260 (2015).

28. J. Fu *et al.*, A glucose-dependent spatial patterning of exocytosis in human beta-cells is disrupted in type 2 diabetes. *JCI Insight* **5**, e127896 (2019).

29. K. P. Trogden *et al.*, Microtubules regulate pancreatic beta-cell heterogeneity via spatiotemporal control of insulin secretion hot spots. *Elife* **10**, e59912 (2021).

30. T. Branco, K. Staras, The probability of neurotransmitter release: variability and feedback control at single synapses. *Nat Rev Neurosci* **10**, 373-383 (2009).

31. A. Y. C. Wong, B. P. Graham, B. Billups, I. D. Forsythe, Distinguishing between presynaptic and postsynaptic mechanisms of short-term depression during action potential trains. *Journal of Neuroscience* **23**, 4868-4877 (2003).

32. C. E. Boudreau, D. Ferster, Short-term depression in thalamocortical synapses of cat primary visual cortex. *J Neurosci* **25**, 7179-7190 (2005).

33. J. Xu, L. G. Wu, The decrease in the presynaptic calcium current is a major cause of short-term depression at a calyx-type synapse. *Neuron* **46**, 633-645 (2005).

34. R. S. Zucker, W. G. Regehr, Short-term synaptic plasticity. *Annu Rev Physiol* **64**, 355-405 (2002).

35. J. M. Trifaro, M. F. Bader, J. P. Doucet, Chromaffin cell cytoskeleton: its possible role in secretion. *Can J Biochem Cell Biol* **63**, 661-679 (1985).

36. A. Papadopulos *et al.*, Activity-driven relaxation of the cortical actomyosin II network synchronizes Munc18-1-dependent neurosecretory vesicle docking. *Nat Commun* **6**, 6297 (2015).

37. J. D. Clements, R. A. Silver, Unveiling synaptic plasticity: a new graphical and analytical approach. *Trends Neurosci* **23**, 105-113 (2000).

38. C. F. Stevens, Y. Wang, Facilitation and depression at single central synapses. *Neuron* **14**, 795-802 (1995).

39. E. Neher, What is Rate-Limiting during Sustained Synaptic Activity: Vesicle Supply or the Availability of Release Sites. *Front Synaptic Neurosci* **2**, 144 (2010).

40. Y. Saheki, P. De Camilli, Synaptic vesicle endocytosis. *Cold Spring Harb Perspect Biol* **4**, a005645 (2012).

41. C. W. Chang, C. W. Chiang, M. B. Jackson, Fusion pores and their control of neurotransmitter and hormone release. *J Gen Physiol* **149**, 301-322 (2017).

42. S. Sharma, M. Lindau, The fusion pore, 60 years after the first cartoon. *FEBS Lett* **592**, 3542-3562 (2018).

43. E. Ales *et al.*, High calcium concentrations shift the mode of exocytosis to the kiss-and-run mechanism. *Nat Cell Biol* **1**, 40-44 (1999).

44. J. E. Heuser, T. S. Reese, Structural changes after transmitter release at the frog neuromuscular junction. *J Cell Biol* **88**, 564-580 (1981).

45. M. A. Bittner, R. L. Aikman, R. W. Holz, A nibbling mechanism for clathrin-mediated retrieval of secretory granule membrane after exocytosis. *J Biol Chem* **288**, 9177-9188 (2013).

46. P. S. Abbineni, D. Axelrod, R. W. Holz, Visualization of expanding fusion pores in secretory cells. *J Gen Physiol* **150**, 1640-1646 (2018).

47. W. D. Zhao *et al.*, Hemi-fused structure mediates and controls fusion and fission in live cells. *Nature* **534**, 548-552 (2016).

48. N. G. Gubernator *et al.*, Fluorescent false neurotransmitters visualize dopamine release from individual presynaptic terminals. *Science* **324**, 1441-1444 (2009).

49. J. W. Taraska, D. Perrais, M. Ohara-Imaizumi, S. Nagamatsu, W. Almers, Secretory granules are recaptured largely intact after stimulated exocytosis in cultured endocrine cells. *Proc Natl Acad Sci U S A* **100**, 2070-2075 (2003).

50. D. Perrais, I. C. Kleppe, J. W. Taraska, W. Almers, Recapture after exocytosis causes differential retention of protein in granules of bovine chromaffin cells. *J Physiol* **560**, 413-428 (2004).

51. W. Helfrich, Elastic properties of lipid bilayers: theory and possible experiments. *Z Naturforsch C* **28**, 693-703 (1973).

52. N. Porat-Shliom, O. Milberg, A. Masedunskas, R. Weigert, Multiple roles for the actin cytoskeleton during regulated exocytosis. *Cell Mol Life Sci* **70**, 2099-2121 (2013).

53. J. Dai, M. P. Sheetz, Membrane tether formation from blebbing cells. *Biophys J* **77**, 3363-3370 (1999).

54. Z. Shi, Z. T. Graber, T. Baumgart, H. A. Stone, A. E. Cohen, Cell Membranes Resist Flow. *Cell* **175**, 1769-1779 e1713 (2018).

55. N. Borghi, F. Brochard-Wyart, Tether extrusion from red blood cells: integral proteins unbinding from cytoskeleton. *Biophys J* **93**, 1369-1379 (2007).

56. J. T. Jenkins, Static equilibrium configurations of a model red blood cell. *J Math Biol* **4**, 149-169 (1977).

57. G. J. Palm *et al.*, The structural basis for spectral variations in green fluorescent protein. *Nat Struct Biol* **4**, 361-365 (1997).

58. P. S. Abbineni, M. A. Bittner, D. Axelrod, R. W. Holz, Chromogranin A, the major lumenal protein in chromaffin granules, controls fusion pore expansion. *J Gen Physiol* **151**, 118-130 (2019).

59. M. P. Stewart *et al.*, Hydrostatic pressure and the actomyosin cortex drive mitotic cell rounding. *Nature* **469**, 226-230 (2011).

60. K. Neuland, N. Sharma, M. Frick, Synaptotagmin-7 links fusion-activated Ca(2)(+) entry and fusion pore dilation. *J Cell Sci* **127**, 5218-5227 (2014).

61. W. Rawicz, K. C. Olbrich, T. McIntosh, D. Needham, E. Evans, Effect of chain length and unsaturation on elasticity of lipid bilayers. *Biophys J* **79**, 328-339 (2000).

62. J. Y. Tinevez *et al.*, Role of cortical tension in bleb growth. *Proc Natl Acad Sci U S A* **106**, 18581-18586 (2009).

63. S. Boulant, C. Kural, J. C. Zeeh, F. Ubelmann, T. Kirchhausen, Actin dynamics counteract membrane tension during clathrin-mediated endocytosis. *Nat Cell Biol* **13**, 1124-1131 (2011).

64. A. Diz-Munoz *et al.*, Control of directed cell migration in vivo by membrane-to-cortex attachment. *PLoS Biol* **8**, e1000544 (2010).

65. K. Tsujita, T. Takenawa, T. Itoh, Feedback regulation between plasma membrane tension and membrane-bending proteins organizes cell polarity during leading edge formation. *Nat Cell Biol* **17**, 749-758 (2015).

66. A. N. Weiss, M. A. Bittner, R. W. Holz, D. Axelrod, Protein mobility within secretory granules. *Biophys J* **107**, 16-25 (2014).

67. M. S. Montesinos *et al.*, The crucial role of chromogranins in storage and exocytosis revealed using chromaffin cells from chromogranin A null mouse. *J Neurosci* **28**, 3350-3358 (2008).

68. T. C. Rao *et al.*, Distinct fusion properties of synaptotagmin-1 and synaptotagmin-7 bearing dense core granules. *Mol Biol Cell* **25**, 2416-2427 (2014).

69. T. C. Rao *et al.*, Synaptotagmin isoforms confer distinct activation kinetics and dynamics to chromaffin cell granules. *J Gen Physiol* **149**, 763-780 (2017).

70. J. E. Heuser, T. S. Reese, Evidence for recycling of synaptic vesicle membrane during transmitter release at the frog neuromuscular junction. *J. Cell Biol* **57**, 315-344 (1973).

71. N. L. Kononenko, V. Haucke, Molecular mechanisms of presynaptic membrane retrieval and synaptic vesicle reformation. *Neuron* **85**, 484-496 (2015).

72. J. R. Monck, G. Alvarez de Toledo, J. M. Fernandez, Tension in secretory granule membranes causes extensive membrane transfer through the exocytotic fusion pore. *Proc Natl Acad Sci U S A* **87**, 7804-7808 (1990).

73. R. M. Hochmuth, N. Mohandas, P. L. Blackshear, Jr., Measurement of the elastic modulus for red cell membrane using a fluid mechanical technique. *Biophys J* **13**, 747-762 (1973).

74. H. Plattner, A. R. Artalejo, E. Neher, Ultrastructural organization of bovine chromaffin cell cortex-analysis by cryofixation and morphometry of aspects pertinent to exocytosis. *J Cell Biol* **139**, 1709-1717 (1997).

75. S. Bicknese, N. Periasamy, S. B. Shohet, A. S. Verkman, Cytoplasmic viscosity near the cell plasma membrane: measurement by evanescent field frequency-domain microfluorimetry. *Biophys J* **65**, 1272-1282 (1993).

76. U. Seifert, K. Berndl, R. Lipowsky, Shape transformations of vesicles: Phase diagram for spontaneous- curvature and bilayer-coupling models. *Phys Rev A* **44**, 1182-1202 (1991).

77. P. Mazzarello, A unifying concept: the history of cell theory. *Nat Cell Biol* **1**, E13-15 (1999).

78. Y. Diekmann, J. B. Pereira-Leal, Evolution of intracellular compartmentalization. *Biochem J* **449**, 319-331 (2013).

79. T. Gabaldon, A. A. Pittis, Origin and evolution of metabolic sub-cellular compartmentalization in eukaryotes. *Biochimie* **119**, 262-268 (2015).

80. J. Lombard, P. Lopez-Garcia, D. Moreira, The early evolution of lipid membranes and the three domains of life. *Nat Rev Microbiol* **10**, 507-515 (2012).

81. P. L. Yeagle, Lipid regulation of cell membrane structure and function. *FASEB J* **3**, 1833-1842 (1989).

82. Y. Hu, L. Qu, T. Schikorski, Mean synaptic vesicle size varies among individual excitatory hippocampal synapses. *Synapse* **62**, 953-957 (2008).

83. C. S. Olofsson *et al.*, Fast insulin secretion reflects exocytosis of docked granules in mouse pancreatic B-cells. *Pflugers Arch* **444**, 43-51 (2002).

84. J. A. Heymann *et al.*, 3D imaging of mammalian cells with ion-abrasion scanning electron microscopy. *J Struct Biol* **166**, 1-7 (2009).

85. C. Nanavati, V. S. Markin, A. F. Oberhauser, J. M. Fernandez, The exocytotic fusion pore modeled as a lipidic pore. *Biophys J* **63**, 1118-1132 (1992).

86. M. Lindau, W. Almers, Structure and function of fusion pores in exocytosis and ectoplasmic membrane fusion. *Curr Opin Cell Biol* **7**, 509-517 (1995).

87. X. Han, C. T. Wang, J. Bai, E. R. Chapman, M. B. Jackson, Transmembrane segments of syntaxin line the fusion pore of Ca2+-triggered exocytosis. *Science* **304**, 289-292 (2004).

88. C. W. Chang *et al.*, A structural role for the synaptobrevin 2 transmembrane domain in dense-core vesicle fusion pores. *J Neurosci* **35**, 5772-5780 (2015).

89. D. J. Adams, C. P. Arthur, M. H. Stowell, Architecture of the Synaptophysin/Synaptobrevin Complex: Structural Evidence for an Entropic Clustering Function at the Synapse. *Sci Rep* **5**, 13659 (2015).

90. G. J. Augustine, M. P. Charlton, S. J. Smith, Calcium entry and transmitter release at voltage-clamped nerve terminals of squid. *The Journal of physiology* **367**, 163-181 (1985).

91. C. Amatore, S. Arbault, I. Bonifas, M. Guille, Quantitative investigations of amperometric spike feet suggest different controlling factors of the fusion pore in exocytosis at chromaffin cells. *Biophys Chem* **143**, 124-131 (2009).

92. N. Wang *et al.*, Influence of cholesterol on catecholamine release from the fusion pore of large dense core chromaffin granules. *J Neurosci* **30**, 3904-3911 (2010).

93. W. Shin *et al.*, Vesicle Shrinking and Enlargement Play Opposing Roles in the Release of Exocytotic Contents. *Cell Rep* **30**, 421-431 e427 (2020).

94. M. Bretou *et al.*, Cdc42 controls the dilation of the exocytotic fusion pore by regulating membrane tension. *Mol Biol Cell* **25**, 3195-3209 (2014).

95. Z. Wu *et al.*, Dilation of fusion pores by crowding of SNARE proteins. *Elife* **6**, e22964 (2017).

96. T. C. Sudhof, J. E. Rothman, Membrane fusion: grappling with SNARE and SM proteins. *Science* **323**, 474-477 (2009).

97. Z. A. McDargh, A. Polley, B. O'Shaughnessy, SNARE-mediated membrane fusion is a two-stage process driven by entropic forces. *FEBS letters* **592**, 3504-3515 (2018).

98. S. C. Harrison, Viral membrane fusion. *Virology* **479-480**, 498-507 (2015).

99. T. Tang, M. Bidon, J. A. Jaimes, G. R. Whittaker, S. Daniel, Coronavirus membrane fusion mechanism offers a potential target for antiviral development. *Antiviral Res* **178**, 104792 (2020).

100. B. Chen, Molecular Mechanism of HIV-1 Entry. *Trends Microbiol* **27**, 878-891 (2019).

101. Y. A. Chizmadzhev, P. I. Kuzmin, D. A. Kumenko, J. Zimmerberg, F. S. Cohen, Dynamics of fusion pores connecting membranes of different tensions. *Biophys J* **78**, 2241-2256 (2000).

102. M. B. Jackson, Minimum membrane bending energies of fusion pores. *J Membrane Biol* **231**, 101-115 (2009).

103. V. A. Frolov, V. A. Lizunov, A. Y. Dunina-Barkovskaya, A. V. Samsonov, J. Zimmerberg, Shape bistability of a membrane neck: a toggle switch to control vesicle content release. *Proc Natl Acad Sci U S A* **100**, 8698-8703 (2003).

104. J. Yoo, M. B. Jackson, Q. Cui, A comparison of coarse-grained and continuum models for membrane bending in lipid bilayer fusion pores. *Biophys J* **104**, 841-852 (2013).

105. R. J. Ryham, M. A. Ward, F. S. Cohen, Teardrop shapes minimize bending energy of fusion pores connecting planar bilayers. *Phys Rev E Stat Nonlin Soft Matter Phys* **88**, 062701 (2013).

106. L. L. Jia, S. Pei, R. A. Pelcovits, T. R. Powers, Axisymmetric membranes with edges under external force: buckling, minimal surfaces, and tethers. *Soft Matter* **17**, 7268-7286 (2021).

107. I. Derenyi, F. Julicher, J. Prost, Formation and interaction of membrane tubes. *Phys Rev Lett* **88**, 238101 (2002).

108. T. R. Powers, G. Huber, R. E. Goldstein, Fluid-membrane tethers: minimal surfaces and elastic boundary layers. *Phys Rev E Stat Nonlin Soft Matter Phys* **65**, 041901 (2002).

109. L. Durand, Stability and Oscillations of a Soap Film - an Analytic Treatment. *Am J Phys* **49**, 334-343 (1981).

110. O. Y. Zhong-can, W. Helfrich, Bending energy of vesicle membranes: General expressions for the first, second, and third variation of the shape energy and applications to spheres and cylinders. *Phys Rev A Gen Phys* **39**, 5280-5288 (1989).

111. Y. J. Chen, P. H. Steen, Dynamics of inviscid capillary breakup: Collapse and pinchoff of a film bridge. *Journal of Fluid Mechanics* **341**, 245-267 (1997).

112. R. E. Goldstein, A. I. Pesci, C. Raufaste, J. D. Shemilt, Geometry of catenoidal soap film collapse induced by boundary deformation. *Phys Rev E* **104**, 035105 (2021).

113. A. Dall'Acqua, K. Deckelnick, G. Wheeler, Unstable Willmore surfaces of revolution subject to natural boundary conditions. *Calculus of Variations and Partial Differential Equations* **48**, 293-313 (2012).

114. M. Deserno (2004) Notes on differential geometry. (http://www.cmu.edu/biolphys/deserno/pdf/diff_geom.pdf).

115. P. Castro-Villarreal, J. Guven, Inverted catenoid as a fluid membrane with two points pulled together. *Phys Rev E Stat Nonlin Soft Matter Phys* **76**, 011922 (2007).

116. Z. Zhang *et al.*, Release mode of large and small dense-core vesicles specified by different synaptotagmin isoforms in PC12 cells. *Mol Biol Cell* **22**, 2324-2336 (2011).

117. P. Sens, J. Plastino, Membrane tension and cytoskeleton organization in cell motility. *J Phys Condens Matter* **27**, 273103 (2015).

118. F. Behroozi, P. S. Behroozi, Determination of surface tension from the measurement of internal pressure of mini soap bubbles. *Am J Phys* **79**, 1089-1093 (2011).

119. R. Capovilla, J. Guven, J. A. Santiago, Deformations of the geometry of lipid vesicles. *Journal of Physics a-Mathematical and General* **36**, 6281-6295 (2003).

120. M. Ito, T. Sato, In situ observation of a soap-film catenoid-a simple educational physics experiment. *Eur J Phys* **31**, 357-365 (2010).

121. B. Pontes, P. Monzo, N. C. Gauthier, Membrane tension: A challenging but universal physical parameter in cell biology. *Semin Cell Dev Biol* **71**, 30-41 (2017).

122. M. Deserno, Fluid lipid membranes: from differential geometry to curvature stresses. *Chem Phys Lipids* **185**, 11-45 (2015).

123. P. Heo, J. Coleman, J. B. Fleury, J. E. Rothman, F. Pincet, Nascent fusion pore opening monitored at single-SNAREpin resolution. *Proc Natl Acad Sci U S A* **118** (2021).

124. D. Das, H. Bao, K. C. Courtney, L. Wu, E. R. Chapman, Resolving kinetic intermediates during the regulated assembly and disassembly of fusion pores. *Nat Commun* **11**, 231 (2020).

125. A. Nath, W. M. Atkins, S. G. Sligar, Applications of phospholipid bilayer nanodiscs in the study of membranes and membrane proteins. *Biochemistry* **46**, 2059-2069 (2007).

126. A. Anantharam *et al.*, A new role for the dynamin GTPase in the regulation of fusion pore expansion. *Mol Biol Cell* **22**, 1907-1918 (2011).

127. Y. Kozlovsky, M. M. Kozlov, Stalk model of membrane fusion: solution of energy crisis. *Biophys J* **82**, 882-895 (2002).

128. Z. Zhang, M. B. Jackson, Membrane bending energy and fusion pore kinetics in Ca(2+)-triggered exocytosis. *Biophys J* **98**, 2524-2534 (2010).

129. L. Shi *et al.*, SNARE proteins: one to fuse and three to keep the nascent fusion pore open. *Science* **335**, 1355-1359 (2012).

130. R. Capovilla, J. Guven, Stresses in lipid membranes. *Journal of Physics a-Mathematical and General* **35**, 6233-6247 (2002).

131. T. C. Sudhof, J. Rizo, Synaptic vesicle exocytosis. *Cold Spring Harb Perspect Biol* **3** (2011).

132. N. Holderith *et al.*, Release probability of hippocampal glutamatergic terminals scales with the size of the active zone. *Nat Neurosci* **15**, 988-997 (2012).

133. R. G. Zhai, H. J. Bellen, The architecture of the active zone in the presynaptic nerve terminal. *Physiology (Bethesda)* **19**, 262-270 (2004).

134. R. C. Lin, R. H. Scheller, Mechanisms of synaptic vesicle exocytosis. *Annu Rev Cell Dev Biol* **16**, 19-49 (2000).

135. T. F. Martin, Tuning exocytosis for speed: fast and slow modes. *Biochim Biophys Acta* **1641**, 157-165 (2003).

136. F. A. Meunier, L. M. Gutierrez, Captivating New Roles of F-Actin Cortex in Exocytosis and Bulk Endocytosis in Neurosecretory Cells. *Trends Neurosci* **39**, 605-613 (2016).

137. M. Yoshihara, J. T. Littleton, Synaptotagmin I functions as a calcium sensor to synchronize neurotransmitter release. *Neuron* **36**, 897-908 (2002).

138. J. S. Dittman, T. A. Ryan, The control of release probability at nerve terminals. *Nat Rev Neurosci* **20**, 177-186 (2019).

139. M. C. Chicka, E. Hui, H. Liu, E. R. Chapman, Synaptotagmin arrests the SNARE complex before triggering fast, efficient membrane fusion in response to Ca2+. *Nat Struct Mol Biol* **15**, 827-835 (2008).

140. Z. A. McDargh, A. Polley, J. Zeng, B. O'Shaughnessy, Coupling of Ca<sup>2+</sup>-triggered unclamping and membrane fusion during neurotransmitter release. *bioRxiv* 10.1101/2021.06.16.448753, 2021.2006.2016.448753 (2021).

141. D. Maschi, V. A. Klyachko, Spatiotemporal Regulation of Synaptic Vesicle Fusion Sites in Central Synapses. *Neuron* **94**, 65-73 e63 (2017).

142. Y. Hua *et al.*, Blocking endocytosis enhances short-term synaptic depression under conditions of normal availability of vesicles. *Neuron* **80**, 343-349 (2013).

143. A. Yoshida *et al.*, Morphological changes of plasma membrane and protein assembly during clathrin-mediated endocytosis. *PLoS Biol* **16**, e2004786 (2018).

144. S. Watanabe *et al.*, Ultrafast endocytosis at mouse hippocampal synapses. *Nature* **504**, 242-247 (2013).

145. W. Shin *et al.*, Preformed Omega-profile closure and kiss-and-run mediate endocytosis and diverse endocytic modes in neuroendocrine chromaffin cells. *Neuron* **109**, 3119-3134 e3115 (2021).

146. M. Deserno, Fluid lipid membranes–a primer. *See* *http://www. cmu. edu/biolphys/deserno/pdf/membrane_theory. pdf* (2007).

147. P. Chengappa, K. Sao, T. M. Jones, R. J. Petrie, "Chapter Seven - Intracellular Pressure: A Driver of Cell Morphology and Movement" in International Review of Cell and Molecular Biology, L. Galluzzi, Ed. (Academic Press, 2018), vol. 337, pp. 185-211.

148. N. Zhu *et al.*, A Novel Coronavirus from Patients with Pneumonia in China, 2019. *N Engl J Med* **382**, 727-733 (2020).

149. Y. F. Tu *et al.*, A Review of SARS-CoV-2 and the Ongoing Clinical Trials. *Int J Mol Sci* **21**, 2657 (2020).

150. D. Wrapp *et al.*, Cryo-EM structure of the 2019-nCoV spike in the prefusion conformation. *Science* **367**, 1260-1263 (2020).

151. C. G. K. Ziegler *et al.*, SARS-CoV-2 Receptor ACE2 Is an Interferon-Stimulated Gene in Human Airway Epithelial Cells and Is Detected in Specific Cell Subsets across Tissues. *Cell* **181**, 1016-1035 e1019 (2020).

152. M. Hoffmann *et al.*, SARS-CoV-2 Cell Entry Depends on ACE2 and TMPRSS2 and Is Blocked by a Clinically Proven Protease Inhibitor. *Cell* **181**, 271-280 e278 (2020).

153. X. Ou *et al.*, Characterization of spike glycoprotein of SARS-CoV-2 on virus entry and its immune cross-reactivity with SARS-CoV. *Nat Commun* **11**, 1620 (2020).

154. S. C. Harrison, Viral membrane fusion. *Nat Struct Mol Biol* **15**, 690-698 (2008).

155. T. Heald-Sargent, T. Gallagher, Ready, set, fuse! The coronavirus spike protein and acquisition of fusion competence. *Viruses* **4**, 557-580 (2012).

156. Y. Cai *et al.*, Distinct conformational states of SARS-CoV-2 spike protein. *Science* **369**, 1586-1592 (2020).

157. Z. A. Jaafar, J. S. Kieft, Viral RNA structure-based strategies to manipulate translation. *Nat Rev Microbiol* **17**, 110-123 (2019).

158. A. C. Walls *et al.*, Structure, Function, and Antigenicity of the SARS-CoV-2 Spike Glycoprotein. *Cell* **181**, 281-292 e286 (2020).

159. S. Xia *et al.*, Inhibition of SARS-CoV-2 (previously 2019-nCoV) infection by a highly potent pan-coronavirus fusion inhibitor targeting its spike protein that harbors a high capacity to mediate membrane fusion. *Cell Res* **30**, 343-355 (2020).

160. T. Ivanovic, J. L. Choi, S. P. Whelan, A. M. van Oijen, S. C. Harrison, Influenza-virus membrane fusion by cooperative fold-back of stochastically induced hemagglutinin intermediates. *Elife* **2**, e00333 (2013).

161. M. S. Ladinsky *et al.*, Electron tomography visualization of HIV-1 fusion with target cells using fusion inhibitors to trap the pre-hairpin intermediate. *Elife* **9**, e58411 (2020).

162. D. J. Benton, S. J. Gamblin, P. B. Rosenthal, J. J. Skehel, Structural transitions in influenza haemagglutinin at membrane fusion pH. *Nature* **583**, 150-153 (2020).

163. T. C. Marcink, T. Wang, A. des Georges, M. Porotto, A. Moscona, Human parainfluenza virus fusion complex glycoproteins imaged in action on authentic viral surfaces. *PLoS Pathog* **16**, e1008883 (2020).

164. P. Chen *et al.*, SARS-CoV-2 Neutralizing Antibody LY-CoV555 in Outpatients with Covid-19. *N Engl J Med* **384**, 229-237 (2021).

165. A. Baum *et al.*, REGN-COV2 antibodies prevent and treat SARS-CoV-2 infection in rhesus macaques and hamsters. *Science* **370**, 1110-1115 (2020).

166. L. A. Jackson *et al.*, An mRNA Vaccine against SARS-CoV-2 - Preliminary Report. *N Engl J Med* **383**, 1920-1931 (2020).

167. E. E. Walsh *et al.*, Safety and Immunogenicity of Two RNA-Based Covid-19 Vaccine Candidates. *N Engl J Med* **383**, 2439-2450 (2020).

168. R. D. de Vries *et al.*, Intranasal fusion inhibitory lipopeptide prevents direct-contact SARS-CoV-2 transmission in ferrets. *Science* **371**, 1379-1382 (2021).

169. B. J. Bosch *et al.*, Severe acute respiratory syndrome coronavirus (SARS-CoV) infection inhibition using spike protein heptad repeat-derived peptides. *Proc Natl Acad Sci U S A* **101**, 8455-8460 (2004).

170. T. C. Marcink *et al.*, Hijacking the Fusion Complex of Human Parainfluenza Virus as an Antiviral Strategy. *mBio* **11**, e03203-03219 (2020).

171. J. LaBonte, J. Lebbos, P. Kirkpatrick, Enfuvirtide. *Nat Rev Drug Discov* **2**, 345-346 (2003).

172. M. Hoffmann *et al.*, SARS-CoV-2 variants B.1.351 and P.1 escape from neutralizing antibodies. *Cell* **184**, 2384-2393 e2312 (2021).

173. L. Casalino *et al.*, Beyond Shielding: The Roles of Glycans in the SARS-CoV-2 Spike Protein. *ACS Cent Sci* **6**, 1722-1734 (2020).

174. B. Turonova *et al.*, In situ structural analysis of SARS-CoV-2 spike reveals flexibility mediated by three hinges. *Science* **370**, 203-208 (2020).

175. A. Ali, R. Vijayan, Dynamics of the ACE2-SARS-CoV-2/SARS-CoV spike protein interface reveal unique mechanisms. *Sci Rep* **10**, 14214 (2020).

176. G. Khelashvili, A. Plante, M. Doktorova, H. Weinstein, Ca(2+)-dependent mechanism of membrane insertion and destabilization by the SARS-CoV-2 fusion peptide. *Biophys J* **120**, 1105-1119 (2021).

177. D. Gorgun, M. Lihan, K. Kapoor, E. Tajkhorshid, Binding mode of SARS-CoV-2 fusion peptide to human cellular membrane. *Biophys J* **120**, 2914-2926 (2021).

178. S. Borkotoky, D. Dey, M. Banerjee, Computational Insight Into the Mechanism of SARS-CoV-2 Membrane Fusion. *J Chem Inf Model* **61**, 423-431 (2021).

179. A. Yu *et al.*, A multiscale coarse-grained model of the SARS-CoV-2 virion. *Biophys J* **120**, 1097-1104 (2021).

180. S. Barfoot, D. Poger, A. E. Mark, Understanding the Activated Form of a Class-I Fusion Protein: Modeling the Interaction of the Ebola Virus Glycoprotein 2 with a Lipid Bilayer. *Biochemistry* **59**, 4051-4058 (2020).

181. X. Lin, J. K. Noel, Q. Wang, J. Ma, J. N. Onuchic, Atomistic simulations indicate the functional loop-to-coiled-coil transition in influenza hemagglutinin is not downhill. *Proc Natl Acad Sci U S A* **115**, E7905-E7913 (2018).

182. M. Lin, L. T. Da, Refolding Dynamics of gp41 from Pre-fusion to Pre-hairpin States during HIV-1 Entry. *J Chem Inf Model* **60**, 162-174 (2020).

183. C. M. Carr, P. S. Kim, A spring-loaded mechanism for the conformational change of influenza hemagglutinin. *Cell* **73**, 823-832 (1993).

184. D. J. Benton *et al.*, Receptor binding and priming of the spike protein of SARS-CoV-2 for membrane fusion. *Nature* **588**, 327-330 (2020).

185. S. Hakansson-McReynolds, S. Jiang, L. Rong, M. Caffrey, Solution structure of the severe acute respiratory syndrome-coronavirus heptad repeat 2 domain in the prefusion state. *J Biol Chem* **281**, 11965-11971 (2006).

186. D. Xu, Y. Zhang, Ab initio protein structure assembly using continuous structure fragments and optimized knowledge-based force field. *Proteins* **80**, 1715-1735 (2012).

187. Z. Ke *et al.*, Structures and distributions of SARS-CoV-2 spike proteins on intact virions. *Nature* **588**, 498-502 (2020).

188. A. L. Lai, J. H. Freed, SARS-CoV-2 Fusion Peptide has a Greater Membrane Perturbating Effect than SARS-CoV with Highly Specific Dependence on Ca(2). *J Mol Biol* **433**, 166946 (2021).

189. B. O'Shaughnessy, U. Sawhney, Polymer reaction kinetics at interfaces. *Phys Rev Lett* **76**, 3444-3447 (1996).

190. T. C. Marcink *et al.*, Intermediates in SARS-CoV-2 spike-mediated cell entry. *Sci Adv* **8**, eabo3153 (2022).

191. V. K. Outlaw *et al.*, Inhibition of Coronavirus Entry In Vitro and Ex Vivo by a Lipid-Conjugated Peptide Derived from the SARS-CoV-2 Spike Glycoprotein HRC Domain. *mBio* **11**, e01935-01920 (2020).

192. J. L. Baylon, E. Tajkhorshid, Capturing Spontaneous Membrane Insertion of the Influenza Virus Hemagglutinin Fusion Peptide. *J Phys Chem B* **119**, 7882-7893 (2015).

193. L. J. Calder, P. B. Rosenthal, Cryomicroscopy provides structural snapshots of influenza virus membrane fusion. *Nat Struct Mol Biol* **23**, 853-858 (2016).

194. D. J. Benton *et al.*, Influenza hemagglutinin membrane anchor. *Proc Natl Acad Sci U S A* **115**, 10112-10117 (2018).

195. L. Lu *et al.*, Structure-based discovery of Middle East respiratory syndrome coronavirus fusion inhibitor. *Nat Commun* **5**, 3067 (2014).

196. C. Wang *et al.*, A conserved immunogenic and vulnerable site on the coronavirus spike protein delineated by cross-reactive monoclonal antibodies. *Nat Commun* **12**, 1715 (2021).

197. B. Webb, A. Sali, Comparative Protein Structure Modeling Using MODELLER. *Curr Protoc Bioinformatics* **54**, 5 6 1-5 6 37 (2016).

198. S. Jo, T. Kim, V. G. Iyer, W. Im, CHARMM-GUI: a web-based graphical user interface for CHARMM. *J Comput Chem* **29**, 1859-1865 (2008).

199. W. L. Jorgensen, J. Chandrasekhar, J. D. Madura, R. W. Impey, M. L. Klein, Comparison of Simple Potential Functions for Simulating Liquid Water. *Journal of Chemical Physics* **79**, 926-935 (1983).

200. W. G. Hoover, Canonical dynamics: Equilibrium phase-space distributions. *Phys Rev A Gen Phys* **31**, 1695-1697 (1985).

201. S. J. T. J. o. c. p. Nosé, A unified formulation of the constant temperature molecular dynamics methods. **81**, 511-519 (1984).

202. M. Parrinello, A. Rahman, Polymorphic Transitions in Single-Crystals - a New Molecular-Dynamics Method. *Journal of Applied Physics* **52**, 7182-7190 (1981).

203. H. Bekker *et al.* (1993) Gromacs: A parallel computer for molecular dynamics simulations. in *Physics computing* (World Scientific Singapore), pp 252-256.

204. H. J. C. Berendsen, D. Vanderspoel, R. Vandrunen, Gromacs - a Message-Passing Parallel Molecular-Dynamics Implementation. *Computer Physics Communications* **91**, 43-56 (1995).

205. W. Kabsch, C. Sander, Dictionary of protein secondary structure: pattern recognition of hydrogen-bonded and geometrical features. *Biopolymers* **22**, 2577-2637 (1983).

206. R. P. Joosten *et al.*, A series of PDB related databases for everyday needs. *Nucleic Acids Res* **39**, D411-419 (2011).

207. R. B. Best *et al.*, Optimization of the additive CHARMM all-atom protein force field targeting improved sampling of the backbone ϕ, ψ and side-chain $\chi1$ and $\chi2$ dihedral angles. **8**, 3257-3273 (2012).

208. J. B. Klauda *et al.*, Update of the CHARMM all-atom additive force field for lipids: validation on six lipid types. *J Phys Chem B* **114**, 7830-7843 (2010).

209. D. H. de Jong *et al.*, Improved Parameters for the Martini Coarse-Grained Protein Force Field. *J Chem Theory Comput* **9**, 687-697 (2013).

210. S. J. Marrink, H. J. Risselada, S. Yefimov, D. P. Tieleman, A. H. de Vries, The MARTINI force field: coarse grained model for biomolecular simulations. *J Phys Chem B* **111**, 7812-7824 (2007).

211. T. A. Wassenaar, H. I. Ingolfsson, R. A. Bockmann, D. P. Tieleman, S. J. Marrink, Computational Lipidomics with insane: A Versatile Tool for Generating Custom Membranes for Molecular Simulations. *J Chem Theory Comput* **11**, 2144-2155 (2015).

212. G. Bussi, D. Donadio, M. J. T. J. o. c. p. Parrinello, Canonical sampling through velocity rescaling. **126**, 014101 (2007).

213. H. J. C. Berendsen, J. P. M. Postma, W. F. Vangunsteren, A. Dinola, J. R. Haak, Molecular-Dynamics with Coupling to an External Bath. *Journal of Chemical Physics* **81**, 3684-3690 (1984).

214. R. T. McGibbon *et al.*, MDTraj: A Modern Open Library for the Analysis of Molecular Dynamics Trajectories. *Biophys J* **109**, 1528-1532 (2015).

215. T. A. Wassenaar, K. Pluhackova, R. A. Bockmann, S. J. Marrink, D. P. Tieleman, Going Backward: A Flexible Geometric Approach to Reverse Transformation from Coarse Grained to Atomistic Models. *J Chem Theory Comput* **10**, 676-690 (2014).